

The morphology of the X-ray afterglows and of the jetted GeV emission in long GRBs

R. Ruffini,^{1,2,5,7,14} R. Moradi,^{1,2,15*} J. A. Rueda,^{1,2,4,8,16} L. Li,^{1,2,15} N. Sahakyan,^{1,6} Y.-C. Chen,^{1,2} Y. Wang,^{1,2,15} Y. Aimuratov,^{1,2,9} L. Becerra,^{1,2,17} C. L. Bianco,^{1,2,16} C. Cherubini,^{1,3,11} S. Filippi,^{1,3,10} M. Karlica,^{1,2} G. J. Mathews,^{1,12} M. Muccino,¹³ G. B. Pisani,^{1,2} and S. S. Xue^{1,2}

¹ ICRA^{Net}, Piazza della Repubblica 10, I-65122 Pescara, Italy

² ICRA, Dipartimento di Fisica, Università di Roma “La Sapienza”, Piazzale Aldo Moro 5, I-00185 Roma, Italy

³ ICRA, University Campus Bio-Medico of Rome, Via Alvaro del Portillo 21, I-00128 Rome, Italy

⁴ ICRA^{Net}-Ferrara, Dipartimento di Fisica e Scienze della Terra, Università degli Studi di Ferrara, Via Saragat 1, I-44122 Ferrara, Italy

⁵ ICRA^{Net}-Rio, Centro Brasileiro de Pesquisas Físicas, Rua Dr. Xavier Sigaud 150, 22290-180 Rio de Janeiro, Brazil

⁶ ICRA^{Net}-Armenia, Marshall Baghramian Avenue 24a, Yerevan 0019, Republic of Armenia

⁷ Université de Nice Sophia-Antipolis, Grand Château Parc Valrose, Nice, CEDEX 2, France

⁸ Dipartimento di Fisica e Scienze della Terra, Università degli Studi di Ferrara, Via Saragat 1, I-44122 Ferrara, Italy

⁹ Fesenkov Astrophysical Institute, Observatory 23, 050020 Almaty, Kazakhstan

¹⁰ Department of Engineering, University Campus Bio-Medico of Rome, Nonlinear Physics and Mathematical Modeling Lab, Via Alvaro del Portillo 21, 00128 Rome, Italy

¹¹ Department of Science and Technology for Humans and the Environment and Nonlinear Physics and Mathematical Modeling Lab, University Campus Bio-Medico of Rome, Via Alvaro del Portillo 21, 00128 Rome, Italy

¹² Center for Astrophysics, Department of Physics, University of Notre Dame, Notre Dame, IN, 46556, USA

¹³ Istituto Nazionale di Fisica Nucleare, Laboratori Nazionali di Frascati, I-00044 Frascati, Italy

¹⁴ INAF, Viale del Parco Mellini 84, 00136 Rome, Italy

¹⁵ INAF – Osservatorio Astronomico d’Abruzzo, Via M. Maggini snc, I-64100, Teramo, Italy

¹⁶ INAF, Istituto di Astrofisica e Planetologia Spaziali, Via Fosso del Cavaliere 100, 00133 Rome, Italy

¹⁷ Instituto de Astrofísica, Facultad de Física, Pontificia Universidad Católica de Chile, Av. Vicuña Mackenna 4860, Macul, Santiago, Chile

Accepted XXX. Received YYY; in original form ZZZ

ABSTRACT

We recall evidence that long gamma-ray bursts (GRBs) have binary progenitors and give new examples. Binary-driven hypernovae (BdHNe) consist of a carbon-oxygen core (CO_{core}) and a neutron star (NS) companion. For binary periods ~ 5 min, the CO_{core} collapse originates the subclass BdHN I characterized by: 1) an energetic supernova (the “SN-rise”); 2) a black hole (BH), born from the NS collapse by SN matter accretion, leading to a GeV emission with luminosity $L_{\text{GeV}} = A_{\text{GeV}} t^{-\alpha_{\text{GeV}}}$, observed only in some cases; 3) a new NS (ν NS), born from the SN, originating the X-ray afterglow with $L_X = A_X t^{-\alpha_X}$, observed in all BdHN I. We record 378 sources and present for four prototypes GRBs 130427A, 160509A, 180720B and 190114C: 1) spectra, luminosities, SN-rise duration; 2) A_X , $\alpha_X = 1.48 \pm 0.32$, and 3) the ν NS spin time-evolution. We infer a) A_{GeV} , $\alpha_{\text{GeV}} = 1.19 \pm 0.04$; b) the BdHN I morphology from time-resolved spectral analysis, three-dimensional simulations, and the GeV emission presence/absence in 54 sources within the Fermi-LAT boresight angle. For 25 sources, we give the integrated and time-varying GeV emission, 29 sources have no GeV emission detected and show X/gamma-ray flares previously inferred as observed along the binary plane. The 25/54 ratio implies the GeV radiation is emitted within a cone of half-opening angle $\approx 60^\circ$ from the normal to the orbital plane. We deduce BH masses 2.3–8.9 M_\odot and spin 0.27–0.87 by explaining the GeV emission from the BH energy extraction, while their time evolution validates the BH mass-energy formula.

Key words: gamma-ray bursts: general — binaries: general — stars: neutron — supernovae: general — black hole physics

1 INTRODUCTION

The year 2021 marks the 50th anniversary of the paper “Introducing the black hole” (Ruffini & Wheeler 1971) and of the black hole (BH) mass-energy formula (Christodoulou 1970; Christodoulou &

Ruffini 1971; Hawking 1971; Hawking 1972). Since those days, interest in BHs has spread worldwide and their study represents one of the most innovative fields of fundamental physics and astrophysics. There has also been an exponential growth of observational and theoretical developments which are finally reaching the momentous result of unveiling the process of rotational energy extraction from a rotating Kerr BH. We indicate the path of this discovery in the present paper. This realization has allowed for the identification of

* ruffini@icra.it, rahim.moradi@inaf.it, liang.li@icranet.org, jorge.rueda@icra.it, yu.wang@icranet.org

the code of GRBs: one of the most complex sequences of a very large number of non-repetitive classical and quantum events, each of which are characterized by specific spectral and temporal properties. In parallel, a new arena for fundamental physics has been revealed by the dubbed “*blackholic quantum*” (Rueda & Ruffini 2020). This enormous conceptual progress has not been reached straightforwardly: it has come from an intense dedicated process with continuous feedback between theoretical understanding, unprecedented panchromatic observational progress, and modification of basic interpretation paradigms: they have all been truly essential. We first summarize in this introduction some of the contributions which have led to the start of this most complex inquiry into the the most powerful energy source in the Universe.

1.1 The initial “golden age” of Relativistic Astrophysics

The first breakthrough in relativistic astrophysics was the discovery of pulsars in 1967 (Hewish et al. 1968), and the discovery of a pulsar in the core of the Crab Nebula (Staelin & Reifstein 1968; Reifstein et al. 1969). The identification of the energy source of the pulsar with a fast rotating newly born neutron star (NS); the new NS (vNS), coincident with the supernova (SN) explosion led to a new paradigm in SN understanding (Shklovskij 1969). As we show in this paper, we are gaining a deeper understanding of both of SNe and of the role of the vNS in the binary driven hypernova (BdHN) systems.

The second breakthrough came from the launch in 1970 of the first X-Ray telescope, observing in the 2–20 keV energy band: the Uhuru satellite (see e.g. Giacconi & Ruffini 1978; Giacconi 2003). Uhuru paved the way for a crucial working method in developing a multiwavelength collaboration with optical and radio observatories. Thanks to the theoretical understanding, this led to the discovery, inside our own galaxy, of a large number of binary X-ray sources composed of a main sequence star and a companion NS (like Hercules X-1 and Centaurus X-3) and a binary system composed of a main sequence star and a BH, which gave the first evidence for the discovery of a BH in our Galaxy (see Ruffini 1974; Giacconi & Ruffini 1978, for details). It was soon realized that these binary X-ray sources would themselves further evolve as the companion main sequence star would undergo a SN explosion on timescales of 10^8 y (Ruffini 1974). In view of the limited number of such binary X-ray sources in our Galaxy, the expected observational rate of the final evolution of such binary systems would be on the order of 10^{-8} events/y in our Galaxy. The point that was missed at the time was the existence of the process of “*induced gravitational collapse*”, which was identified years later (Ruffini et al. 2001; Rueda & Ruffini 2012). This implies an unprecedented energy emission of $\sim 10^{54}$ erg, making them observable from all galaxies in the entire Universe: if the number of galaxies in our past light-cone is taken into account, the expected observational rate of the final evolution of such binary X-ray sources in the entire Universe is on the order of 10–100 events/y.

The third breakthrough was the introduction in 1971 of the BH mass-energy formula by Christodoulou, Hawking, Ruffini (Christodoulou 1970; Christodoulou & Ruffini 1971; Hawking 1971; Hawking 1972), and the BH extractable energy by reversible

and irreversible transformation (in geometric $c = G = 1$ units):

$$M^2 = \frac{J^2}{4M_{\text{irr}}^2} + M_{\text{irr}}^2, \quad (1a)$$

$$S = 16\pi M_{\text{irr}}^2 \quad (1b)$$

$$\delta S = 32\pi M_{\text{irr}} \delta M_{\text{irr}} \geq 0, \quad (1c)$$

where J , M , M_{irr} and S are the angular momentum, mass, irreducible mass and horizon surface area of the BH.

Again in this article, we indicate the path to observe for the first time the BH extractable energy process, which can be as high as 29% of the BH mass for an extreme Kerr BH. We measure as well the BH mass and spin in selected BdHN.

Just at the end of this “initial golden age of relativistic astrophysics”, the discovery of GRBs was publicly announced in February 1974 at the annual meeting of the American Association for the Advancement of Science, in San Francisco (see details in Gursky & Ruffini 1975). In that meeting, observations by the Vela 5 and Vela 6 satellites were presented. These satellites operated in the 3–12 keV X-ray energy band and, for the first time, in the 150–750 keV (Vela 5) and 300–1500 keV (Vela 6) gamma-ray energy bands. Tens of gamma-ray events per year of unknown origin, lasting for a few seconds, and originating outside the Solar System, were named “Gamma-Ray Bursts” (details in Klebesadel et al. 1973; Strong 1975).

What has become clear only recently, and further clarified in this article, is that precisely the late catastrophic evolution of the binary X-ray sources leads to the BdHN: the progenitors of a class of long gamma-ray bursts (GRBs). Indeed, these highest luminosity energy sources in the Universe are observed to occur at a rate of 10–100 events/y, consistent with the order of magnitude estimate given above.

We proceed to focus on the most recent developments, selecting crucial observational milestones, theoretical developments, and define the interpretation paradigms which have recently led to a unified understanding of the GRBs.

1.2 The largest ever multi-wavelength observational efforts

The earliest evidence for high-energy radiation above 100 MeV from GRBs were the observations by the Energetic Gamma-Ray Experiment Telescope (*EGRET*), operating in the energy range ~ 20 MeV–30 GeV, onboard of the Compton Gamma-Ray Observatory (*CGRO*, 1991–2000). The detection was triggered by the Burst And Transient Source Experiment (*BATSE*), operating in energy range of ~ 20 –2000 keV. *EGRET* has detected five GRBs which, from our understanding today, were long duration bursts: GRB 910503, GRB 910601, GRB 930131, GRB 940217, and GRB 940301 (see e.g. Kanbach 1996, and references therein). Unfortunately, no redshift was known at the time.

A new epoch started with the launch of the Beppo-Sax satellite in 1996, joining the expertise of the X-ray and gamma-ray communities. Its gamma-ray burst monitor (GRBM) operating in the 40–700 keV energy band determined the trigger of the GRB, and two wide-field cameras operating in the 2–30 keV X-ray energy band allowed the localization of the source to within arc-minutes resolution. This enabled a follow-up with the narrow-field instruments (NFI) in the 2–10 keV energy band.

Beppo-SAX achieved three major results:

(i) The discovery of the X-ray afterglow (GRB 970228, Costa et al. (1997)), characterized by an X-ray luminosity decreasing with

a power-law with index of $\alpha_X = -1.48 \pm 0.32$ (see de Pasquale et al. 2006, as well as Li et al. 2015; Pisani et al. 2016; Li et al. 2018b). In this article, we specifically address the astrophysical origin of the afterglow.

(ii) The determination of the accurate positions by the NFI, transmitted to the optical (van Paradijs et al. 1997) and radio telescopes (Frail et al. 1997), allowed the determination of the GRB cosmological redshifts. The first redshift was measured for GRB 970508 (Metzger et al. 1997), using the LRIS instrument of the Keck II telescope (Oke et al. 1995). The derived distances of $\approx 5\text{--}10$ Gpc confirmed their cosmological origin and their unprecedented energetics, $\approx 10^{50}\text{--}10^{54}$ erg, thus validating our hypothesis derived from first principles (Damour & Ruffini 1975; Ruffini 1998).

(iii) The discovery of the temporal and spatial coincidence of GRB 980425 with SN 1998bw (Galama et al. 1998), which suggested the connection between GRBs and SNe, was soon supported by many additional events (see e.g. Woosley & Bloom 2006; Della Valle 2011; Hjorth & Bloom 2012; Li et al. 2012, 2018a). The astrophysical origin of this coincidence is addressed in this article within the BdHN approach.

The Neil Gehrels *Swift* Observatory (hereafter indicated as *Swift*) followed in 2004. It was conceived as a panchromatic space observatory dedicated to the observations of GRBs. The GRB trigger is detected by the large field of view of its Burst Alert Telescope (BAT) (Barthelmy et al. 2005), operating in the hard X-ray band. This is followed up by the fast and automatic observations of the onboard narrow fields instruments XRT (Burrows et al. 2005) and UVOT (Roming et al. 2005) operating in the soft/medium X-ray and in the optical/UV bands, respectively. The BAT telescope operates in the 15–150 keV energy band and can detect the GRB prompt emission while accurately determining its position in the sky within 3 arcmin. Within 90 s, *Swift* can repoint the XRT telescope, operating in the 0.3–10 keV energy range, and relay promptly the burst position to the ground. Unfortunately, this does not allow the establishment of the initial *Swift*-XRT detection prior to the *Swift*-BAT trigger, as later explained in this article.

Thanks to the *Swift* satellite, the number of detected GRBs increased rapidly to 1300 sources with known redshifts (see, e.g., Giommi et al. 2020). By analyzing the light-curve of some long GRBs, Nousek et al. (2006) and Zhang et al. (2006) discovered three power-law segments in the XRT flux light curves prior to the afterglow emission (see, also, Li et al. 2015; Li et al. 2018a). We refer in this article to these segments as the “Nousek-Zhang power-laws”. All the X-ray afterglow observations considered in this article refer to *Swift*-XRT observation.

The high-energy astrophysics era of GRB observations started with the launch of *AGILE* in 2007 (Tavani et al. 2009) with the onboard Gamma-Ray Imaging Detector (*GRID*) operating in the 30 MeV–50 GeV energy range. *AGILE* was soon followed by the launch in June 2008 of the *Fermi* satellite, having onboard the Gamma-ray Burst Monitor (GBM) operating in the 8 keV–40 MeV energy range (Meegan et al. 2009) and the Large Area Telescope (LAT) operating in the 20 MeV–300 GeV energy range (Atwood et al. 2009).

AGILE-GRID detected the first long GRB with emission above 100 MeV and with a photometric redshift of $z = 1.8$, GRB 080514B (Giuliani et al. 2008). It was followed four months later by the detection of GRB 080916C (Greiner et al. 2009) by *Fermi* with one of the largest isotropic energies ever detected, $E_{\text{iso}} = (4.07 \pm 0.86) \times 10^{54}$ erg, and a photometric redshift of $z = 4.35$. These were followed by a large number of long GRBs observed by LAT with

both GeV emission and with a well-defined z . All the high-energy long GRBs considered in this article are based on the first and second Fermi-LAT GRB catalogs (Ackermann et al. 2013; Ajello et al. 2019).

The leading observations from space observatories were followed by a multitude of equally essential observations from ground-based observatories spanning the globe. The leading role was taken by the largest optical telescopes, e.g. the VLT from ESO with its X-shooter instrument (Vernet et al. 2011), and radio telescopes. This vastest ever multiwavelength observational campaign has been recently further extended to the very-high-energy (VHE) domain with the GRB detection by observatories on the ground. This is the case of the observations of GRB 190114C by the Imaging Atmospheric Cherenkov Telescopes MAGIC (see Fig. 3 and MAGIC Collaboration et al. 2019a), designed to detect VHE gamma-rays from 30 GeV to more than 50 TeV (see e.g. Aleksić et al. 2016a,b), the observations of GRB 180720B by H.E.S.S. (see Fig. 2 and Abdalla et al. 2019), operating in the energy range from tens of GeV to tens of TeV (see e.g. Aharonian et al. 2006), as well as GRB 190829A (Chand et al. 2020), which we also address in this article.

1.3 The short GRBs with binary NS progenitors

One of the main results of the observations of the CGRO satellite (Murdin 2000) was the isotropic distribution of the GRBs when expressed in galactic coordinates (Meegan et al. 1992). This result gave the first preliminary indication of the cosmological nature of GRBs. This was later confirmed by irrefutable evidence from the observations of Beppo-Sax, as mentioned above. An additional result was the clear indication of the existence of two different classes of GRBs: the short and the long GRBs (Kouveliotou et al. 1993). This classification has been confirmed and further extended as we recall in Section 2, now duly expressing all quantities, after Beppo-Sax, in the rest frame of the source.

The first proposal of successfully relating a GRB to an astrophysical cosmological source came from the vision of Bohdan Paczynski and collaborators, who identified the progenitors of short GRBs with merging NS binaries (see, e.g., Paczynski 1986; Eichler et al. 1989; Narayan et al. 1991, 1992; Mao & Paczynski 1992; Narayan et al. 1992). This result was later confirmed by Beppo-Sax (Li & Paczyński 1998, 2000, 2006; Berger 2014). Complementary information came from the localization of short GRBs at large off-sets from their host galaxies and with no star formation evidence (see, e.g., Fox et al. 2005; Gehrels et al. 2005; Berger 2014). The following fundamental discovery came from the identification of the first short GRB in the GeV band by *AGILE*. The first observation of a short GRB was done by *AGILE* who detected GRB 090510A at a spectroscopic redshift of $z = 0.903$, with $E_{\text{iso}} = (3.95 \pm 0.21) \times 10^{52}$ erg, and a significant GeV emission $E_{\text{LAT}} = (5.78 \pm 0.60) \times 10^{52}$ erg. On the basis of the observed energetics of this source, and its spectral properties, we proposed that in this short GRB we witness the birth of a BH, which we associate with the onset of the GeV emission: the signature of this event (Ruffini et al. 2016a).

This identification further evolved with the introduction of the two sub-classes of short bursts (Ruffini et al. 2015b, 2016a,b; Aimurátov et al. 2017). The first sub-class corresponds to short bursts with isotropic energies $E_{\text{iso}} < 10^{52}$ erg (in the rest-frame 1–10⁴ keV energy band) and rest-frame spectral peak energies $E_{\text{p},i} < 2$ MeV. These are expected to originate when the NS-NS merger leads to a single massive NS (M-NS) with a mass below the NS critical mass. We have called these sources short gamma-ray flashes (S-GRFs).

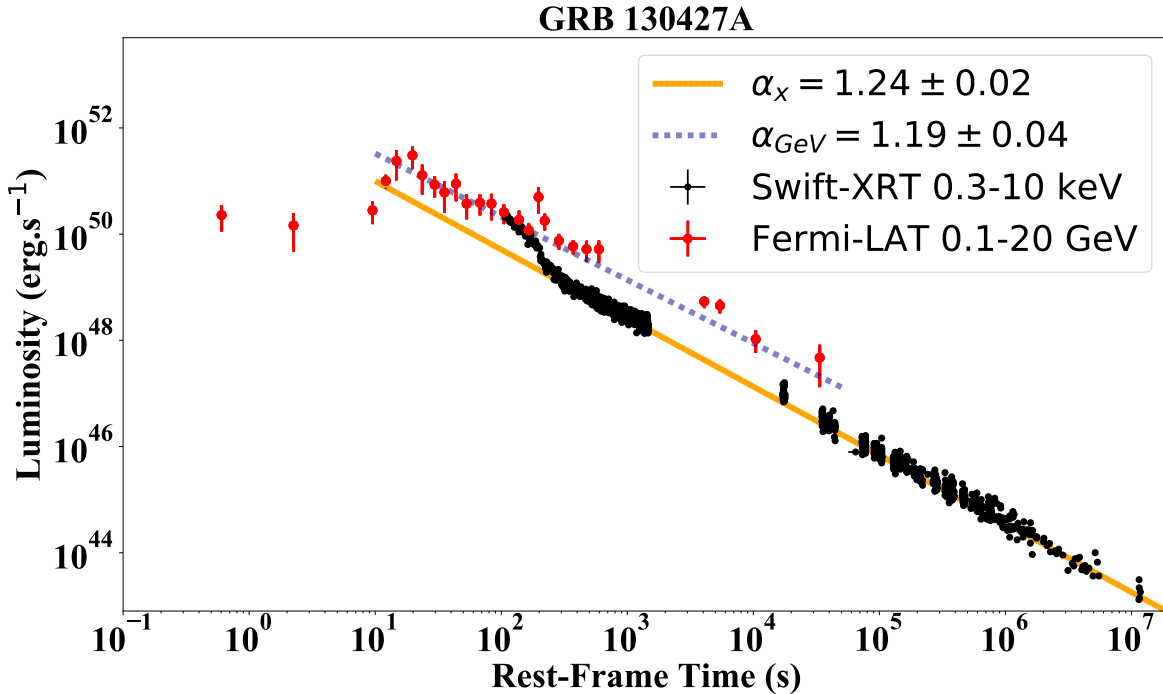


Figure 1. Luminosity of BdHN I 130427A: the black data points represent the rest-frame 0.3–10 keV luminosity obtained from *Swift*-XRT. It follows a decaying power-law with amplitude $(3.65 \pm 0.63) \times 10^{52} \text{ erg s}^{-1}$ and index $\alpha_X = 1.24 \pm 0.02$. The red data points show the rest-frame in 0.1–20 GeV luminosity observed by *Fermi*-LAT. It follows a decaying power-law with an amplitude of $(5.1 \pm 0.2) \times 10^{52} \text{ erg s}^{-1}$ and index $\alpha_{\text{GeV}} = 1.19 \pm 0.04$. Details are given in Sections 4, 5 and 8.

The second sub-class corresponds to short bursts with $E_{\text{iso}} \gtrsim 10^{52} \text{ erg}$ and $E_{\text{p},i} \gtrsim 2 \text{ MeV}$. It was assumed that these sources, in analogy with the prototype GRB 090510, originate from a NS-NS merger in which the merged core overcomes the NS critical mass and gravitationally collapses to form a BH. We have called these sources genuine short GRBs (S-GRBs); see Ruffini et al. (2016a, 2019c); six of such short GRBs have been identified, all emitting GeV emission with a decaying luminosity of index $\alpha_{\text{GeV,short}} = -1.29 \pm 0.06$ (Ruffini et al. 2019c); see Fig. 11 in Section 8.

We show how, by following these pathfinding works on short GRBs, we have progressed in formulating the theory of the BdHN: the theory of long GRBs based on binary progenitors. Before this, however, we summarize the traditional long GRB models based upon a single progenitor.

1.4 Long GRBs in the traditional model

A review of the traditional long GRB model is facilitated by the extensive book by Bing Zhang and many references therein (Zhang 2018). As recounted there, the papers by Rees & Meszaros (1992); Mészáros & Rees (1997), and Woosley (1993) have characterized this traditional model. Rees & Meszaros (1992) proposed a single BH as the origin of GRBs emitting an ultrarelativistic blast wave, whose expansion follows the Blandford-McKee self-similar solution (Blandford & McKee 1976). Woosley (1993) linked the GRB origin to a Kerr BH emitting an ultrarelativistic jet originating from the accretion of toroidal material onto the BH. The BH was assumed to be produced from the direct collapse of a massive star, a “failed” SN leading to a large BH of approximately $5M_{\odot}$, possibly as high

as $10M_{\odot}$, a “collapsar”. We will address this interesting idea within our BdHN model in section 9.

In these ultrarelativistic blast wave models, the afterglow is explained by the synchrotron/synchrotron self-Compton (SSC) emission from accelerated electrons when the blast wave of $\Gamma \sim 1000$ is slowed down by the circumburst medium (Waxman & Piran 1994; Wijers et al. 1997; Sari & Piran 1995; Sari 1997; Sari et al. 1998).

As pointed out by Zhang (2018), these ultrarelativistic blast wave models have been applied to explain a vast number of observations:

- (i) The X-ray afterglow as well as the steep and shallow decay in the “Nousek-Zhang” phase, the X-ray and the gamma-ray flares.
- (ii) The optical and the radio emissions.
- (iii) The high-energy emission in the GeV band observed in some long GRBs by Fermi-LAT.

An example of this method is the recent case of GRB 190114C, in which the traditional approach has been applied:

- (i) to jointly explain the emissions in the TeV observed recently by MAGIC (R. Mirzoyan et al. 2019; MAGIC Collaboration et al. 2019a,b); see Fig. 3;
- (ii) to explain the emission in the MeV and GeV bands observed by the Fermi GBM and LAT satellites in the jetted emission;
- (iii) To explain the emission in the MeV and keV bands observed by *Swift* including the emission in the optical and radio.

In the traditional model, all of these emissions occur jointly using the kinetic energy of an ultrarelativistic blast wave with Lorentz factor $\Gamma \sim 10^3$, emitting at distances of $\sim 10^{16} \text{ cm}$ – 10^{18} cm , implying total energies reaching 10^{55} erg .

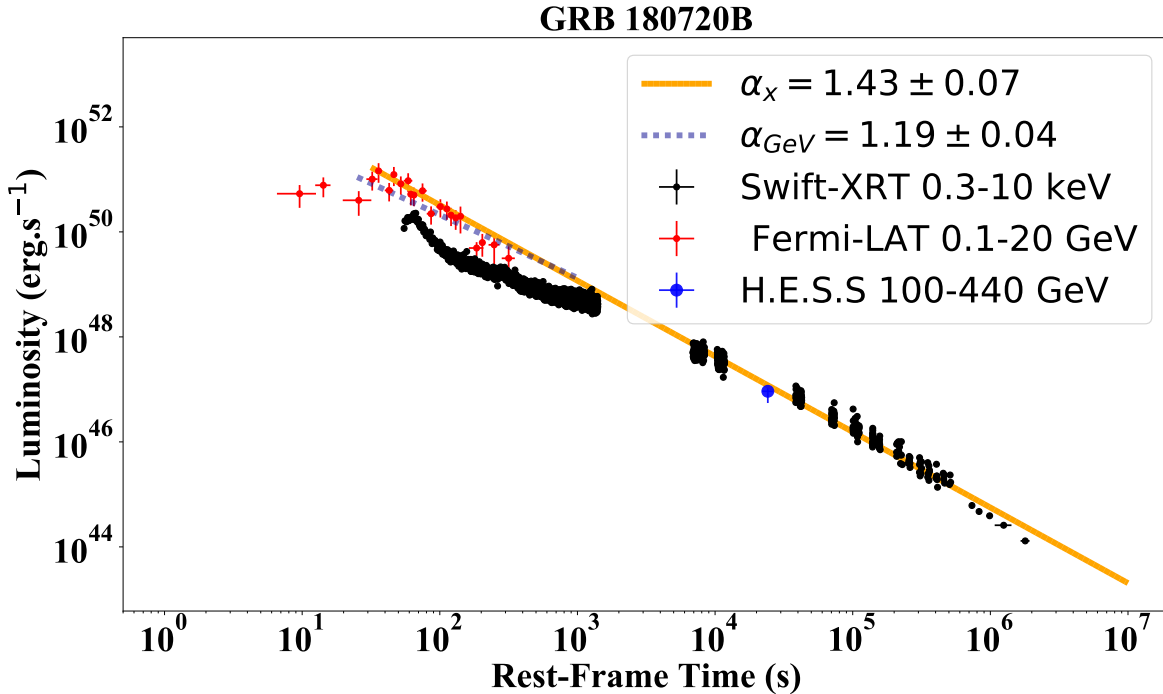


Figure 2. Luminosity of BdHN I 180720B: the black data points represent the rest-frame 0.3–10 keV luminosity obtained from *Swift*-XRT. It follows a decaying power-law with index $\alpha_x = 1.43 \pm 0.07$. The blue data point shows the rest-frame 100–440 GeV luminosity observed by H.E.S.S. The red data points show the rest-frame 0.1–20 GeV luminosity observed by *Fermi*-LAT. It follows a decaying power-law with amplitude $(5.4 \pm 0.6) \times 10^{52} \text{ erg s}^{-1}$ and index $\alpha_{\text{GeV}} = 1.19 \pm 0.04$. Details are given in Sections 4, 5 and 8.

This approach, however, encounters some contradictions with model-independent constraints. Moreover, there is no requirement that these different emission processes be explained by a single origin, i.e. the kinetic energy of a blast wave. As we are going to show in this article, each one of the above mentioned emissions finds its reason for existence in different specific processes originating in different specific episodes during the BdHN evolution. Each episode implies a different process and less demanding energy requirements.

1.5 The role of binary systems as progenitors of long GRBs

The role of binary systems as progenitors of long GRBs in our approach involves three assumptions:

A) That all long GRBs, not only the short GRBs, originate from binary systems. These binaries are composed of different combinations of CO_{core} , NS, white dwarfs (WDs), BH and νNS ; see Table 1. We classify all GRBs in nine different subclasses on the basis of their energetics, their spectra and their duration expressed in the rest-frame of the source. Only in *some* of these subclasses the presence of a BH occurs (see e.g. Ruffini et al. 2016b, 2018c; Wang et al. 2019); detail in section 2.

B) We focus on BdHNe with a binary progenitor composed of a CO-star and a companion binary NS. As the CO_{core} gravitationally collapses, it gives origin to a SN and its iron core collapses to form a newborn NS (νNS). The hypercritical accretion of the SN ejecta on the companion NS leads, for binary periods $\lesssim 5$ min, to the formation of a BH. This happens when the NS critical mass is reached and overcome (Becerra et al. 2016). We denote these sys-

tems as BdHNe I in which a BH is formed. The BdHNe I are characterised by an isotropic energy, estimated by the Fermi-GBM, in the range $10^{52} < E_{\text{iso}} < 10^{54}$ erg. In the opposite case, i.e. for longer binary periods, a more massive NS (MNS) originates from the SN hypercritical accretion process (Wang et al. 2019). These BdHNe II are characterised by $10^{50} < E_{\text{iso}} < 10^{52}$ erg (Ruffini et al. 2016b). The BdHNe III are characterized by binaries with even longer periods, so with more widely separated components, leading to an even weaker energy emission with $10^{48} < E_{\text{iso}} < 10^{50}$ erg.

C) We make use of recent theoretical results in the study of the hypercritical accretion of the SN ejecta both on the companion NS and the νNS (see e.g. Ruffini et al. 2016b; Becerra et al. 2016; Ruffini et al. 2018a; Becerra et al. 2019; Rueda et al. 2020). We rely on the three-dimensional (3D) simulations performed with a new Smoothed-Particle-Hydrodynamics (SPH) code developed in collaboration with Los Alamos National laboratory (see e.g. Becerra et al. 2019, and reference therein). We here give special attention to this procedure in order to reconstruct the morphology of the BdHNe, which has a strong dependence on the viewing angle as a result of the binary nature of the progenitor. We use the observations of the GeV emission observed by Fermi-LAT present only in *some* BdHN to infer their morphology and visualize its nature by SPH simulations; see section 6 and section 7 and Fig. 4.

1.6 The role of the binary progenitor in the SN associated with long GRBs

Contrary to the case of short GRBs, the necessity of a binary progen-

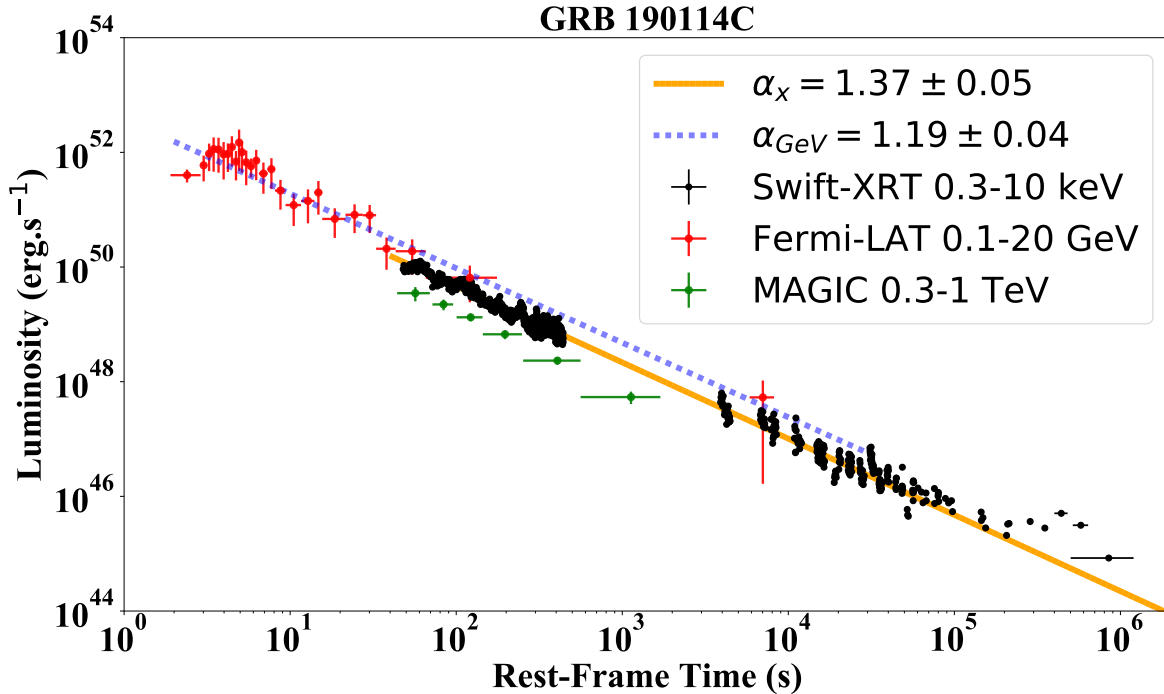


Figure 3. Luminosity of BdHN I 190114C: the black data points represent the rest-frame 0.3–10 keV luminosity obtained from *Swift*-XRT. It follows a decaying power-law with index $\alpha_x = 1.37 \pm 0.05$. The red data points show the rest-frame 0.1–20 GeV luminosity observed by *Fermi*-LAT. It follows a decaying power-law with amplitude $(4.6 \pm 0.6) \times 10^{52} \text{ erg s}^{-1}$ and index $\alpha_{\text{GeV}} = 1.19 \pm 0.04$. The green data points show the rest-frame 0.3–1 TeV luminosity obtained from MAGIC. Details are given in Sections 4, 5 and 8.

itor in long GRBs did not arise from the very beginning, and possibly the most important observational piece of evidence of this need can be identified in the temporal and spatial coincidence of GRB 980425 (Pian et al. 2000) and SN 1998bw (Galama et al. 1998), and the subsequent systematic spectroscopic analysis of additional GRB-SN associations (see Cano et al. 2017, for a review).

There are two key observational aspects of the SNe associated with GRBs pointing to a relevant role of binary interactions: 1) they are of type Ic, namely both hydrogen and helium lack in their spectra, and 2) the spectral lines are broad-lined implying their ejecta expand at very high expansion velocities of the order of 10^4 km s^{-1} , implying kinetic energies of up to 10^{52} erg , reason for which they have been dubbed HN (Cano et al. 2017).

The first feature, namely that these SNe are of type IC implies that they possibly originate from helium stars, CO_{core} , or Wolf-Rayet stars which have rid of their outermost layers (see, e.g., Smith et al. 2011). Indeed, it has been recognized that the a binary companion would most efficiently help in stripping off the pre-SN star outermost layers by tidal effects, multiple mass-transfer and common-envelope episodes (see, e.g., Nomoto & Hashimoto 1988; Iwamoto et al. 1994; Fryer et al. 2007; Yoon et al. 2010; Smith et al. 2011).

The second feature, namely the observed high-expansion velocities of the SN ejecta, is more delicate and less straightforward to account for in theoretical models. In the BdHN model, numerical simulations in Ruffini et al. (2018a) have shown that the explosion of the GRB within the SN might transfer to it sufficient energy and momentum to convert an initial ordinary SN into a HN. Therefore, broad-lined SNe or HNe in the BdHN model does not necessarily need to be born as such, instead they can be the outcome of the GRB

feedback into the SN (see also Becerra et al. 2019). Evidence of such a transition from a SN into a HN in a BdHN has been observationally identified in GRB 151027A (see Ruffini et al. 2018c, for details).

In addition, binary interactions may enforce corotation of the pre-SN star (i.e the CO_{core}) thereby spinning it up to high rotation rates. For BdHN I, this implies a rotation period of the CO_{core} of the order of minutes, so a rotational energy $\sim 10^{50} \text{ erg}$ (Wang et al. 2019). Of course, this can not explain directly an observed kinetic energy of 10^{52} erg . The core-collapse of the iron core of this rotating CO_{core} , by angular-momentum conservation, implies the birth of a millisecond period vNS, which may well power the SN by injecting into it energies of the order of 10^{52} erg (see Wang et al. 2019; Rueda et al. 2020, for more details). It may also happen that binary interactions spin up the CO_{core} beyond corotation bringing it to even to higher rotation rates $\sim 1 \text{ rad s}^{-1}$ (see, e.g., Nakamura et al. 2014; Gilkis 2018; Fujisawa et al. 2019), which would imply a much larger rotational energy of a few 10^{52} erg , ready to be used in the SN event.

There is increasing observational evidence on the high energetics of up to 10^{52} erg and the complex nature of the SN from the X- and gamma-ray precursors to the prompt radiation in long GRBs (see, e.g., Wang et al. 2019). In order to account for such a complexity, we have dubbed these early phases of the BdHN as “*SN-rise*” (Li et al. 2019). The *SN-rise* triggers the entire BdHN, so it includes the SN explosion as well as the feedback of the hypercritical accretion onto the vNS and onto the binary companion NS. We dedicate section 3 to their analysis giving examples in the case of BdHN I and II.

We can conclude that the binary progenitor of the BdHN model provides a natural explanation of the observational features of the SN associated with long GRBs. Having said this, it is now appropri-

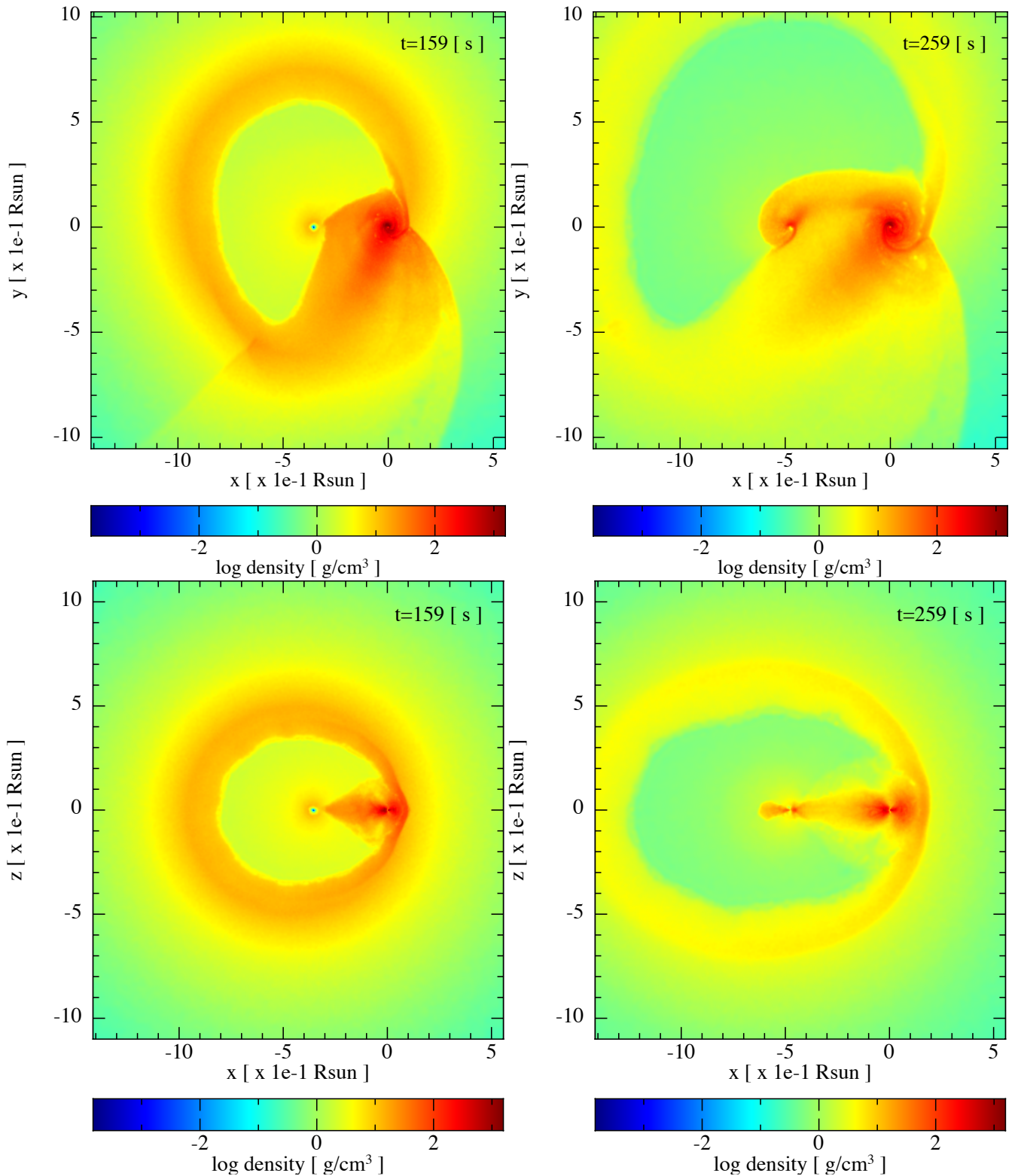


Figure 4. A SPH simulation from [Becerra et al. \(2019\)](#) of the exploding CO-star as the SN in the presence of a companion NS: Model “25m1p08E” (see table 2 therein). The CO-star is obtained from the evolution of a $25 M_{\odot}$ zero-age main-sequence (ZAMS) progenitor which leads to a pre-SN CO-star mass $M_{\text{CO}} = 6.85 M_{\odot}$. The initial mass of the ν NS (formed at the center of the SN) is $1.85 M_{\odot}$ and the one of the NS companion is $M_{\text{NS}} = 2 M_{\odot}$. The initial orbital period is 4.8 min. The upper panels show the mass density on the binary equatorial plane and the lower ones correspond to the plane orthogonal to it, at two selected times from the SN explosion ($t = 0$ of the simulation), 159 s and 259 s. The reference system is rotated and translated so that the x-axis is along the line that joins the ν NS and the NS, and the axis origin $(0,0)$ is located at the NS position. For this simulation, the NS collapses reaching the secular axisymmetric instability point with a mass $2.26 M_{\odot}$ and angular momentum $1.24 GM_{\odot}^2/c$, while the ν NS is stable with mass and angular momentum, respectively, $2.04 M_{\odot}$ and $1.24 GM_{\odot}^2/c$. Up to the final simulation time, the binary system kept bound although the binary orbit widens, reaching an orbital period of 16.5 min and an eccentricity of $\epsilon = 0.6$. The collapse of the NS to the newly-formed BH, characteristic of a BdHN I, occurs at $t = 21.6$ min.

ate to discuss the formation of the CO_{core}-NS binary progenitors of the BdHN from the stellar-evolution viewpoint.

It is well-known from the stellar evolution theory and observations that massive binaries might evolve to form binaries composed of compact objects, e.g. WD-WD, NS-WD, NS-NS and NS-BH. Leaving aside specific technical details, traditional evolutionary paths lead the compact remnant of the more massive star, after undergoing SN, to common-envelope phase with the companion, and after the collapse of the companion star leading to the second SN, the system forms a compact-object binary providing it keeps bound (Fryer et al. 1999; Dominik et al. 2012; Postnov & Yungelson 2014). It is very interesting that alternative evolutionary scenarios have been recently proposed in the X-ray binary and SN community leading to the so-called “ultra-stripped” binaries used to explain NS-NS and low-luminosity SNe (see e.g. Tauris et al. 2013, 2015, for details). The binary in these cases, after first SN, experiences multiple mass-transfer phases leading to the expulsion of the hydrogen and helium shells of the secondary. As proposed in Becerra et al. (2015); Fryer et al. (2015), these evolutionary scenarios are a plausible path to form CO_{core}-NS binary progenitors of BdHN.

From the above descends the question of whether such a population of binaries might or not include the progenitors of the BdHN. The orbital periods of the binary at the end of the evolution in these population synthesis codes are 50–5000 h (Tauris et al. 2013). They have been used as a main channel to form NS-NS, but the formation of NS-BH binaries, which are the final outcome left by BdHN I, have not been up to now considered in population synthesis numerical codes. One of the main reasons for this is that the physical processes involved in a BdHN I, occurring when shorter orbital periods of the order of minutes are allowed, lead to BH formation and they have not accounted for yet in these numerical codes. This is certainly a major research which deserves to be pursued in the near future.

We refer to Fryer et al. (2015) for additional details on the following estimation of the BdHN progenitor population. Ultra-stripped binaries are expected to be 0.1–1% of the total SN (Tauris et al. 2013), which is estimated to be $2 \times 10^4 \text{ Gpc}^{-3} \text{ y}^{-1}$ (see e.g. Guetta & Della Valle 2007). The population densities of BdHN II/III and BdHN I have been estimated to be $\sim 100 \text{ Gpc}^{-3} \text{ y}^{-1}$ and $\sim 1 \text{ Gpc}^{-3} \text{ y}^{-1}$, respectively (Ruffini et al. 2016b). The above numbers imply, for instance, that BdHN I would comprise only the 0.5% of the ultra-stripped binaries. These estimates confirm, in passing, the rareness of the GRB phenomenon.

Since 2018, our research on BdHN has acquired a different status by promoting technical progress in the visualization and in the data analysis, as well as in the introduction of new theoretical paradigms and identification of new astrophysical regimes which we further extend in this article. We start with a specific example of BdHN simulation.

1.7 A specific BdHN I SPH simulation

In Fig. 4, we show the results of a specific SPH simulation of a BdHN I from Becerra et al. (2019). It represents the implosion of a CO_{core} of $6.85M_{\odot}$ giving origin to the explosion of a SN in presence of a binary companion NS of $M_{\text{NS}} = 2M_{\odot}$. An additional NS of $1.85M_{\odot}$ originates from the collapse of the Fe-core within the CO_{core} (the green dot at the center of the SN in the two left figures). We indicate as vNS this newborn neutron star, in order to differentiate it from the binary companion NS. The two upper panels correspond to the mass density in the binary equatorial plane of the binary progenitor, which we label for short as “seen in the orbital plane”.

The lower panels correspond to viewing in a plane orthogonal to the equatorial plane of the binary progenitor, indicated for short as “seen from the top”. This figure well summarizes the central role of the SN in triggering the BDHN1 Phenomenon: by first creating the vNS and the accreting SN ejecta both on the vNS and the binary NS companion. The sequence of the accretion process is followed in these Figures 159 s and 259 s. Following the hypercritical accretion process the vNS reaches a mass and angular momentum, $2.04M_{\odot}$ and $1.24GM_{\odot}^2/c$, respectively. Up to the final simulation time. Similarly the binary NS companion collapses reaching the secular axisymmetric instability point with a mass of $2.26M_{\odot}$ and angular momentum $1.24GM_{\odot}^2/c$ at $t = 21.6$ min. In this model the initial binary period of the circular orbit is 4.8 min. The binary orbit then widens, reaching an orbital period of 16.5 min and an eccentricity of $\epsilon = 0.6$. We are going to give specific examples in selected GRBs of this process in section 10 with the determination of the mass and spin of the newborn BH. This figure is also essential in emphasizing the implications of the different viewing angles implied by the binary nature of the progenitors, which have been also neglected in the traditional approach.

We further exemplify, in the next two sections, the large amount of results inferred on the BdHN nature utilizing the two above viewing angles.

1.8 The upper limits on the Lorentz Γ factor and nature of the afterglow

The observations of BdHN I “seen in the orbital plane” have been addressed in a series of articles based essentially on the X-ray observations made with the XRT detector in Swift (see e.g., Ruffini et al. 2018a, and references therein). They have been essential in identifying model-independent upper limits on the Lorentz Γ factors of the emission regions during the gamma-ray flare, the X-ray flares phase, the flare-plateau and the early afterglow phases (the Nousek-Zhang phase), following the initial ultra-relativistic prompt radiation phase.

The traditional approach had shown that gamma-ray spikes in the prompt emission occur at $\sim 10^{15}$ – 10^{17} cm with Lorentz gamma factor $\Gamma \sim 10^2$ – 10^3 (e.g., Li 2020). Using a novel data analysis we have shown that the time of occurrence, duration, luminosity and total energy of the X-ray flares correlate with E_{iso} . A crucial feature has been identified in the observation of thermal emission in the X-ray flares that we have shown occurs at radii $\sim 10^{12}$ cm with $\Gamma \lesssim 4$. The upper limit of Lorentz factor, $\Gamma \lesssim 2$, has been there established in the analysis of the X-ray flares. Equally, an upper limit $\Gamma \lesssim 3$ has been set in the transition from a SN to a Hypernova (HN) in GRB 151027A (Ruffini et al. 2018c). Finally, the limit $\Gamma \lesssim 2$ has been established in the thermal emission in the early part of the afterglow phase of GRB 130427A (Ruffini et al. 2018b).

The enormous kinetic energy of an ultra-relativistic blast wave needed in the traditional approach to explain the energy source of the afterglow has been therefore superseded: the above mentioned stringent upper limits on the Γ factors exclude any ultra-relativistic motion.

The origin of the afterglow of long GRBs and these mildly-relativistic processes have been successfully identified in the synchrotron emission produced by relativistic electrons in the SN ejecta, powered by the hypercritical accretion of the SN into the spinning vNS of $1.5 M_{\odot}$ and its pulsar-like emission (Ruffini et al. 2018b; Wang et al. 2019; Rueda et al. 2020). From the amplitude of their decaying X-ray luminosities observed by *Swift*-XRT (Pisani et al. 2016) the spin of the vNS and the strength and structure of its mag-

Extended wording	Acronym
Binary-driven hypernova	BdHN
Black hole	BH
Carbon-oxygen star	CO-star
fallback-powered kilonova	FB-KN
Gamma-ray burst	GRB
Gamma-ray flash	GRF
gamma-ray flash kilonovae	GR-K
Massive neutron star	M-NS
Neutron star	NS
New neutron star	vNS
Short gamma-ray burst	S-GRB
Short gamma-ray flash	S-GRF
Supernova	SN
Supernova rise	SN-rise
Ultrashort gamma-ray burst	U-GRB
White dwarf	WD
X-ray flash	XRF

Table 1. Alphabetic ordered list of the acronyms used in this work.

netic field in specific BdHN I and II have recently been obtained (Rueda et al. 2020).

It is important that the synchrotron process occurring in the interaction of the SN ejecta with the vNS, requires a much smaller energy to explain the nature of the afterglow in our present approach based on the hypercritical accretion of from the SN onto the vNS (Wang et al. 2019; Rueda et al. 2020) than the ones purported in the ultrarelativistic blast waves.

1.9 The “inner engine” of BdHN I

The observations of the BdHN I “seen from the top” are the main topic of this article. They lead to an identification of the morphology of BdHN I, to the origin of the MeV, GeV, and TeV emissions observed by the GBM and LAT instruments on board the Fermi satellite, the MAGIC and the H.E.S.S. telescopes, as well as to a contribution to ultrahigh-energy cosmic rays (UHECRs) from GRBs (see, e.g., Rueda & Ruffini 2020). Particularly important has been the recent identification of the physical process occurring in the “inner engine” originating the GeV emission as “seen from the top” in GRB 130427A, also confirmed in three additional BdHN I GRB 160509A, GRB 160625B and GRB 190114C (Ruffini et al. 2019c; Li et al. 2019).

In these works:

(i) We have proposed that the *inner engine* of a BdHN I is composed of a Kerr BH in a non-stationary state, embedded in a uniform magnetic field B_0 aligned with the BH rotation axis, as modeled by the Papapetrou-Wald solution of the Einstein-Maxwell equations (Papapetrou 1966; Wald 1974), and surrounded by an extremely-low density ionized plasma of 10^{-14} g cm $^{-3}$. Using GRB 130427A as a prototype, we have shown that this *inner engine* acts in a sequence of *elementary impulses* emitting “*blackholic quanta*” (Rueda & Ruffini 2020). The repetition time of the emission of each “*blackholic quantum*” of energy $\mathcal{E} \sim 10^{37}$ erg, is $\sim 10^{-14}$ s at the beginning of the process. Then, it slowly increases with the time evolution. Electrons are accelerated to ultra-relativistic energy near the BH horizon and, propagate along the polar axis, $\theta = 0$. They can reach energies of $\sim 10^{18}$ eV, and partially contribute to ultra-high energy cosmic rays (UHECRs). When propagating along $\theta \neq 0$ through the magnetic field B_0 they give rise to the synchrotron emission of GeV and TeV photons. The *inner engine* operates within a “cavity” formed during

the hypercritical accretion of the SN ejecta onto the NS binary companion, and during the BH formation (Ruffini et al. 2019b). This result is the first step toward identifying the BdHN I morphology, presented in this article.

(ii) It has been shown that the multiwavelength emissions corresponding to the above acceleration process leading to synchrotron radiation occur in a jet with a half-opening angle of 60° from the normal to the binary plane. The jetted emission occurs in selected energy bands in the MeV, GeV, TeV and UHECR.

(iii) This result has been applied to GRB 130427A, and we here show that it applies generally to all BdHN I as a consequence of the novel morphology identified in the present article.

(iv) We have evaluated the total GeV emission in GRB 130427A and identified its decaying luminosity in the GeV range with a power-law index of $\alpha_{\text{GeV}} = -1.19 \pm 0.04$, using the first and the second *Fermi*-GRB catalogs (Ackermann et al. 2013; Ajello et al. 2019). In this article we generalize this result to all BdHN I emitting GeV radiation.

1.10 On the measure of the BH mass and spin in BdHN I

For the first time, in Ruffini et al. (2019c) it was shown how to extract the rotational energy of a Kerr BH in an astrophysical system, using GRB 130427A as a prototype. This was made possible making use of the the mass-energy formula of the Kerr BH (Christodoulou 1970; Christodoulou & Ruffini 1971; Hawking 1971; Hawking 1972), given in Eq. (1a). There, it was shown how through the “*inner engine*” activity the energetics of the GeV emission could originate near the BH horizon and be explained using the extractable energy of the BH, keeping constant the BH *irreducible mass*. In turn, this has led to the first measure of the initial mass and spin of the BH at its moment of formation: $M = 2.3M_\odot$, its spin, $\alpha = a/M = 0.47$. The present article is dedicated to extend this classic result to all BdHN I, where sufficient GeV emission data are available. This same procedure will be soon extended to active galactic nuclei with BH masses up to $10^{10}M_\odot$.

1.11 Structure of the article

We first give in section 2 an outline of the nine GRB subclasses presented in Ruffini et al. (2016b), with a brief summary of their initial states (*in-state*), their final state (*out-state*), their energetics and spectral properties in the gamma-rays both in the MeV and in the GeV emissions. We also recall the binary mergers which include the NS-NS binaries leading to the two classes of short GRBs.

In section 3, we summarize the previous results (Li et al. 2019) on the analysis of the SN-rise of BdHNe I and II obtained from *Fermi*-GBM, and present their relation with the X-ray afterglow observed by *Swift*-XRT.

In section 4, following our previous works (Ruffini et al. 2018b; Wang et al. 2019; Rueda et al. 2020), we study properties of the X-ray afterglow of BdHNe and we determine the spin of the vNS in two BdHNe I, two BdHNe II and one BdHN III system.

In section 5, we analyze the properties of the GeV emission in BdHNe I updated following the second GRB catalog presented by Fermi-LAT, which covers the first 10 years of its operations, from 2008 August 4 to 2018 August 4 (Ajello et al. 2019). We address the 378 BdHNe I with known cosmological redshift; see the list of BdHNe I in Pisani et al. (2016); Ruffini et al. (2018a) and also the updated list in Appendix A. We then consider only the 54 BdHN I with the boresight angle of *Fermi*-LAT smaller than 75° at the trigger time. We give the details of the 25 BdHNe I with observed GeV

radiation, out of the 54. For each of them, we list in Table 5 the cosmological redshift, the $E_{p,i}$ of the spectrum, the $E_{\gamma,iso}$ of the source, the *Fermi* GCN, the boresight angle, the E_{LAT} , the likelihood test statistic (TS), and some additional distinguishing properties. In Table 6 for the 29 BdHNe I, we then give the cosmological redshift, the $E_{p,i}$ of the spectrum, the $E_{\gamma,iso}$ of the source, the *Fermi* GCN, the boresight angle and some distinguishing properties of the associated X-ray emissions.

In section 6, we explain the nature of these BdHNe in terms of a novel morphology of the binary system. The BdHN I have a conical structure normal to the equatorial plane of the binary progenitor. When the observations are made with a viewing angle lying in the orbital plane of the binary progenitor then the GeV emission is not observable. In this case, only the gamma-ray flare, the X-ray flares and the X-ray plateau remain observable. From the ratio $N_{LAT}/N_{tot} = 25/54$, we infer the presence in the BdHN I of a conical structure of approximately 60° around the normal to the plane of the binary progenitors. Within this cone all emissions are observable, namely the X-ray, the gamma-ray, the GeV and TEV emission also UHECRs. For larger inclination angle as confirmed theoretically in Ruffini et al. (2018c, 2019c), the GeV radiation is not observable and only flaring activities are observed following the prompt radiation phase.

In section 7, we show that this novel geometry is indeed present in the recent three-dimensional SPH numerical simulations at the moment of BH formation in a BdHN (Becerra et al. 2019).

In section 8, for each of the 25 BdHNe I, we provide the 0.1–10 GeV luminosity light-curves as a function of the time in the rest-frame of the source. We obtain a power-law fit $L_n = A_n t^{-1.19 \pm 0.04}$ erg s $^{-1}$ and report the amplitude A_n and the luminosity at 10 s from the beginning of the prompt radiation, L_{10s} , with their associated uncertainties. We also provide a correlation between L_{10s} and $E_{\gamma,iso}$.

In section 9, we determine the values of the mass and spin of the BH and the strength of the magnetic field surrounding the BH in the “inner engine” of the selected BdHNe I. We also show the process of hypercritical accretion of the SN on a companion NS gives in all cases origin to the newborn BH.

In section 10, we confirm 1) the central role of the SN in giving rise to its hypercritical accretion on the vNS and the newly born BH, to the afterglow observed by SWIFT and to the high energy GeV and TeV emission observed by *Fermi*-LAT, 2) that the MeV-GeV energetic range is explainable by extractable rotational energy of a Kerr BH operating in the “inner engine” and this result allows the determination of the initial mass and spin of the BH, 3) the power-law evolution of the 0.1–100 GeV luminosity after the prompt phase, arises from the slowing down rate of the BH spin, keeping constant the irreducible mass M_{irr} of the BH.

We finally proceed to the general conclusions in section 11. Before proceeding, we indicate in Table 1 the alphabetic ordered list of acronyms used in this work.

2 SUBCLASSES OF GRBS AND DEFINITIONS OF BDHN

We address the specific role of the X-ray emission observed by the *Swift* satellite as well as the MeV-GeV radiation observed by the *Fermi* satellite in order to further characterize the nine subclasses of GRBs presented in Ruffini et al. (2016b) and updated in Ruffini et al. (2018a); Wang et al. (2019), and here further updated in section 4 and Appendix A. In Table 2, we summarize for each GRB sub-

class their name, the number of observed sources with cosmological redshift, and their progenitors characterizing their “in-state”.

In all cases the GRB progenitors are binary systems composed of various combinations of CO_{core}, of NSs, of WDs, and of BHs. The “out-state” of the corresponding mergers or accretion processes have been represented in Fig. 7 in Ruffini et al. (2016b) where we also presented the interesting possibility that “out-states” of the GRB subclasses can become the “in-states” of new GRB subclasses. In particular, we indicate an example in which the “out-state” of a BdHN I can become the “in-state” of a short GRB.

In this article, we focus only on long GRBs with BdHN progenitors (Ruffini et al. 2016b): binary systems composed of a CO_{core}, exploding as SN Ic, and a NS binary companion. The presence of such a NS binary companion in close orbit can explain the removing of the outer layers of Hydrogen and Helium of the massive star leading to the CO_{core} (see, e.g., Ruffini et al. 001c; Rueda & Ruffini 2012; Fryer et al. 2014).

As noted in the introduction, when the CO_{core} gravitationally collapses, it gives origin to a SN and its Fe core collapses to form a vNS. The entire dynamics and evolution of the BdHN is essentially based on these three different components and their interplay: the SN explosion (SN-rise), the vNS undergoing an overcritical accretion process of the SN ejecta, the binary companion NS also undergoes an overcritical accretion process of the SN ejecta which monotonically increases the binary NS companion mass. In compact binary systems, this accretion causes the NS to obtain its critical mass leading to the formation of a newborn BH (Becerra et al. 2015, 2016); see also Fig. 4.

We first address the SN hypercritical accretion onto the binary NS companion: the outcome is a strong function of the compactness of the binary system and its binary orbital period.

When the orbital period is as short as 5 min, the hypercritical accretion proceeds at higher rates and the companion NS reaches its critical mass leading to:

- (i) the formation of a BH and consequently a formation of a new binary system composed of a BH and a vNS (Fryer et al. 2014);
- (ii) the emission of a very energetic GRB in the range of $10^{52} \lesssim E_{iso} \lesssim 10^{54}$ erg and, peak energy in the range of $0.2 \text{ MeV} < E_{p,i} < 2 \text{ MeV}$ lasting a few seconds known as the ultra relativistic prompt emission phase (UPE);
- (iii) the onset of the prolonged power-law GeV emission, triggered by the formation of the newborn BH, with a luminosity described in the rest frame of the source

$$L_{GeV} = A_{GeV} \left(\frac{t}{1 \text{ s}} \right)^{-\alpha_{GeV}}, \quad (2)$$

with $\alpha_{GeV} = 1.19 \pm 0.04$. One of the main results in this paper is to show that this radiation is present only in a subset of BdHN and the explanation of this result will lead to the determination of the conical BdHN morphology, see section 8.

These systems have been indicated as BdHN I (Ruffini et al. 2015b; Becerra et al. 2015, 2016; Ruffini et al. 2016b; Wang et al. 2019; Ruffini et al. 2019c).

The first list of the BdHNe I was composed of 161 sources spanning 12 years of *Swift*/XRT observation activity till 2015 presented in Pisani et al. (2016) which was further extended to 173 sources in Ruffini et al. (2018a) up through the end of 2016 which led to a total of 345 BdHNe I within 1997–2016 observed by other satellites like *Fermi* and *Konus*-WIND in addition to *Swift*. This list is further extended here to 378 BdHN I till Dec. 2018; see Appendix. A; see Table 2.

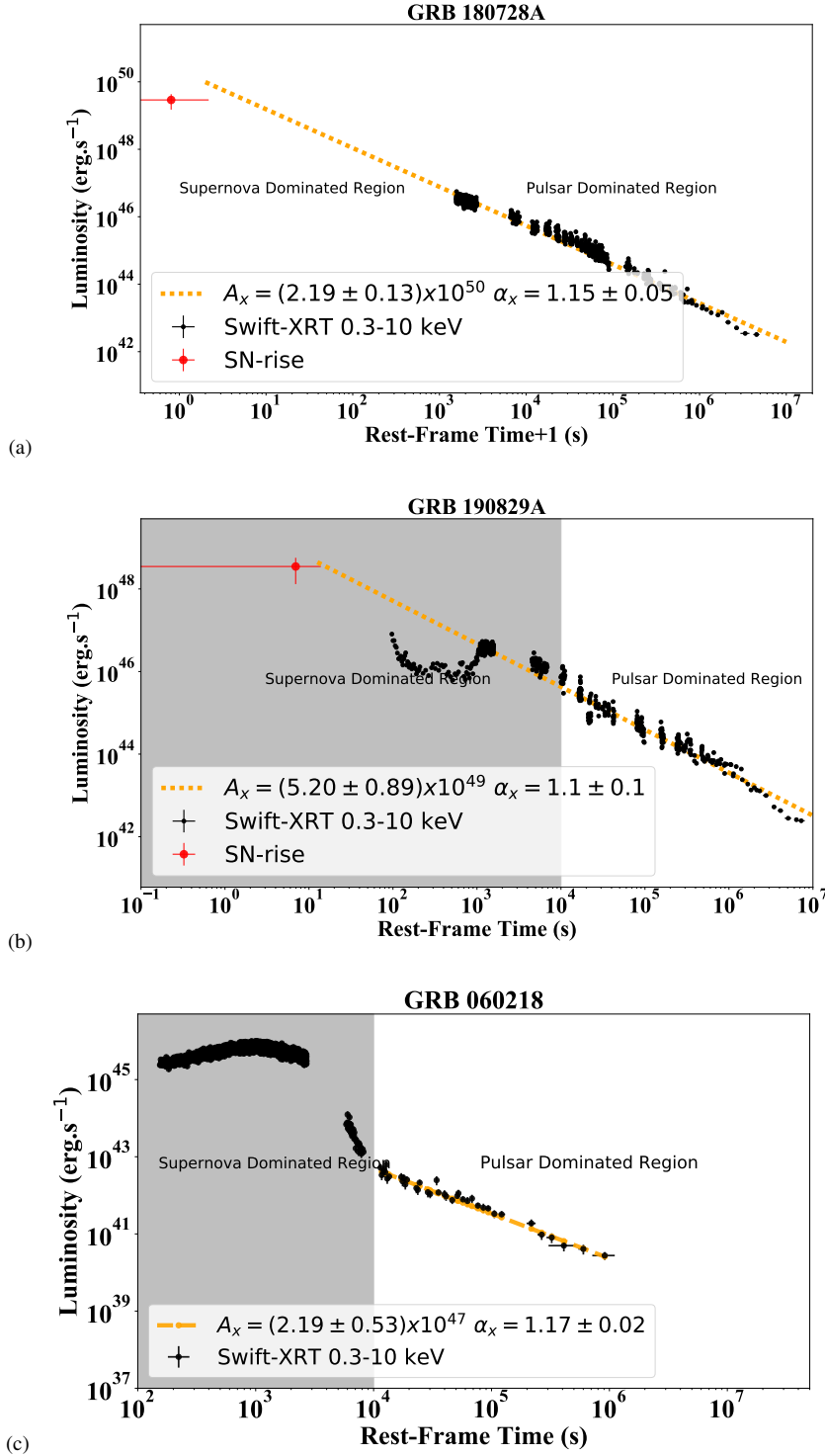


Figure 5. The X-ray afterglow luminosity observed by *Swift*-XRT which follow a decaying power-law: **a:** GRB 180728A (BdHN II) with amplitude $(2.19 \pm 0.13) \times 10^{50} \text{ erg s}^{-1}$ and power-law index $\alpha_X = 1.15 \pm 0.05$. **b:** GRB 190829A (BdHN II) with amplitude $(5.20 \pm 0.89) \times 10^{49} \text{ erg s}^{-1}$ and power-law index $\alpha_X = 1.1 \pm 0.1$. **c** GRB 060218 (BdHN III) with amplitude $(2.19 \pm 0.53) \times 10^{47} \text{ erg s}^{-1}$ and power-law index $\alpha_X = 1.17 \pm 0.02$. The fallback material of the SN on the ν NS produce this X-ray afterglow emission (Rueda et al. 2020). In section 4.1, we report the result of the simultaneous fit of the X-ray afterglow of all types of BdHN in order to find the universal power-law index. As shown in Ruffini et al. (2018a,c), until $\sim 10^4 \text{ s}$ the gamma/X-ray afterglow is mainly produced by the SN kinetic energy (*SN dominated region*) and its interaction with the magnetic field of the ν NS. After 10^4 s , as shown by Ruffini et al. (2018b), the role of ν NS becomes prominent (*pulsar dominated region*).

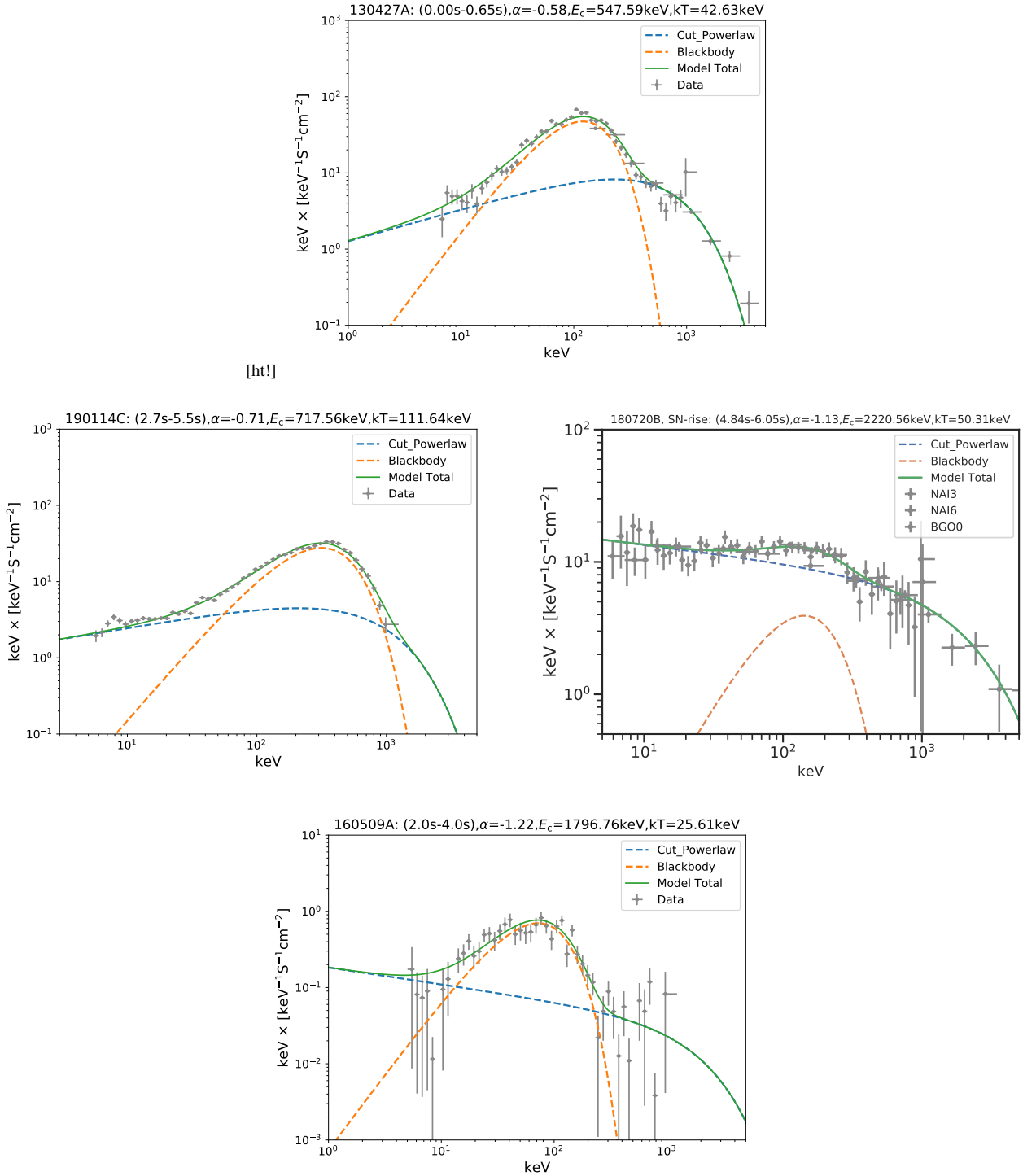


Figure 6. The Spectrum of the SN-rise of GRB 160509A as observed by Fermi-GBM in the energy range of 8–900 keV. **Upper left:** SN-rise spectrum of BdHN I 130427A, well fitted by a CPL+BB model, from 0 to 0.65s ($t_{\text{rf}} \simeq 0.49\text{s}$); the spectral index α is -0.58, cutoff energy E_c is 547.59 keV, and the BB temperature is 42.63 keV in the observer’s frame. **Upper right:** The spectra of SN-rise of BdHN I 190114C corresponding to $t = 1.12\text{s}$ ($t_{\text{rf}} = 0.79\text{s}$) to $t = 1.68\text{s}$ ($t_{\text{rf}} = 1.18\text{s}$), which is best fit by a CPL+BB model, with a low-energy photon index α of -0.71, and a peak energy E_c of 524.7 keV, and a BB temperature 18.42 keV. Time is reported in both the observer’s frame and the rest-frame. Spectral parameters of the best fit are presented in the observer’s frame. **Lower left:** SN-rise spectrum of BdHN I 180720B, well fitted by a CPL+BB model, from 4.84 to 6.05s ($t_{\text{rf}} \simeq 0\text{s}$); the spectral index α is -1.13, cutoff energy E_c is 2220.56 keV, and the BB temperature is 50.31 keV in the observer’s frame. **Lower right:** SN-rise spectrum of BdHN I 160509A, well fitted by a CPL+BB model, from 2.0 to 4.0s ($t_{\text{rf}} \simeq 0\text{s}$); the spectral index α is -1.22., cutoff energy E_c is 1796.76 keV, and the BB temperature is 25.66 keV in the observer’s frame.

Class	Type	Number	<i>In-state</i>	<i>Out-state</i>	$E_{p,i}$ (MeV)	$E_{\gamma,iso}$ (erg)	$E_{iso,GeV}$ (erg)
Binary Driven Hypernova (BdHN)	I	378	CO star-NS	vNS-BH	$\sim 0.2-2$	$\sim 10^{52}-10^{54}$	$\gtrsim 10^{52}$
	II	(49)	CO star-NS	vNS-NS	$\sim 0.01-0.2$	$\sim 10^{50}-10^{52}$	–
	III	(19)	CO star-NS	vNS-NS	~ 0.01	$\sim 10^{48}-10^{50}$	–
	IV	0	CO star-NS	BH	–	$> 10^{54}$	$\gtrsim 10^{53}$
Binary Merger (BM)	I	18	NS-NS	MNS	$\sim 0.2-2$	$\sim 10^{49}-10^{52}$	–
	II	6	NS-NS	BH	$\sim 2-8$	$\sim 10^{52}-10^{53}$	$\gtrsim 10^{52}$
	III	(1)	NS-WD	MNS	$\sim 2-2$	$\sim 10^{49}-10^{52}$	–
	IV	(1)	WD-WD	NS/MWD	< 0.2	$< 10^{51}$	–
	V	(0)	NS-BH	direct BH	$\gtrsim 2$	$> 10^{52}$	–

Table 2. Summary of the GRB subclasses. In addition to the subclass name, we report the number of GRBs for each subclass. We recall as well the “in-state” representing the progenitors and the “out-state” as well as the $E_{p,i}$ and $E_{\gamma,iso}$ for each subclass. The GeV emission is indicated in the last column: for long GRBs it appears only in BdHN I and BdHN IV (BH-SN) while, for short bursts, it appears only for S-GRBs. In all sources with GeV emission, it is $\gtrsim 10^{52}$ erg.

When the orbital period of the binary system is $\gtrsim 5$ min, the hypercritical accretion is not sufficient to trigger the collapse of the NS companion into a BH: therefore no GeV emission can be produced nor be observed. Therefore, a MNS is formed. In these systems, the observed peak energy is in the range $4 \text{ keV} < E_{p,i} < 300 \text{ keV}$ and the isotropic energy in the range of $10^{48} \lesssim E_{iso} \lesssim 10^{52}$ erg, as observed by the Fermi-GBM. They have been indicated as X-ray flashes (XRF) in contrast with the more energetic BdHN I (Ruffini et al. 2015b; Becerra et al. 2015, 2016; Ruffini et al. 2016b). We here use for the XRFs the name BdHN II, according to Wang et al. (2019). A canonical example has been given in Wang et al. (2019); see Table. 2.

BdHN III have the same composition as BdHN II, but the binary is further detached. No BH is formed and no GeV radiation is produced nor observed. This subclass is characterized by binary systems widely separated and weaker energy emission with E_{iso} in the range of $10^{48}-10^{50}$ erg.

As we will see in section 10, the most energetic BdHN I originate from extremely tight binary systems with the companion NS grazing the radius of the CO_{core} . It is therefore conceivable that in some systems the NS companion merges with the CO_{core} just prior to the SN explosion leading to the possible direct formation of a BH, a concept envisaged by Woosley (1993) in the failed SN scenario. We have left such a possibility opened in an additional BdHN IV family; see Table 2.

The hypercritical accretion of the SN ejecta onto the vNS leads to the pulsar-like emission which gives rise to the X-ray afterglow emission observed by Swift (Rueda et al. 2020). This is a property intrinsic to the nature of the model and shared by all BdHN subclasses. It is therefore natural to expect, as has been verified, that the luminosity of the X-ray afterglows of *all* long GRBs, in all BdHN subclasses, follow a common decaying power-law of

$$L_X = A_X \left(\frac{t}{1s} \right)^{-\alpha_X}, \quad (3)$$

with $\alpha_X = 1.48 \pm 0.32$, including the SN-rise, when averaged over all BdHN I up to 10^6 s (Pisani et al. 2016). The different amplitudes, A_X , and power-law indices, α_X , of the X-ray afterglow luminosity can be used to determine the spin and magnetic field of the vNS (Wang et al. 2019; Rueda et al. 2020).

Before leaving this topic, we mention a few cases of X-ray afterglows in BdHN II and BdHN III. Each BdHN II and BdHN III will be also characterized by an x-ray afterglow originating from the accretion of the SN ejecta into the vNS. Their power-law index α_X coincides with the one of BdHN I, although the difference in the total angular momentum of the binary progenitors and its conservation leads necessarily to a smaller value of the amplitude A_X in Eq. (3), to a corresponding lower value of the vNS spin and to a smaller value of the SN-rise; see Fig.5.

In the rest of this article, we mainly examine the properties of BdHN I with special attention to:

- (i) their SN-rise emission;
- (ii) the power-law decay of the X-ray emission of the afterglow observed by Swift, measured in the cosmological rest-frame of the source;
- (iii) the corresponding GeV emission observed by Fermi-LAT, centering on the identification of the BdHN morphology to explain the absence of this emission in a subclass of BdHN I.

3 THE SN-RISE IN BDHN I AND BDHN II: FERMI OBSERVATION

The trigger of all BdHN is represented by the gravitational collapse of the CO_{core} which gives origin to a SN and its Fe-core collapses to form a vNS. We have indicated the first appearance of the SN as the SN-rise. In BdHN I, the SN-rise is characterized by the presence of the thermal component in the Fermi-GBM data with isotropic energy of $\sim 10^{52}$ erg; see Ruffini et al. (2019a); Li et al. (2019); Fryer et al. (2014). In BdHN II, the SN-rise is weaker and has no thermal component in the Fermi-GBM data with energy of $\sim 10^{50}$ erg; see Wang et al. (2019); Ruffini et al. (2019a); Li et al. (2019), Fig. 6 and Table 2. In this article, we just recall the observation of the SN-rise in 4 BdHN I: GRB 130427A, GRB 160509A, GRB 180720B and GRB 190114C, as well as in two BdHN II: GRB 180728A and GRB 190829A. In Fig. 6 we show the spectra of the SN-rise in the aforementioned sources and in Fig. 7 we show their corresponding luminosity.

4 THE AFTERGLOWS OF BDHN I, BDHN II AND BDHN III: THE SWIFT OBSERVATIONS

Following the CO_{core} gravitational collapse and the appearance of the SN-rise, which characterizes all BdHN subclasses, the hypercritical accretion of the SN ejecta onto the vNS and the magnetic field of the vNS leads to the pulsar-like emission powering the X-ray afterglow observed by the Swift satellite (Rueda et al. 2020).

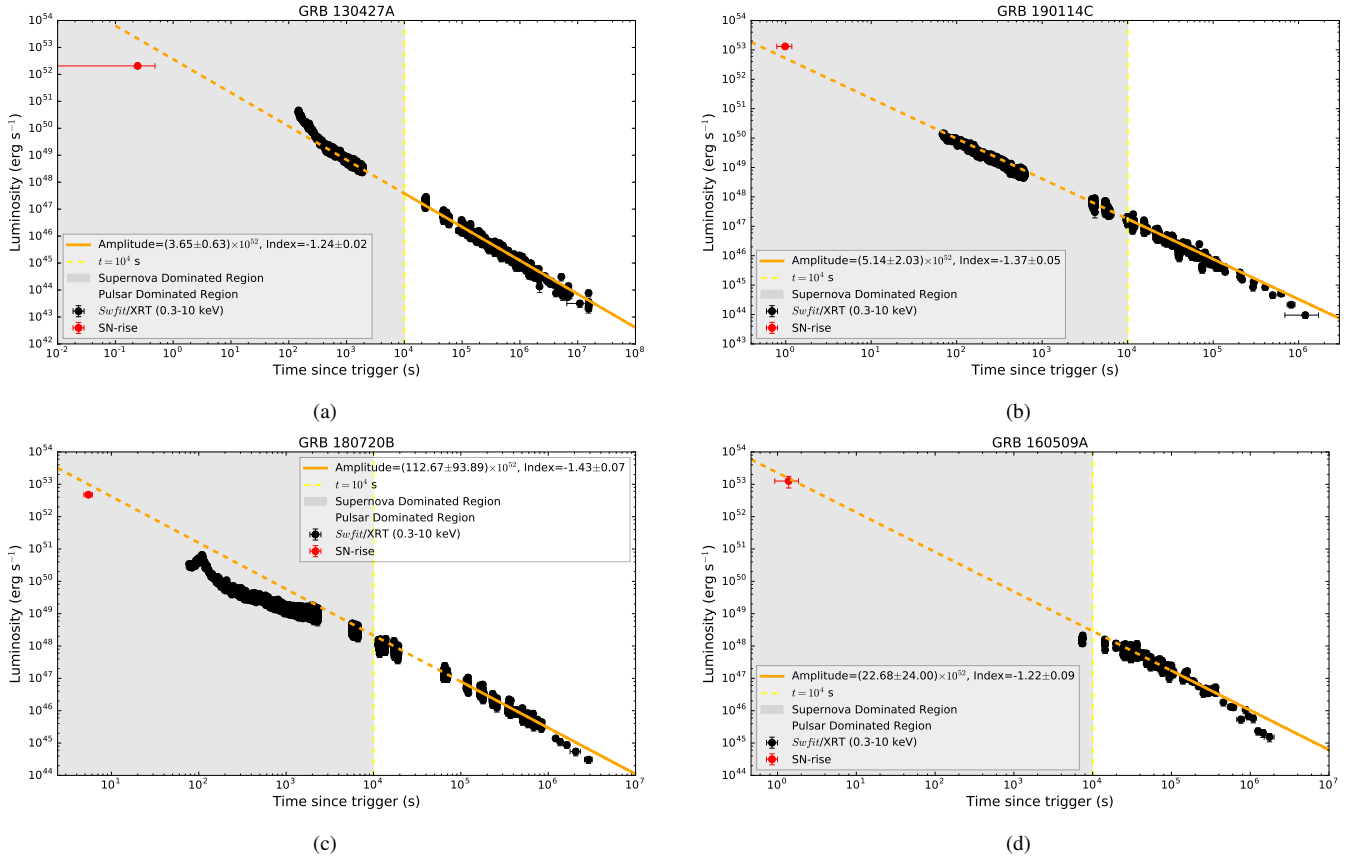
We present four afterglows of BdHN I (Fig. 7), two afterglows of BdHN II, and one afterglow of BdHN III (Fig. 5). In each case, we also reproduce the SN-rise presented in the previous section; see Figs. 5 and 7.

The BdHN I in GRB 130427A, GRB 190114C, GRB 180720B and GRB 160509A follow a decaying luminosity consistent with Eq. (3); see Fig. 7:

- GRB 130427A with amplitude $(3.65 \pm 0.63) \times 10^{52} \text{ erg s}^{-1}$ and power-law index $\alpha_X = 1.24 \pm 0.02$;

Table 3. The properties of the SN-rise in BdHN I: GRB 190114C, GRB 130427A, GRB 160509A, and GRB 160625B; and the properties of the SN-rise in BdHN II: GRB 180728A.

GRB	$t_1 \sim t_2$ (s) (Observation)	Duration (s) (Rest)	Flux ($\text{erg cm}^{-2} \text{s}^{-1}$) (SN-rise)	E_{sh} (10^{52} erg) (SN-rise)	E_{iso} (erg) (Total)	Temperature (keV) (Rest)	redshift	Reference (For SN-rise)
190114C	1.12~1.68	0.39	$1.06^{+0.20}_{-0.20} (10^{-4})$	$2.82^{+0.13}_{-0.13}$	$(2.48 \pm 0.20) \times 10^{53}$	$27.4^{+45.4}_{-25.6}$	0.424	A. Melandri et al. (2019)
130427A	0.0~0.65	0.49	$2.14^{+0.28}_{-0.26} (10^{-5})$	$0.65^{+0.17}_{-0.17}$	$\sim 1.40 \times 10^{54}$	$44.9^{+1.5}_{-1.5}$	0.3399	Xu et al. (2013)
160509A	2.0~4.0	0.92	$1.82^{+1.23}_{-0.76} (10^{-6})$	$1.47^{+0.6}_{-0.6}$	$\sim 1.06 \times 10^{54}$	$25.6^{+4.8}_{-4.7}$	1.17	Tam et al. (2017)
160625B	0~2.0	0.83	$6.8^{+1.6}_{-1.6} (10^{-7})$	$1.09^{+0.2}_{-0.2}$	$\sim 3.00 \times 10^{54}$	$36.8^{+1.9}_{-1.9}$	1.406	This paper
180728A	-1.57 ~ 1.18	0.83	$4.82^{+1.16}_{-0.82} (10^{-8})$	$7.98^{+1.92}_{-1.34} \times 10^{49}$	$2.76^{+0.11}_{-0.10} \times 10^{51}$	-	0.117	Izzo et al. (2018)

**Figure 7.** X-ray afterglow luminosities of four BdHNe I observed by *Swift*-XRT which follow a decaying power-law: (a): GRB 130427A (BdHNe I) with amplitude $(3.65 \pm 0.63) \times 10^{52} \text{ erg s}^{-1}$ and power-law index $\alpha_X = 1.24 \pm 0.02$. (b): GRB 190114C with amplitude $(5.14 \pm 2.03) \times 10^{52} \text{ erg s}^{-1}$ and power-law index $\alpha_X = 1.37 \pm 0.05$. (c): GRB 180720B with amplitude $(112.67 \pm 93.89) \times 10^{52} \text{ erg s}^{-1}$ and power-law index $\alpha_X = 1.43 \pm 0.07$. (d): GRB 160509A with amplitude $(22.68 \pm 24.00) \times 10^{52} \text{ erg s}^{-1}$ and power-law index $\alpha_X = 1.22 \pm 0.09$. The red points show the luminosity of SN-rise in each BdHN. The fallback of material from the SN onto the vNS produces this X-ray afterglow emission ([Rueda et al. 2020](#)). As shown in [Ruffini et al. \(2018a,c\)](#), till $\sim 10^4$ s the gamma/X-ray afterglow is mainly produced by the SN kinetic energy (*SN dominated region*) and its interaction with the magnetic field of the vNS. After 10^4 s, as shown by [Ruffini et al. \(2018b\)](#), the role of vNS becomes prominent (*pulsar dominated region*).

- GRB 160509A with amplitude $(22.68 \pm 24.00) \times 10^{52} \text{ erg s}^{-1}$ and power-law index $\alpha_X = 1.22 \pm 0.09$;
- GRB 180720B with amplitude $(112.67 \pm 93.89) \times 10^{52} \text{ erg s}^{-1}$ and power-law index $\alpha_X = 1.43 \pm 0.07$;
- GRB 190114C with amplitude $(5.14 \pm 2.03) \times 10^{52} \text{ erg s}^{-1}$ and power-law index $\alpha_X = 1.37 \pm 0.05$

The BdHNe II in GRB 180728A and GRB 190829A follow a decaying luminosity consistent with Eq. (3) (see [Wang et al. 2019](#) and Wang, et al., in preparation); see Fig. 5(a) and (b):

- GRB 180728A with amplitude $(2.19 \pm 0.13) \times 10^{50} \text{ erg s}^{-1}$ and power-law index $\alpha_X = 1.15 \pm 0.05$;

- GRB 190829A with amplitude $(5.20 \pm 0.89) \times 10^{49} \text{ erg s}^{-1}$ and power-law index $\alpha_X = 1.1 \pm 0.1$.

As an example of the X-ray afterglow luminosity of a BdHN III, we indicate the case of GRB 060218 where the X-ray luminosity, as in the case of BdHNe I and II, follows a decaying power-law consistent with Eq. (3), with an amplitude $(2.19 \pm 0.53) \times 10^{47} \text{ erg s}^{-1}$ and power-law index $\alpha_X = 1.17 \pm 0.02$. This is consistent with $\alpha_X = 1.2 \pm 0.1$ obtained by [Campana et al. \(2006\)](#); see Fig. 5(c).

We can then reach the following general conclusions:

- The X-ray afterglow is present in all three BdHN subclasses: BdHN I, BdHN II, BdHN III.

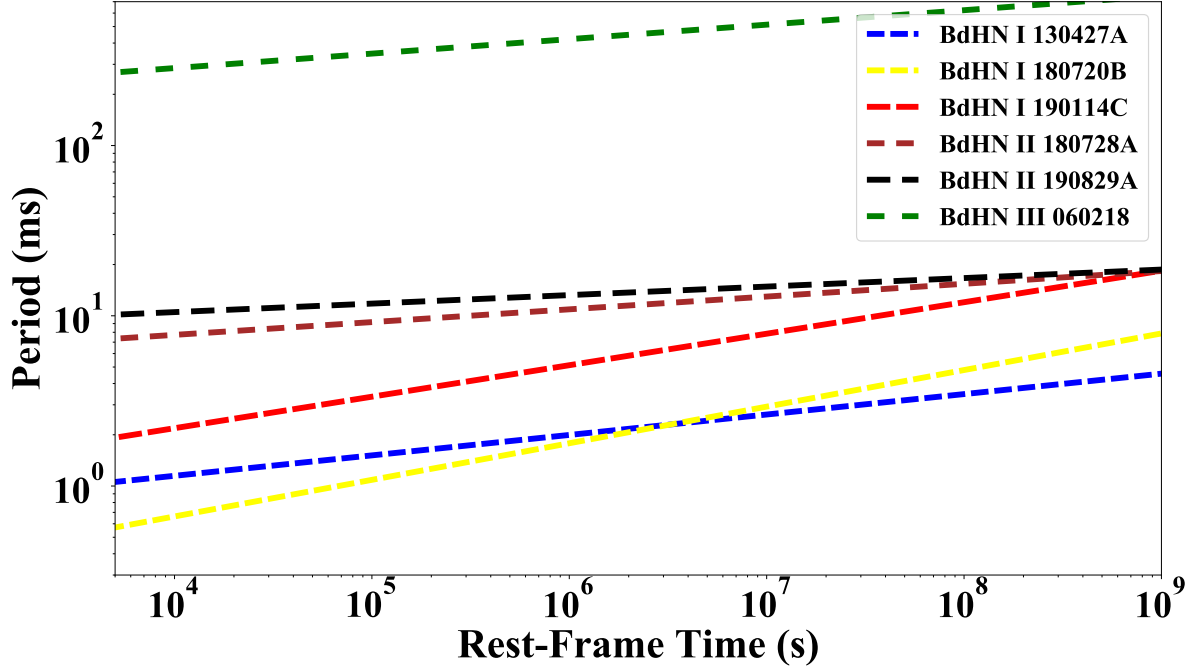


Figure 8. The evolution of the vNS period of six BdHNe, as a function of rest-frame time. The values of the vNS period at 10^4 s, namely in the pulsar dominated region of the afterglow are tabulated in Table 4. The trend of the vNS period indicates that the rotational energy is being released due to the radiation losses in the keV band revealing itself as the X-ray afterglow luminosity.

(ii) The X-ray afterglow is always present in *all* of the 378 BdHNe I; see Appendix A.

(iii) This result clearly indicates the spherical symmetry, or a very wide-angle emission of the X-ray afterglow.

4.1 The spin of the vNS

In Ruffini et al. (2018b); Rueda et al. (2020) and Wang et al. (2019), the bolometric luminosity contributing to the optical and X-ray bands by the vNS rotational energy loss by magnetic braking has been modeled for the emission at late times $t \gtrsim 10^4$ s of the “Nousek-Zhang” (flare-plateau-afterglow, FPA phase). This allows the inference of the initial rotation period of the vNS as well as its magnetic field structure. The origin of the long GRB afterglows at this phase is the interaction between the SN ejecta and the spinning magnetised vNS and their synchrotron emission (Ruffini et al. 2018b).

Since the vNS is just born, it must be rapidly rotating and contains abundant rotational energy:

$$E_{\text{rot}} = \frac{1}{2} I \Omega^2, \quad (4)$$

where I is the moment of inertia, and $\Omega = 2\pi/P_{\text{vNS}}$ is the angular velocity. For a vNS with a period of $P_{\text{vNS}}=1$ ms, $M = 1.4M_{\odot}$, $R = 10$ km, the moment of inertia is $I \sim 10^{45}$ g cm². This leads to a total rotational energy of $E \sim 2 \times 10^{52}$ erg.

We assume that the rotational energy of the vNS provides the energy budget of the X-ray radiation via synchrotron emission of the electrons (Ruffini et al. 2018b):

$$E_{\text{rot}} = E_X. \quad (5)$$

This is reminiscent of the extraction of the BH rotational energy via synchrotron radiation of electrons radiating in the GeV energy band (Ruffini et al. 2019c).

Therefore, using the Eq. (4) and substituting the Eq. (3)

$$\frac{dE_X}{dt} = L_X(t) = A_X \left(\frac{t}{1\text{s}} \right)^{-\alpha_X} = -I\Omega\dot{\Omega}. \quad (6)$$

The best fit to the X-ray luminosity of Eq. (3), together with Eq. (6), allow an estimate of the spin of the vNS in *all* BdHNe, as well as their spin evolution; see Table 4 and Fig. 8.

In Table 4, we report the physical quantities of three BdHNe I, GRB 130427A, GRB 180720B and GRB 190114C, together with two BdHNe II, GRB 180728A and GRB 190829A, as well as one BdHNe III, GRB 060218; assuming a vNS of mass and radius, respectively, $1.4M_{\odot}$ and 10^6 cm. The vNS emission is not able to explain the emission of the “Nousek-Zhang” phase at early times 10^2 – 10^4 s. As it is shown in Ruffini et al. (2018b,c), that emission is mainly powered by the mildly-relativistic SN kinetic energy which we refer it to as the *SN dominated region*. After 10^4 s, as shown by Ruffini et al. (2018b), the role of vNS becomes prominent, referred to as the *pulsar dominated region*.

The first main results of this paper are: 1) the first identification of the SN-rise, 2) the agreement of the extrapolated luminosity of the X-ray afterglow with the luminosity of the SN-rise, and 3) the measurement of the vNS period, leading to the power-law emission of the afterglow; see Fig. 7. The two process of the SN-rise energetics and the vNS dynamics appear to be strongly correlated.

[!ht]

Table 4. Observational properties of three BdHN I, GRB 130427A, GRB 180720B and GRB 190114C together with two BdHNe II 180728A and 190829A as well as one BdHN III, GRB 060218 and inferred physical quantities of the vNS of the corresponding BdHN model that fits the GRB data. Column 1: GRB name; column 2: identified BdHN type; column 3: cosmological redshift (z); column 4: the isotropic energy released (E_{iso}) in gamma-rays; column 5: vNS rotation period (P_{vNS}) at 10^4 s, column 6: The isotropic energy of the X-ray afterglow (E_X). In We assume the NS mass of $1.4M_{\odot}$ and the NS radius of 10^6 cm for all these cases.

GRB	Type	Redshift	E_{iso} (erg)	$P_{\text{vNS}}@10^4$ s (ms)	E_X (after 10^4 s) (erg)	A_X (erg/s)	α_X
130427A	BdHN I	0.34	9.2×10^{53}	1.15	1.67×10^{52}	$3.65 \pm 0.63 \times 10^{52}$	1.24 ± 0.02
180720B	BdHN I	0.654	6.8×10^{53}	0.66	4.99×10^{52}	$(112.67 \pm 93.89) \times 10^{52}$	1.43 ± 0.07
190114C	BdHN I	0.42	1.5×10^{53}	2.19	4.60×10^{51}	$(5.14 \pm 2.03) \times 10^{52}$	1.37 ± 0.05
180728A	BdHN II	0.117	2.3×10^{51}	7.74	3.68×10^{50}	$(2.19 \pm 0.13) \times 10^{50}$	1.15 ± 0.05
190829A	BdHN II	0.0785	2.2×10^{50}	10.31	2.07×10^{50}	$(5.20 \pm 0.89) \times 10^{49}$	1.10 ± 0.06
060218	BdHN III	0.033	5.4×10^{49}	285.81	2.69×10^{47}	$(2.19 \pm 0.53) \times 10^{47}$	1.17 ± 0.02

5 BDHN I: THE FERMI-LAT OBSERVATIONS

5.1 BdHNe I observed by Fermi-LAT

We now address the 378 BdHNe I with known redshifts; see [Pisani et al. \(2016\)](#); [Ruffini et al. \(2018a\)](#) and Appendix A: out of them, we are first interested in the 25 BdHNe I emitting GeV radiation and within the boresight angle of *Fermi*-LAT, i.e. $\theta < 75^\circ$, at the time of the trigger, since exposure drops quickly for larger angles ([Ajello et al. 2019](#)). They have as well a TS value > 25 , which means the GeV photons are excluded at the $5\text{-}\sigma$ level from background sources. We follow the first and second *Fermi* catalogs ([Ackermann et al. 2013](#); [Ajello et al. 2019](#)) for the time-resolved likelihood spectral analysis. Therefore, we divide the data into logarithmic spaced bins and, if the test statistic (TS) value of each bin is smaller than 16, we merge the time bin with the next one and repeat the likelihood analysis. In Table 5, we indicate in the first column the name of the BdHNe I, in the second their measured redshift, we report in the third column the $E_{\text{p},i}$ obtained from the *Fermi* data, we estimate in the fourth column the $E_{\gamma,\text{iso}}$, which is itself larger than the 10^{52} erg. In the fifth column, the *Fermi* GCN numbers are shown. In the sixth column, the values of E_{LAT} are provided and finally we add the boresight angle of the LAT $\theta < 75^\circ$ and the TS values of these GRBs observed by LAT.

5.2 BdHNe I without GeV emission and geometry of the BdHNe I

We now turn to an additional unexpected result obtained in the analysis of the BdHNe I subtended within the 75° of the *Fermi*-LAT boresight angle: the existence of 29 BdHNe I without observed GeV emission, see Table 6. Although the distribution of the boresight angle and redshift is analogous to the one of the 25 sources considered in section 5, no GeV emission is observed.

Some BdHNe I of this group have been observed previously by *Swift* and have been identified as sources of a) gamma and hard X-ray flares, b) soft X-ray flares and of c) the extended thermal emission (see [Ruffini et al. 2018a](#), for details). A particular example has been given by GRB 151027A in [Nappo et al. \(2017\)](#) and [Ruffini et al. \(2018c\)](#). There, we assumed that the viewing angle of these sources lies in the equatorial plane of the progenitor system; see section 1 and Fig. 4. As we will show in this article, in none of these sources GeV radiation can be observed due to the new morphology discovered in the BdHNe I; see next section.

6 MORPHOLOGY OF BDHN I

We here assume that the 25 sources considered in Table 5, all emitting in the GeV have a viewing angle close to the normal of the plane. This assumption is confirmed in [Ruffini et al. \(2019c\)](#) where indeed the high energy GeV-TeV radiations are emitted in direction close the BH rotation axis.

The remaining 29 sources in Table 6 have a viewing angle in the equatorial plane of the binary progenitor and in that case only flaring activities in gamma and X-ray are observable, i.e. no GeV-TeV emission, as explicitly shown in [Ruffini et al. \(2018c, 2019c\)](#). This allows us to introduce a new morphology for the BdHNe I and predict specific observational properties.

We now look at the ratio between the number of GRBs with an observed GeV radiation, N_{LAT} , and the total number of GRBs, N_{tot} , both within the LAT 75° boresight angle. We assume that: 1) BdHNe I follow the same cosmological isotropic distribution of all GRBs first observed by the BATSE instrument onboard the CGRO satellite (see, e.g., [Meegan et al. 1992](#); [Paciesas et al. 1999](#)); 2) all orientations of the BdHNe I with respect to the LAT detector are equally probable; 3) the GeV emitting region is a two-side cone whose opening angle is the same for all sources. Under these assumptions, we can then estimate the half-opening angle of a single cone ϑ as:

$$1 - \cos \vartheta = \frac{N_{\text{LAT}}}{N_{\text{tot}}}. \quad (7)$$

Our search in the LAT data¹ gives $N_{\text{LAT}} = 25$ and $N_{\text{tot}} = 54$, leading to $\vartheta \approx 60^\circ$. Therefore, in BdHN I the GeV emission comes from a wide-angle emission, as it is schematically shown in Fig. 9. This is in agreement with theory of synchrotron radiation produced around the Kerr BH along the rotation axis (see details in [Ruffini et al. 2019c](#)).

Therefore, we have identified a *new* morphology of the BdHN I (see Figs. 9 and 10). The identification of this morphology has been possible thanks to the analysis of the GeV emission in the present paper, by the soft and hard X-ray flares in [Ruffini et al. \(2018a\)](#), the extended thermal emission in [Nappo et al. \(2017\)](#); [Ruffini et al. \(2018a\)](#) in GRB 151027A. In this identification, we have been guided by the large number of numerical simulations describing the accretion of the SN ejected material around the NS companion; see Figs. 4 and 10, and its idealized representation in Fig. 9; (see [Becerra et al. 2016, 2019](#), for additional details).

What can be concluded from the above results is that in BdHNe I, the GeV emission is only detectable when the viewing angle is less

¹ https://fermi.gsfc.nasa.gov/ssc/observations/types/grbs/lat_grbs/table.php

GRB	z	$E_{p,i}$ (MeV)	$E_{\gamma,iso}$ (10^{52} erg)	Fermi GCN	E_{LAT} (10^{52} erg)	θ (deg)	TS
080916C	4.35	2.27 ± 0.13	407 ± 86	8246	230 ± 10	48.8	1450
090323A	3.57	2.9 ± 0.7	438 ± 53	9021	120 ± 20	57.2	150
090328A	0.736	1.13 ± 0.08	14.2 ± 1.4	9044	2.7 ± 0.4	64.6	107
090902B	1.822	2.19 ± 0.03	292.0 ± 29.2	9867	47 ± 2	50.8	1832
090926A	2.106	0.98 ± 0.01	228 ± 23	9934	149 ± 8	48.1	1983
091003A	0.897	0.92 ± 0.04	10.7 ± 1.8	9985	0.8 ± 0.3	12.3	108
091127	0.49	0.05 ± 0.01	0.81 ± 0.18	10204	0.03 ± 0.02	25.8	34
091208B	1.063	0.25 ± 0.04	2.10 ± 0.11	10266	$\gtrsim 0.41 \pm 0$	55.6	20
100414A	1.368	1.61 ± 0.07	55.0 ± 0.5	10594	7 ± 1	69	81
100728A	1.567	1.00 ± 0.45	72.5 ± 2.9	11006	0.9 ± 0.3	59.9	32
110731A	2.83	1.21 ± 0.04	49.5 ± 4.9	12221	15 ± 2	3.4	460
120624B	2.197	1.39 ± 0.35	347 ± 16	13377	22 ± 2	70.8	312
130427A	0.334	1.11 ± 0.01	92 ± 13	14473	8.6 ± 0.4	47.3	163
130518A	2.488	1.43 ± 0.38	193 ± 1	14675	15 ± 5	41.5	50
131108A	2.40	1.27 ± 0.05	51.20 ± 3.83	15464	37 ± 4	23.78	870
131231A	0.642	0.27 ± 0.01	21.50 ± 0.02	15640	1.6 ± 0.3	38	110
141028A	2.33	0.77 ± 0.05	76.2 ± 0.6	16969	9 ± 2	27.5	104.5
150314A	1.758	0.86 ± 0.01	70.10 ± 3.25	17576	1.8 ± 0.7	47.13	27.1
150403A	2.06	0.95 ± 0.04	87.30 ± 7.74	17667	1.1 ± 0.4	55.2	37
150514A	0.807	0.13 ± 0.01	1.14 ± 0.03	17816	0.06 ± 0.05	38.5	33.9
160509A	1.17	0.80 ± 0.02	84.5 ± 2.3	19403	10 ± 1	32	234
160625B	1.406	1.3 ± 0.1	337 ± 1	19581, 19604	17 ± 1	41.46	961.33
170214A	2.53	0.89 ± 0.04	392 ± 3	20675, 20686	53 ± 4	33.2	1571
170405A	3.51	1.20 ± 0.42	241.01 ± 52.02	20990, 20986	16 ± 7	52.0	56
180720B	0.654	1.06 ± 0.24	68.2 ± 2.2	22996, 23042	2.2 ± 0.2	49.1	975

Table 5. Prompt and GeV emission of the 25 long GRBs inside the Fermi-LAT boresight angle and with GeV photons detected. The columns list: the source name, z , $E_{p,i}$, $E_{\gamma,iso}$, E_{LAT} in 0.1–10 GeV, the position of the source from the LAT boresight θ , the likelihood TS. The E_{LAT} includes only the energy in the observed time duration, which does not cover the whole GeV emission period, and is different for each GRB, so we put a symbol ' \gtrsim ' to indicate that the value is the lower limit.

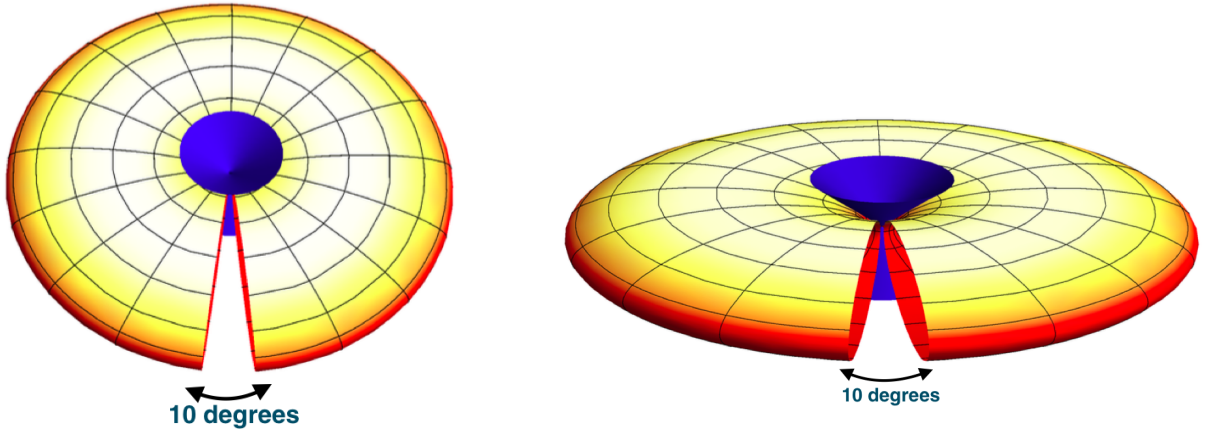


Figure 9. Schematic plot for showing the morphology of the BdHNe I. The GeV emission is detectable when the viewing angle is less than the 60° from the normal to the orbital plane. Left panel is the situation in which the detectors can observe GeV and Prompt emissions and the right panel is the one for which GeV emission is not detectable and only Gamma-ray and X-ray flares are detectable. The 10° cuts in both figures indicate the low density region in Fig 10 through which the prompt radiation phase can be “seen in the orbital plane”. The existence of such a 10° cut was first identified by the SPH simulation quoted in Becerra et al. (2016, 2019) and further confirmed in GRB 151027A (Ruffini et al. 2018c).

than $\approx 60^\circ$ from the normal to the plane and the BdHN I is “seen from the top”, see the left plot in Fig. 9. Whenever the viewing angle is within 60° from the orbital plane, no GeV emission is observed, though X-ray and gamma-ray flares are observed, see right plot in Fig. 9.

Therefore, the second main result of this paper is the identification of the BdHN I morphology and its explanation within the BdHN I model.

7 SPH SIMULATION OF BDHNE I

The numerical simulations at the moment of BH formation in a BdHN I is presented in Becerra et al. (2016, 2019). Three-dimensional (3D) views of the density distribution at the moment of the BH formation in a BdHN I are shown Fig. 10. These plots correspond to the simulation of the SN ejecta expansion in the presence of the NS companion. The simulation is performed using an SPH code in which the SN ejecta material is evolved with N point-

GRB	z	E_p (MeV)	$E_{\gamma, \text{iso}}$ ($\times 10^{52}$ erg)	Fermi GCN	θ (deg)	GeV observed	comments
081222	2.77	0.51 ± 0.03	27.4 ± 2.7	8715	50.0	no	
090424A	0.544	0.27 ± 0.04	4.07 ± 0.41	9230	71.0	no	
090516A	4.109	0.14 ± 0.03	99.6 ± 16.7	9415	20.0	no	Clear X-ray flare
100615A	1.398	0.21 ± 0.02	5.81 ± 0.11	10851	64.0	no	
100728B	2.106	0.32 ± 0.04	3.55 ± 0.36	11015	57.1	no	
110128A	2.339	0.46 ± 0.01	1.58 ± 0.21	11628	45.0	no	
111228A	0.716	0.060 ± 0.007	2.75 ± 0.28	12744	70.0	no	
120119A	1.728	0.52 ± 0.02	27.2 ± 3.6	12874	31.4	no	
120712A	4.175	0.64 ± 0.13	21.2 ± 2.1	13469	42.0	no	
120716A	2.486	0.4 ± 0.04	30.2 ± 3.0	13498	63.0	no	
120909A	3.93	0.87 ± 0.01	87 ± 10	13737	66.0	no	
130528A	1.250	0.27 ± 0.18	18.01 ± 2.28	14729	60.0	no	X-ray flare
130925A	0.347	0.14 ± 0.04	3.23 ± 0.37	15261	22.0	no	X-ray flare
131105A	1.686	0.55 ± 0.08	34.7 ± 1.2	15455	37.0	no	
140206A	2.73	1.1 ± 0.03	144.24 ± 19.20	15790	46.0	no	Clear X-ray flare
140213A	1.2076	0.176 ± 0.004	9.93 ± 0.15	15833	48.5	no	
140423A	3.26	0.53 ± 0.04	65.3 ± 3.3	16152	44.0	no	
140623A	1.92	1.02 ± 0.64	7.69 ± 0.68	16450	32.0	no	
140703A	4.13	0.91 ± 0.07	1.72 ± 0.09	16512	16.0	no	
140907A	1.21	0.25 ± 0.02	2.29 ± 0.08	16798	16.0	no	X-ray flare
141220A	1.3195	0.42 ± 0.02	2.44 ± 0.07	17205	47.0	no	
150301B	1.5169	0.45 ± 0.10	2.87 ± 0.42	17525	39.0	no	
150821A	0.755	0.57 ± 0.03	14.7 ± 1.1	18190	57.0	no	
151027A	0.81	0.62 ± 0.11	3.94 ± 1.33	18492	10.0	no	Clear X-ray flare
151111A	3.5	0.25 ± 0.04	3.43 ± 1.19	18582	50.0	no	X-ray flare observed
161014A	2.823	0.64 ± 0.06	10.1 ± 1.7	20051	69.0	no	
171222A	2.409	0.1 ± 0.01	20.73 ± 1.7	22272, 22277	43	no	
180703A	0.67	0.58 ± 0.05	3.15 ± 0.7	23889, 22896	44	no	
180728A	0.117	0.1 ± 0.02	3.15 ± 0.7	23055, 23067	35	no	

Table 6. List of 29 BdHNe I inside the Fermi-LAT boresight angle and with no GeV photons detected: 29 BdHNe I with redshift taken from (Ruffini et al. 2016b) from 2008, when Fermi started to operate, till the end of 2016. All of them are within the boresight of Fermi-LAT, but no detected GeV photons. For each source the columns list: z , $E_{\gamma, \text{iso}}$, E_p , GCN number, position of the source from LAT boresight θ , whether there was a detection by LAT, and additional information.

like particles, in the present case 16 million, with different masses and their motion is followed under the NS gravitational field. The orbital motion of the NS around the SN explosion center is also taken into account as the NS star gravitational mass changes via the hypercritical accretion process. The latter was modeled independently estimating the accretion rate onto the NS via the Bondi-Hoyle formalism. For the initial conditions of the simulation an homologous velocity distribution in free expansion was adopted and a power-law initial density profile of the SN matter was modeled by populating the inner layers with more particles (see Fryer et al. 2014; Becerra et al. 2016, 2019, for additional details). Figures 4 and 10 correspond to an initial binary system formed by a $2M_{\odot}$ NS and the CO_{core} obtained from a progenitor with $M_{\text{ZAMS}} = 30M_{\odot}$. When the CO_{core} collapses and explodes, it ejects $7.94M_{\odot}$ and leads a νNS of $1.5M_{\odot}$ at its center. The initial binary period is about 5 min, corresponding to a binary separation of $\approx 1.5 \times 10^{10}$ cm.

The new morphology of the BdHNe I presented here and in the previous section leads to a difference in the observed energy spectra and time variability for sources with viewing angle in the plane, or normal to the orbital plane of the binary progenitor. We infer that our 25 BdHNe I, with viewing angles less than $\approx 60^\circ$ from the normal to the orbital plane of the binary progenitor, “seen from the top”, have larger $E_{\gamma, \text{iso}}$ than the ones with a viewing angle lying in the plane of the binary system (see Tables 5 and 6). This explains the association/non-association of the GeV emission with bright GRBs often mentioned in the current literature (see Racusin et al. 2011; Cenko et al. 2011 and Fig. 4 in Nava 2018).

An additional issue in the traditional approach (see e.g. Beniamini et al. 2015; Racusin et al. 2011 and sections 3 and 4 in Nava 2018) is also solvable: the sources that are seen with a viewing angle lying in the orbital plane have stronger flaring activities in the X-ray afterglow when compared to the 25 emitting in the GeV range. Therefore, the ratio between E_{iso} and the luminosity in the X-ray afterglow is systematically smaller than in the 25 with GeV emission. This offers a different explanation than the one presented in the traditional approach. However, all of these matters that have already been mentioned in Ruffini et al. (2018c) need a new operational definition of $E_{\gamma, \text{iso}}$, taking into due account the hard and soft X-ray flares and the extended thermal emission; see also Ruffini et al. (2019b).

Another important specific feature of the new morphology of BdHN I is the presence of the νNS formed at the center of the exploding SN (see Fig. 4 and Becerra et al. 2019, 2016). We have shown that the νNS manifests itself through the synchrotron emission by relativistic electrons injected from it into the expanding magnetized SN ejecta, as well as through its pulsar emission which explain the early and late optical and X-ray afterglow, respectively, allowing the inference of the νNS rotation period (see Ruffini et al. 2018b). A smoking gun of this picture, namely the verification of the νNS activity following the above mechanism, both in XRFs (BdHNe II) and in BdHNe I, and the connection of the inferred rotation period of the νNS to the one of the CO-star and to the orbital period, from angular momentum conservation, has been explicitly shown in the GRB 180728A (BdHN II) and GRB 130427A (BdHN I) and GRB 190114C (BdHN I); see Wang et al. (2019) for details.

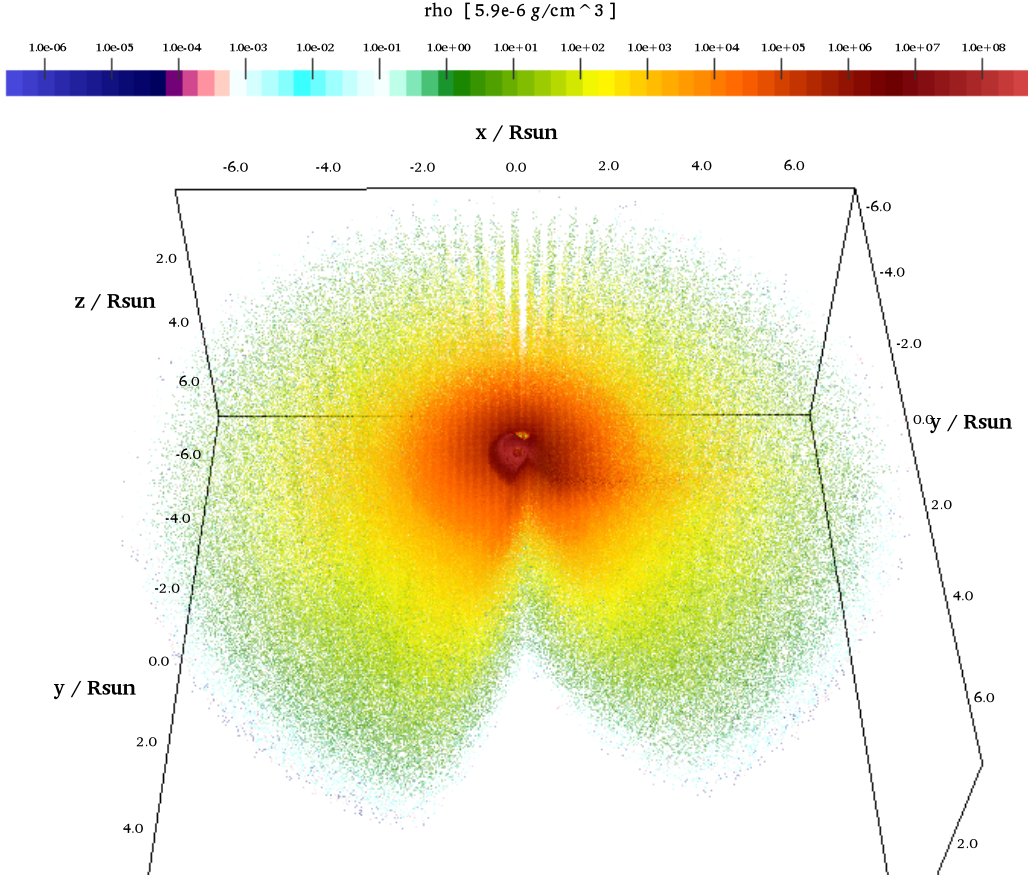


Figure 10. Three-dimensional, half hemisphere views of the density distribution of the SN ejecta at the moment of BH formation in a BdHN I. The simulation is performed with a SPH code that follows the SN ejecta expansion under the influence of the NS companion gravitational field including the effects of the orbital motion and the changes in the NS gravitational mass by the hypercritical accretion process. The initial conditions of the SN ejecta are set as a homologous velocity distribution in free expansion and the mass-distribution is modeled with 16 millions point-like particles (see [Becerra et al. 2016, 2019](#), for additional details). The binary parameters of this simulation are: the NS companion has an initial mass of $2.0 M_{\odot}$; the CO-star, obtained from a progenitor with zero-age main-sequence (ZAMS) mass $M_{\text{ZAMS}} = 30 M_{\odot}$, leads to a total ejecta mass of $7.94 M_{\odot}$ and to a $1.5 M_{\odot}$ vNS, the orbital period is $P \approx 5$ min (binary separation $a \approx 1.5 \times 10^{10}$ cm). The distribution of the ejecta is not axially symmetric; it is strongly influenced by the rotation of the system and accretion occurring in the binary component, see Fig. 4. Particularly relevant for the observations is the low density region of $\approx 10^{\circ}$ which allows, for the sources with viewing angle in the equatorial plane to detect the prompt radiation phase. This has been qualitatively indicated in Fig. 9. In these sources, only a fraction of approximately 10% of the prompt radiation can be detectable, they are the only ones able to trigger the *Fermi*-GBM and the remaining 90% will not have detectable prompt radiation, see [Ruffini et al. \(2018c\)](#). Figure is taken from [Ruffini et al. \(2018c\)](#) with the kind permission of the authors.

8 THE LUMINOSITY POWER-LAW BEHAVIOR IN BDHNE MEASURED IN THE REST-FRAME

In the following, we fit simultaneously the luminosity light-curves of all the 25 BdHNe with GeV emission expressed in their rest-frame. We assume the same power-law decay index for all of them, but allow different amplitude values. This assumption is consistent with our model, moreover, it is a benefit for those GRBs with limited data that cannot be fitted solely.

We limit our analysis of the light-curves after than the BdHN I prompt emission, when the GeV luminosity is already in the asymptotic power-law regime. We assume the power-law

$$L_n(t) = A_n t^{\alpha_{\text{GeV}}}, \quad (8)$$

describing the rest-frame 0.1–100 GeV isotropic luminosity light-curve of n th BdHN I. In the simultaneous fitting, we perform the Levenberg-Marquardt method to perform the minimization ([Gill & Wright 1981](#)). The basic idea of fitting is to minimize the χ^2 ; when fitting one curve to one equation, the χ^2 is minimized. To fit N

curves to N equations simultaneously, the sum of the χ^2 values should to be minimized. The related equations are:

$$\chi^2 = \sum_{n=1}^N \chi_n^2, \quad (9)$$

$$\chi_n^2 = \sum_{i=1}^M \frac{1}{\sigma_{ni}^2} (L_{ni} - L_n(t_{ni}, A_n, \alpha_{\text{GeV}}))^2, \quad (10)$$

where n represents each BdHN I, i represents each data point in a given BdHN I, A_n is the amplitude of a power-law function for the n th BdHN I, α_{GeV} is the common power-law index shared for all the BdHNe I. Thus, for the n th BdHN I, at time t_{ni} , the observed luminosity is L_{ni} , and the predicted luminosity is $L_n(t_{ni}, A_n, \alpha)$. The value of χ^2 represents the difference between the best power-laws fitting and all the observed data, it is a summation of individual χ_n^2 , which represents the difference between the power-law fitting and the observed value of each GRB.

Out of 25 BdHNe I presented in Table 5, we perform the fitting for only 20 GRBs which have more than two data points in

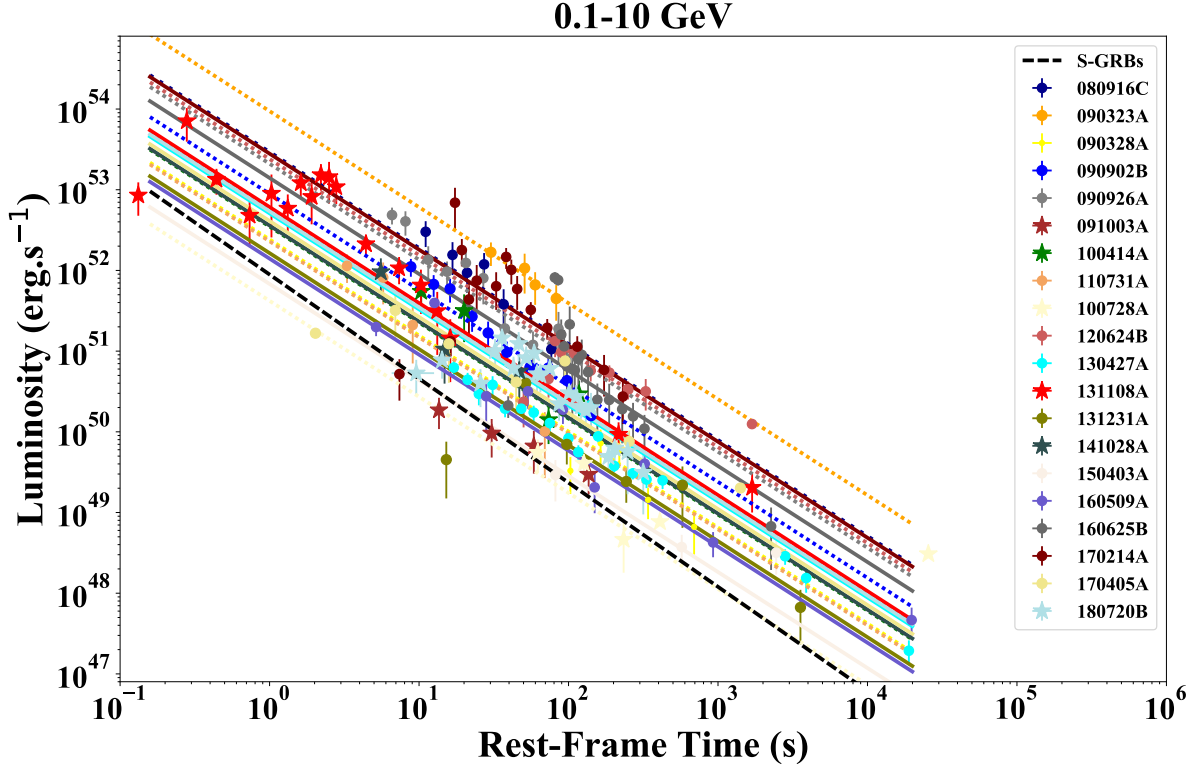


Figure 11. The rest-frame 0.1–10 GeV isotropic luminosity of 20 selected BdHNe with LAT emission. The solid red line marks the common power-law behavior of the GeV emission for BdHNe with slope $\alpha_{\text{GeV}} = 1.19 \pm 0.04$; the shaded gray area encloses all the luminosity light-curves of the selected BdHNe. The dashed black line marks the common power-law behavior of the GeV emission in S-GRBs with a slope of $\gamma = 1.29 \pm 0.06$.

BdHN	A_n (Amplitude)	uncertainty of A_n	$L_{10\text{s}}$	uncertainty of $L_{10\text{s}}$
080916C	2.9×10^{53}	$+9.1 \times 10^{52}$ -7.4×10^{52}	1.88×10^{52}	$+1.1 \times 10^{52}$ -1.0×10^{52}
090323A	9.4×10^{53}	$+3.5 \times 10^{53}$ -2.9×10^{53}	6.04×10^{52}	$+3.8 \times 10^{52}$ -1.4×10^{52}
090328A	2.4×10^{52}	$+1.1 \times 10^{52}$ -0.7×10^{52}	1.5×10^{51}	$+1.0 \times 10^{51}$ -0.9×10^{51}
090902B	8.9×10^{52}	$+2.5 \times 10^{52}$ -2.0×10^{52}	5.7×10^{51}	$+3.3 \times 10^{51}$ -3.0×10^{51}
090926A	2.1×10^{53}	$+3.9 \times 10^{52}$ -4.8×10^{52}	1.4×10^{52}	$+7.9 \times 10^{51}$ -7.3×10^{51}
091003A	5.7×10^{51}	$+1.7 \times 10^{51}$ -1.5×10^{51}	3.7×10^{50}	$+2.1 \times 10^{50}$ -2.0×10^{50}
100414A	3.5×10^{52}	$+1.4 \times 10^{52}$ -1.1×10^{52}	2.3×10^{51}	$+1.4 \times 10^{51}$ -1.3×10^{51}
100728A	4.2×10^{51}	$+1.9 \times 10^{51}$ -1.5×10^{51}	2.7×10^{50}	$+1.9 \times 10^{50}$ -1.6×10^{50}
110731A	2.3×10^{52}	$+0.8 \times 10^{52}$ -0.5×10^{52}	1.8×10^{51}	$+0.9 \times 10^{51}$ -0.8×10^{51}
120624B	2.4×10^{53}	$+8.2 \times 10^{52}$ -6.2×10^{52}	1.6×10^{52}	$+9.6 \times 10^{51}$ -8.5×10^{51}
130427A	5.1×10^{52}	$+2.1 \times 10^{51}$ -2.0×10^{51}	3.3×10^{51}	$+1.3 \times 10^{51}$ -1.3×10^{51}
131108A	6.1×10^{52}	$+9.1 \times 10^{51}$ -8.9×10^{51}	3.9×10^{51}	$+2.0 \times 10^{51}$ -1.9×10^{51}
131231A	1.64×10^{52}	$+7.9 \times 10^{51}$ -5.4×10^{51}	1.1×10^{51}	$+7.3 \times 10^{50}$ -6.1×10^{50}
141028A	3.6×10^{52}	$+1.2 \times 10^{52}$ -1.1×10^{52}	2.3×10^{51}	$+1.4 \times 10^{51}$ -1.3×10^{51}
150403A	6.8×10^{51}	$+3.0 \times 10^{51}$ -2.3×10^{51}	4.3×10^{50}	$+2.9 \times 10^{50}$ -3.0×10^{50}
160509A	1.4×10^{52}	$+4.9 \times 10^{51}$ -3.8×10^{51}	8.9×10^{50}	$+5.4 \times 10^{50}$ -4.1×10^{50}
160625B	1.4×10^{53}	$+4.6 \times 10^{52}$ -3.4×10^{52}	8.7×10^{51}	$+5.2 \times 10^{51}$ -4.6×10^{51}
170214A	2.8×10^{53}	$+7.4 \times 10^{52}$ -5.9×10^{52}	1.8×10^{52}	$+1.0 \times 10^{52}$ -0.9×10^{52}
170405A	4.1×10^{52}	$+1.1 \times 10^{52}$ -1.0×10^{52}	2.5×10^{51}	$+1.5 \times 10^{51}$ -1.4×10^{51}
180720B	5.4×10^{52}	$+6.6 \times 10^{51}$ -6.1×10^{51}	3.5×10^{51}	$+2.2 \times 10^{50}$ -2.1×10^{50}

Table 7. Fitting parameters of the 0.1–10 GeV power-law luminosity when measured in the rest-frame of 20 BdHNe with GeV emission: amplitude of the 0.1–10 GeV luminosity, A_n , and its uncertainty, the inferred 0.1–10 GeV luminosity at 10 s from the fitting and its uncertainty. The common power-law index is $\alpha_{\text{GeV}} = 1.19 \pm 0.04$. Out of 25 BdHNe emitting GeV emission, we performed the fitting for 20 GRBs which have more than two data points in their luminosity light-curves. GRBs 091127, 091208B, 130518A, 150314A, 150514A have only two data points in their GeV luminosity light-curves.

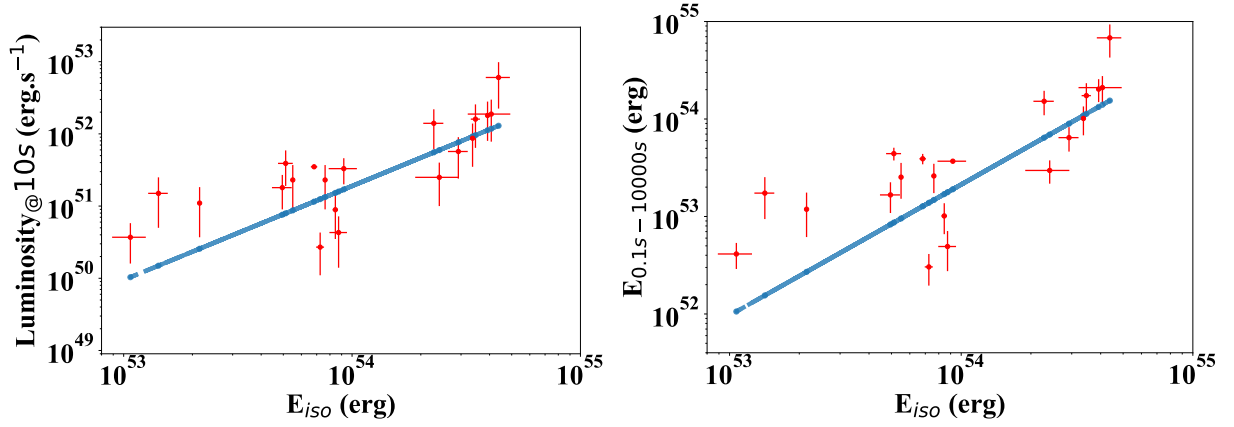


Figure 12. Left: the *Fermi*-LAT luminosity at 10 s in the energy range 0.1–10 GeV versus the isotropic gamma-ray energy from 1 keV to 10 MeV. The BdHNe are listed in Table 7. Right: the *Fermi*-LAT energy from 0.1 to 10^4 s versus isotropic gamma-ray energy from 1 keV to 10 MeV. See the corresponding values in Table 8.

BdHN	$E_{0.1-10^4\text{s}}$	uncertainty of $E_{0.1-10^4\text{s}}$
080916C	2.1×10^{54}	6.6×10^{53}
090323A	6.8×10^{54}	2.5×10^{54}
090328A	1.73×10^{53}	7.9×10^{52}
090902B	6.4×10^{53}	1.8×10^{53}
090926A	1.54×10^{54}	5.60×10^{53}
091003A	4.12×10^{52}	1.58×10^{52}
100414A	2.53×10^{53}	1.18×10^{53}
100728A	3.0×10^{52}	1.6×10^{52}
110731A	1.6×10^{53}	5.8×10^{52}
120624B	1.7×10^{54}	7.2×10^{53}
130427A	3.6×10^{53}	1.8×10^{52}
131108A	4.4×10^{53}	1.2×10^{53}
131231A	1.2×10^{53}	6.3×10^{52}
141028A	2.6×10^{53}	1.1×10^{53}
150403A	4.9×10^{52}	1.7×10^{52}
160509A	1.1×10^{53}	3.5×10^{52}
160625B	1.1×10^{54}	3.3×10^{53}
170214A	2.1×10^{54}	5.3×10^{53}
170405A	3.0×10^{53}	7.9×10^{52}
180720B	3.8×10^{53}	4.7×10^{52}

Table 8. Results of $E_{0.1-10^4\text{s}}$ and related error of 20 BdHNe. $E_{0.1-10^4\text{s}}$ is the total GeV energy (in erg) emitted from 0.1 to 10^4 s. GRBs 091127, 091208B, 130518A, 150314A, 150514A are excluded since they have only two data points in their GeV luminosity light-curves.

their luminosity light-curves. Therefore, for the fitting of BdHNe I, there are 20 bursts and each one has its power-law function. Consequently, there are in total 17 parameters, including 20 amplitudes, and 1 power-law index. The fitting gives a power-law index of $\alpha_{\text{GeV}} = 1.19 \pm 0.04$, i.e.:

$$L_n = A_n t^{-1.19 \pm 0.04}, \quad (11)$$

which is plotted in Fig. 11 and the amplitudes of each GRB, A_n , with the uncertainty are shown in Table 7. This inferred power-law index is similar to the one obtained from fitting the GeV flux, $f_V(t)$, see e.g. (Kumar & Barniol Duran 2009) and (Panaitescu 2017), in which the power-law index is $\alpha_{\text{GeV}} = 1.2 \pm 0.2$ and $\alpha_{\text{GeV}} = 1.2 \pm 0.4$, respectively.

In our approach, we adopt an alternative interpretation of these power-laws: instead of using the flux expressed in arrival time, we use the luminosity expressed in the rest-frame of the source. Since the luminosity is proportional to the flux, i.e. $L = 4\pi d_L^2(1+z)^{\alpha_{\text{GeV}}-2} f_V$, where d_L is the luminosity distance, this similarity of the power-law index is not surprising. The advantage of using lumi-

nosity expressed in the rest-frame of the source, instead of flux in arrival time, is that one can determine the intrinsic energy loss of the system which produces the GeV radiation, regardless of differences in the redshift of the sources. This allows us following our recent understanding of the BdHN I 130427A (see Ruffini et al. 2019c, and references therein), to relate the GeV radiation to the slowing down of the BH spin; see section 10.

After obtaining the best power-law parameters for the luminosity light-curve for each BdHNe I, we check the correlation between the GeV luminosity at 10 s from Eq. (11) using the fitted parameters and the isotropic energy $E_{\gamma,\text{iso}}$. The power-law fitting gives (see Fig. 12):

$$L_{10\text{s}} = (4.7 \pm 1.2) \times 10^{48} (E_{\text{iso}}/10^{52})^{1.3 \pm 0.3}, \quad (12)$$

and the fitting parameters for each GRB including their uncertainties are shown in Table 7. Furthermore, we estimate the energy released

in the GeV band by each GRB in the $0.1\text{--}10^4$ s time interval, i.e.:

$$E_{0.1-10^4\text{s}} = A_{\text{GRB}} \int_{0.1}^{10000} t^{-1.19} dt, \quad (13)$$

and the derived $E_{0.1-10^4\text{s}}$ are shown in Table 8. The parameters $E_{0.1-10^4\text{s}}$ and $E_{\gamma,\text{iso}}$ (isotropic energy of the prompt emission in γ band) are also correlated by a power-law relation (see Fig. 12):

$$E_{0.1-10^4\text{s}} = (4.4 \pm 1.5) \times 10^{50} (E_{\text{iso}}/10^{52})^{1.4 \pm 0.3}. \quad (14)$$

This positive correlation indicates that the BdHNe I with higher isotropic energy are also more luminous and more energetic in the GeV emission.

9 THE DETERMINATION OF THE MASS AND SPIN OF THE BH IN BDHNE I

The theoretical progress introduced in Ruffini et al. (2019c) has identified the GeV radiation as originating in the *inner engine* of BdHN I. There, for the first time, it has been shown that indeed the rotational energy of a Kerr BH can be extracted for powering an astrophysical system. The *inner engine* is composed of: a) a non-stationary Kerr BH, b) a uniform magnetic field of $\sim 10^{10}$ G aligned with the rotation axis, and c) the presence of a very tenuous fully ionized electron-nuclei plasma. The fundamental new conceptual breakthrough introduced by the physics of the *inner engine* are developed in parallel papers; see e.g. Rueda & Ruffini (2020). The main goal here is to show, using our recently published results, that the rotational energy of the Kerr BH is indeed sufficient to explain the energetics of the GeV emission. In turn, this allows us to determine here the mass and spin of the Kerr BH in each BdHN I.

We here apply the self-consistent solution already well tested in the case of GRB 130427A (Ruffini et al. 2019c) and GRB 190114C (Moradi et al. 2019) for determining the three parameters of the *inner engine*, namely the mass and spin of the BH as well as the strength of the surrounding magnetic field B_0 . The values are obtained satisfying three conditions:

(i) The energy budget for the observed GeV luminosity is provided by the extractable rotational energy of a Kerr BH; see Eq. (1a); see Eq. (34) in Ruffini et al. (2019c).

(ii) The magnetic field B_0 fulfills the transparency condition for the propagation of the GeV radiation imposed by the e^+e^- pair production process in the *inner engine*; see Eq. (35) in Ruffini et al. (2019c).

(iii) The ‘‘quantized’’ emission of the GeV radiation is determined by the density of the plasma and by the synchrotron radiation timescale (Ruffini et al. 2019c); see Eq. (36) in Ruffini et al. (2019c).

The high-quality GeV data in 11 BdHNe I out of the 25 long GRBs in Table 5 allow us to determine the starting point of the decreasing luminosity, by identifying the transition of the power-law dependence of the GeV luminosity from a positive to a negative slope (see Ruffini et al. 2019c, for more information). This enables us to calculate the lower limit of the mass, M , spin parameter of the BH, α , the corresponding irreducible mass of the BH, M_{irr} ; which remains constant during the energy extraction process, and finally the surrounding magnetic field strength, B_0 ; as reported in Table 9. The values of the masses $M > 2.21 M_{\odot}$ and spin parameters of $\alpha < 0.71$ of the BH for BdHNe I presented in Table 9 show the consistency with the upper limit of the critical mass of the NS in Rhoades & Ruffini (1974) and the mass and spin of rotating NSs computed in Cipolletta et al. (2015); see Fig. 13.

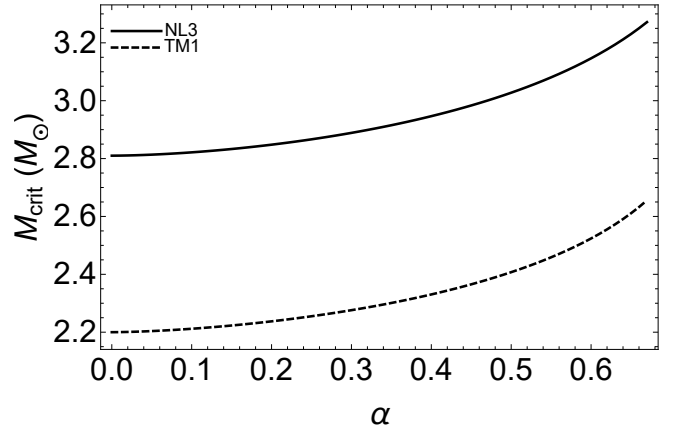


Figure 13. NS critical mass as a function of the spin parameter α for the NL3 and TM1 EOS. We recall that the maximum spin parameter of a uniformly rotating NS is $\alpha_{\text{max}} \approx 0.71$, independently of the NS EOS; see e.g. Cipolletta et al. (2015).

This has indeed been addressed in recent works (Ruffini et al. 2019c), where we have developed a complementary theory and its related analysis to identify the physical conditions which have to be enforced in order to extract the rotational energy of a Kerr BH. We have there addressed an approach of considering a Kerr BH placed in a uniform magnetic field of 10^{10} G aligned along the BH symmetry axis, fulfilling the Einstein-Maxwell equations via the Papapetrou-Wald solution (Wald 1974; Papapetrou 1966) modeling the *inner engine* which produces the MeV, GeV, TeV radiation and UHECRs as well (Rueda & Ruffini 2020).

10 SPIN DOWN OF THE BH IN BDHNE I

Following our previous work (Ruffini et al. 2019c), we can turn now from the luminosity expressed in the rest-frame of the sources, see Eq. (11), and from the initial values of the spin and mass of the BH expressed in Section 9, to derive the slowing down of the BH due to the energy loss in the GeV emission.

The relation of the luminosity and the extractable rotational energy is (see Eq. (39) in Ruffini et al. 2019c)

$$L = -\frac{dE_{\text{extr}}}{dt} = -\frac{dM}{dt}, \quad (15)$$

For each BH during the GeV emission process the M_{irr} is constant. Utilizing the best fit obtained for the GeV luminosity $L_{\text{GeV}} = A_{\text{GeV}} t^{-1.2}$ erg/s, we obtain a relation for the loss of mass-energy of the BH by integrating Eq. (15):

$$M = M_0 + 5At^{-0.2} - 5At_0^{-0.2}, \quad (16)$$

where M_0 is the initial mass of the newborn BH tabulated in Table 9. From the mass-energy formula of the BH we have (Ruffini et al. 2019c)

$$a = \frac{J}{M} = 2M_{\text{irr}} \sqrt{1 - \frac{M_{\text{irr}}^2}{(M_0 + 5At^{-0.2} - 5At_0^{-0.2})^2}}. \quad (17)$$

where M_0 is the initial mass of the BH presented in Table 9 as M_{α} at time t_0 at which the decaying part of GeV luminosity begins.

As indicative examples, we show in Fig. 14 the decrease of the BH spin, $\alpha = a/M = J/M^2$, as a function of time in GRBs 090902B, 131108A and 170405A.

Source	α	$M(\alpha)$ (M_{\odot})	M_{irr} (M_{\odot})	B_0 10^{10} G
BdHN I 080916C	0.87	8.9	7.6	1.9
BdHN I 090902B	0.59	5.3	5	2.8
BdHN I 090926A	0.76	8.4	7.7	2.1
BdHN I 110713A	0.37	4.7	4.6	4.5
BdHN I 130427A	0.40	2.3	2.24	4.1
BdHN I 130518A	0.50	2.5	2.4	3.3
BdHN I 131108A	0.56	4.7	4.4	2.9
BdHN I 160509A	0.41	2.4	2.3	4
BdHN I 170214A	0.80	2.8	2.5	2.1
BdHN I 170405A	0.45	3.4	3.3	3.7
BdHN I 180720B	0.27	2.3	2.29	6

Table 9. The mass, M , the spin parameter, $\alpha = J/M^2$, and surrounding magnetic field, B_0 in 11 BdHNe I, out of the 25 long GRBs in Table 5. The high-quality GeV data of this sample allows for a measurement of the lower limit of their “inner engine” parameters; see Eq. (1a).

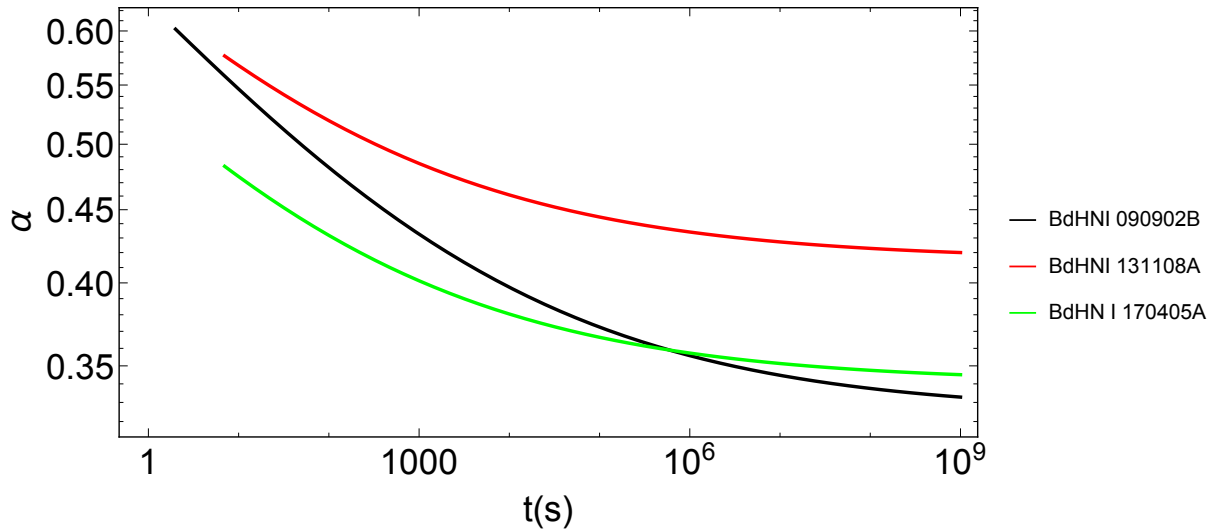


Figure 14. The BH spin, as a function of rest-frame time. The initial values of the spin and mass of the BH for GRB 090902B are $\alpha = 0.59$ and $M(\alpha) = 5.3M_{\odot}$, for 131108A: $\alpha = 0.56$ and $M(\alpha) = 4.7M_{\odot}$ and for 170405A: $\alpha = 0.45$ and $M(\alpha) = 3.4M_{\odot}$. This behavior of the spin parameter indicates that the rotational energy of the BH is decreasing due to the radiation losses in the GeV energy band.

The third main results of this paper are: the identification of the rotational energy extraction from a Kerr BH and the consequent measure of the BH mass and spin.

11 CONCLUSIONS

The unprecedented observations of GRBs, pioneered by the BeppoSax satellite, have developed into the largest ever observational multi-wavelength effort in astrophysics: starting with the *Swift*, BAT and XRT instruments in the X-ray band; see Fig. 1, progressing with the *AGILE* and with *Fermi*-GBM in the MeV-GeV bands. These have worked in synergy with hundreds of optical, radio and VHE telescopes worldwide including MAGIC (see Fig. 3) and H.E.S.S. (see Fig. 2).

This unprecedented observational effort assisted by parallel theoretical developments has allowed in this article the achievement of a new understanding of three new basic properties of the BdHNe: the first appearance of the SN triggering the entire BdHN process, the SN-rise; the presence of a mildly-relativistic afterglow in the X-ray in *all* BdHN; the identification in *all* BdHN of the origin of the high-energy emission in an *inner engine* driven by a newborn BH;

the description of their morphology. We show, for the first time, the extractable energy of a Kerr BH as an astrophysical energy source, which has allowed the inference of the BH mass and spin.

In section 2, we first recall that binary systems have an important role in understanding both short and long GRBs and we report the progress in the classification of GRBs in nine different subclasses (see e.g. Wang et al. 2019, and references therein). We then focus on the BdHNe: long GRB model with progenitors composed of CO_{core} and the binary NS companion. The CO_{core} undergoes gravitational collapses that gives origin to a SN and the collapse of its Fe-core produces a vNS.

We also there recall the fundamental role of the hypercritical accretion of the SN into the companion binary NS and into the vNS determine the BdHNe further evolution; see Fig. 4 and Pisani et al. (2016); Ruffini et al. (2016b, 2018c); Wang et al. (2019) for further details. The SN accretion onto the vNS gives origin to the X-ray afterglow emission, while the SN accretion onto the companion NS leads to different outcomes as a function of the binary period. For periods shorter than 5 min, the hypercritical accretion onto the companion NS is sufficient for the NS to overcome its critical mass and gravitationally collapse to a BH. The BH formation characterizes a BdHN I with an isotropic energy in the range of

$10^{52} \lesssim E_{\text{is}} \lesssim 10^{54}$ erg. We here show that it gives origin, *only in some* of them, to the GeV emission observed by Fermi-LAT. For larger binary periods, no BH is formed and consequently no GeV radiation is observed, the hypercritical SN accretion leads to a MNS with an isotropic energy in the range of $10^{50} \lesssim E_{\text{is}} \lesssim 10^{52}$ erg. We refer to these binaries as BdHN II paradigm. The same occurs for more detached binary systems leading to a BdHN III, where the isotropic energy is in the range of $10^{48} \lesssim E_{\text{iso}} \lesssim 10^{50}$ erg.

In section 3, we have given the spectral properties of the first appearance of the SN-rise in BdHN I and in BdHN II and also differentiate their energetics.

In section 4, we have related the SN-rise luminosity to the X-ray luminosity of the afterglow in all three BdHNe types. It is a fortunate coincidence that we have recently understood the origin of the afterglow as a consequence of the SN hypercritical accretion on the vNS. This process is dominated by a mildly-relativistic synchrotron pulsar-like emission with Lorentz factor $\Gamma \sim 2$ that gives rise to the X-ray afterglow (Ruffini et al. 2018b; Wang et al. 2019; Rueda et al. 2020), and we have also related their X-ray luminosity to the NS spin. This has allowed us to represent in Fig. 8 the afterglows for two BdHNe I, for two BdHNe II as well as one BdHN III and estimate in Table 4 the initial spin value of the vNS. What is the most remarkable, is that the X-ray afterglow is present in *all* BdHN types which implies that, unlike the GeV emission, which as we show in this article to be necessarily beamed, the X-ray afterglow emission is necessarily isotropic. What is equally relevant is that independently of the differences among these four subclasses of BdHN, the X-ray afterglow luminosity emission is consistent with a power-law index of -1.48 ± 0.32 as measured from the Swift observations (Pisani et al. 2016), and a common energy source well explained by the rotational energy of the vNS.

The first identification of the SN-rise and of the measurement of the vNS mass originating power-law emission of the afterglow are the first main result of this paper.

The first main results of this paper are:

- (i) the first identification of the SN-rise;
- (ii) the agreement of the extrapolated luminosity of the X-ray afterglow with the luminosity of the SN-rise;
- (iii) the measurement of the vNS period, originating the power-law emission of the afterglow; see Figs. 7 and 8.

The two process of the SN-rise energetics and the vNS dynamics appear to be strongly correlated.

We then turn in section 5 to consider only the case of BdHN I and their Fermi-GBM and LAT observations. In Appendix A, we update our previous classification of BdHN I following Pisani et al. (2016); Ruffini et al. (2016b, 2018c) reaching the total number of 378 BdHN I, *all* of them are characterized by:

- (i) a measured cosmological redshift;
- (ii) a prompt emission of $T_{90} > 2s$, measured by Fermi-GBM, with isotropic energy larger than 10^{52} erg;
- (iii) a decaying X-ray afterglow, measured by Swift-XRT, characterized by a luminosity decreasing with a mean power-law with index of $\alpha_X = -1.48 \pm 0.32$.

Contrary to the case of the X-ray afterglow, universally present in *all* BdHN types, the GeV radiation is present *only in some* BdHN I. No GeV emission occurs in BdHN II and BdHN III. We first explore the possibility that the non-detection of GeV radiation in *some* of BdHNe I could be due to the observational limitation of the LAT field of view, i.e. because of the boresight angle smaller than 75° . Indeed, we find that only $N_{\text{tot}} = 54$ out of the 378 BdHNe I are inside

the boresight angle of Fermi-LAT. What is unexpected is that only $N_{\text{LAT}} = 25$ out of these 54 BdHNe I exhibit the GeV emission observed by Fermi-LAT. For each of these 25 sources, we have given the basic parameters in Table 5. The corresponding data of the remaining 29 BdHN I, without observed GeV radiation, are given in Table 6.

In section 6, we have assumed that *all* BdHNe I, like all GRBs are homogeneously distributed in space (see, e.g., Meegan et al. 1992; Paciesas et al. 1999), we have inferred that the emission of the GeV radiation occurs in two opposite cones each of half opening angle of $\sim 60^\circ$ from the normal to the binary plane.

We duly recall as well that the visualization of the morphology has been made possible thanks to a close collaboration with LANL (see Becerra et al. 2016, 2019, for additional details), leading to the results well illustrated in the simulation presented in Figs. 4 and 10. We then conclude from this simulation that all of the 25 LAT sources are actually “seen from the top” which allows us to fully observe the conical emission of 60° half-opening angle. For the remaining 29 BdHN I without an observed GeV emission, we evidence that when the Swift data are available, gamma-ray flares and hard and soft X-ray flares as well as extended thermal emissions are observed in these systems (Ruffini et al. 2018c,a), and that these sources have a viewing angle laying in the “orbital plane” of the binary progenitor system.

We conclude that we are faced with a new morphology of the BdHN I which depends significantly on the viewing angle, “seen from the top”, normal to the binary orbital plane when the GeV emission is observed, or seen “in the plane” of the binary when the observation of the GeV radiation is impeded by the accreting binary material; see Figs. 4, 9 and 10. This is reminiscent of the morphology encountered in some AGNs; see e.g. the AGN IC 310 in Aleksić et al. (2014).

The second main result of this paper is the identification of the BdHN I morphology and its explanation within the BdHN I model.

We then recall some theoretical progresses in understanding the origin of the GeV emission:

a) The identification of the three components of the GRB *inner engine* in GRB 130427A (Ruffini et al. 2019c), composed of a Kerr BH with a magnetic field B_0 aligned with the BH rotation axis, both embedded in a tenuous ionized plasma composed of electrons and ions, has represented a turning point in the study of BdHN I. The electrodynamics of this *inner engine*, based on the Papapetrou-Wald solution (Wald 1974; Papapetrou 1966; Ruffini et al. 2019c), leads to a high energy emission in two opposite lobes in the MeV, GeV, and TeV radiation as well as narrowly beamed UHECR along the BH polar axis (Moradi et al. 2019);

b) This high-energy emission, unlike the traditional models which implies ultrarelativistic baryonic motion with $\Gamma \sim 10^3$ at 10^{16} cm– 10^{18} cm, occurs very close to the BH horizon;

c) The energy source is the extractable energy of the BH (Christodoulou 1970; Christodoulou & Ruffini 1971; Hawking 1971; Hawking 1972), see Eq. (1a), and is emitted in a sequence of impulsive process, the “*blackholic quanta*”, occurring on a timescale of 10^{-14} s (Rueda & Ruffini 2020).

On the basis of these results, we have examined the physical origin of the GeV emission observed by Fermi-LAT both in BdHN I. We find that the luminosity of the GeV emission as a function of time in the rest-frame of the source fulfills a universal decaying power-law dependence with index of -1.19 ± 0.04 ; see Fig 11. This has allowed: 1) to verify that indeed the entire GeV radiation observed by Fermi-LAT can be energetically expressed in terms of the rotational energy of the Kerr BH; 2) following the procedures in Ruffini

et al. (2019c) to evaluate the mass and spin of the BH; see Table 9; and 3) to explicitly compute the slowing down rate of the BH spin due to the GeV emission; see Fig. 14.

It has been possible for some of the 25 sources, with the best data:

a) to compute the lower limit of the initial value of the BH masses, M , and show their consistency with the absolute upper limit of the NS critical mass (Rhoades & Ruffini 1974), and the upper limit of the NS mass of $M = 2.21M_{\odot}$ and spin parameter of $\alpha < 0.71$ computed in Cipolletta et al. (2015);

b) to evaluate the value of the spin, a , and show the consistency with the canonical upper limit $\alpha = a/M \leq 1$;

c) by combining the value of the spin of the vNS observed from the afterglow (see Table 4), the time intervening between the SN-rise and the UPE phase, the mass estimate of the BH in GRB 190114C and in GRB 090926A and in GRB 180720B, we infer that necessarily in these system we are observing the presence of a BdHN precursor with a companion NS grazing the surface of the CO_{core} .

The third main results of this paper are:

- (i) the identification of the rotational energy extraction from a Kerr BH and,
- (ii) the consequent measure of the BH mass and spin.

All the above three main results are important: the underlying proof that indeed we can use the extractable rotational energy of a Kerr BH for explaining the high-energy jetted emissions of GRBs and AGNs stands alone. Even more subtle is the fact that the jetted emission does not originate from massive ultra-relativistic jetted emissions, but from very special energy-saving ultra-relativistic quantum and classical electro-dynamical processes originating in the high-energy jetted emission. This brings up the issue of *blackholical* energy (Rueda & Ruffini 2020), which is not treated here. We were waiting for this result for 49 years, since writing Eq. (1a).

ACKNOWLEDGEMENTS

We acknowledge the protracted discussion with Roy Kerr. We are thankful to the referee for the interesting report and suggestions. We also acknowledge the continuous support of the MAECI and the Italian Space Agency (ASI). Y. A. is supported by the Erasmus Mundus Joint Doctorate Program Grant N. 2014-0707 from EACEA of the European Commission. Y. A. acknowledges funding by the Science Committee of the Ministry of Education and Science of the Republic of Kazakhstan (Grant No. AP08855631) and also partial support from targeted financial program No. BR05336383 by Aerospace Committee of the Ministry of Digital Development, Innovations and Aerospace Industry of the Republic of Kazakhstan. G. J. M is supported by the U.S. Department of Energy under Nuclear Theory Grant DE-FG02-95-ER40934. This work made use of data from *Fermi* space observatory. This research has made use of data and software provided by the High Energy Astrophysics Science Archive Research Center (HEASARC), which is a service of the Astrophysics Science Division at NASA/GSFC and the High Energy Astrophysics Division of the Smithsonian Astrophysical Observatory.

DATA AVAILABILITY

The data underlying this article are available in the appendix A of the article.

REFERENCES

- A. Melandri et al., 2019, GRB Coordinates Network
- Abdalla H., et al., 2019, *Nature*, **575**, 464
- Ackermann M., et al., 2013, *ApJS*, **209**, 11
- Aharonian F., et al., 2006, *A&A*, **457**, 899
- Aimurатов Y., et al., 2017, *ApJ*, **844**, 83
- Ajello M., et al., 2019, *ApJ*, **878**, 52
- Aleksić J., et al., 2014, *Science*, **346**, 1080
- Aleksić J., et al., 2016a, *Astroparticle Physics*, **72**, 61
- Aleksić J., et al., 2016b, *Astroparticle Physics*, **72**, 76
- Amati L., et al., 2000, *Science*, **290**, 953
- Atwood W. B., et al., 2009, *ApJ*, **697**, 1071
- Barraud C., et al., 2003, *A&A*, **400**, 1021
- Barthelmy S. D., et al., 2005, *Space Sci. Rev.*, **120**, 143
- Becerra L., Cipolletta F., Fryer C. L., Rueda J. A., Ruffini R., 2015, *ApJ*, **812**, 100
- Becerra L., Bianco C. L., Fryer C. L., Rueda J. A., Ruffini R., 2016, *ApJ*, **833**, 107
- Becerra L., Ellinger C. L., Fryer C. L., Rueda J. A., Ruffini R., 2019, *ApJ*, **871**, 14
- Beniamini P., Nava L., Duran R. B., Piran T., 2015, *MNRAS*, **454**, 1073
- Berger E., 2014, *ARA&A*, **52**, 43
- Blandford R. D., McKee C. F., 1976, *Physics of Fluids*, **19**, 1130
- Burrows D. N., et al., 2005, *Space Sci. Rev.*, **120**, 165
- Campana S., et al., 2006, *Nature*, **442**, 1008
- Cano Z., Wang S.-Q., Dai Z.-G., Wu X.-F., 2017, *Advances in Astronomy*, **2017**, 8929054
- Cenko S. B., et al., 2006, *ApJ*, **652**, 490
- Cenko S. B., et al., 2011, *ApJ*, **732**, 29
- Chand V., et al., 2020, arXiv e-prints, p. arXiv:2001.00648
- Christodoulou D., 1970, *Physical Review Letters*, **25**, 1596
- Christodoulou D., Ruffini R., 1971, *Phys. Rev. D*, **4**, 3552
- Cipolletta F., Cherubini C., Filippi S., Rueda J. A., Ruffini R., 2015, *Phys. Rev. D*, **92**, 023007
- Costa E., et al., 1997, *Nature*, **387**, 783
- Damour T., Ruffini R., 1975, *Physical Review Letters*, **35**, 463
- Della Valle M., 2011, *International Journal of Modern Physics D*, **20**, 1745
- Dominik M., Belczynski K., Fryer C., Holz D. E., Berti E., Bulik T., Mandel L., O’Shaughnessy R., 2012, *ApJ*, **759**, 52
- Eichler D., Livio M., Piran T., Schramm D. N., 1989, *Nature*, **340**, 126
- Fox D. B., et al., 2005, *Nature*, **437**, 845
- Frail D. A., Kulkarni S. R., Nicastro L., Feroci M., Taylor G. B., 1997, *Nature*, **389**, 261
- Frontera F., et al., 1998, *ApJ*, **493**, L67
- Fryer C. L., Woosley S. E., Hartmann D. H., 1999, *The Astrophysical Journal*, **526**, 152
- Fryer C. L., et al., 2007, *PASP*, **119**, 1211
- Fryer C. L., Rueda J. A., Ruffini R., 2014, *ApJ*, **793**, L36
- Fryer C. L., Oliveira F. G., Rueda J. A., Ruffini R., 2015, *Physical Review Letters*, **115**, 231102
- Fujisawa K., Okawa H., Yamamoto Y., Yamada S., 2019, *ApJ*, **872**, 155
- Galama T. J., et al., 1998, *Nature*, **395**, 670
- Gehrels N., et al., 2005, *Nature*, **437**, 851
- Giacconi R., 2003, *Reviews of Modern Physics*, **75**, 995
- Giacconi R., Ruffini R., eds, 1978, *Physics and astrophysics of neutron stars and black holes*
- Gilks A., 2018, *MNRAS*, **474**, 2419
- Gill P. R.; Murray W., Wright M. H., 1981, 500, 136
- Giommi P., et al., 2020, arXiv e-prints, p. arXiv:2003.05153
- Giuliani A., et al., 2008, *A&A*, **491**, L25
- Greiner J., et al., 2009, *A&A*, **498**, 89
- Guetta D., Della Valle M., 2007, *ApJ*, **657**, L73
- Gursky H., Ruffini R., eds, 1975, *Neutron stars, black holes and binary X-ray sources; Proceedings of the Annual Meeting, San Francisco, Calif., February 28, 1974 Astrophysics and Space Science Library Vol. 48*
- Hawking S. W., 1971, *Physical Review Letters*, **26**, 1344
- Hawking S. W., 1972, *Commun. Math. Phys.*, **25**, 152

- Hewish A., Bell S. J., Pilkington J. D. H., Scott P. F., Collins R. A., 1968, *Nature*, **217**, 709
- Hjorth J., Bloom J. S., 2012, *The Gamma-Ray Burst - Supernova Connection*. Cambridge University Press (Cambridge), pp 169–190
- Hurley K., et al., 2000, *ApJ*, **534**, L23
- Iwamoto K., Nomoto K., Höflich P., Yamaoka H., Kumagai S., Shigeyama T., 1994, *ApJ*, **437**, L115
- Izzo L., et al., 2018, GRB Coordinates Network, **23142**, 1
- Kanbach G., 1996, *Mem. Soc. Astron. Italiana*, **67**, 161
- Klebesadel R. W., Strong I. B., Olson R. A., 1973, *ApJ*, **182**, L85
- Kouveliotou C., Meegan C. A., Fishman G. J., Bhat N. P., Briggs M. S., Koshut T. M., Paciesas W. S., Pendleton G. N., 1993, *ApJ*, **413**, L101
- Kumar P., Barniol Duran R., 2009, *MNRAS*, **400**, L75
- Li L., 2020, *ApJ*, **894**, 100
- Li L.-X., Paczyński B., 1998, *ApJ*, **507**, L59
- Li L.-X., Paczyński B., 2000, *ApJ*, **534**, L197
- Li L.-X., Paczyński B., 2006, *MNRAS*, **366**, 219
- Li L., et al., 2012, *ApJ*, **758**, 27
- Li L., et al., 2015, *ApJ*, **805**, 13
- Li L., Wang Y., Shao L., Wu X.-F., Huang Y.-F., Zhang B., Ryde F., Yu H.-F., 2018a, *ApJS*, **234**, 26
- Li L., Wu X.-F., Lei W.-H., Dai Z.-G., Liang E.-W., Ryde F., 2018b, *ApJS*, **236**, 26
- Li L., Ruffini R., Rueda J. A., Moradi R., Wang Y., Xue S. S., 2019, arXiv e-prints, p. arXiv:1910.12615
- MAGIC Collaboration et al., 2019a, *Nature*, **575**, 455
- MAGIC Collaboration et al., 2019b, *Nature*, **575**, 459
- Mao S., Paczynski B., 1992, *ApJ*, **388**, L45
- Meegan C. A., Fishman G. J., Wilson R. B., Paciesas W. S., Pendleton G. N., Horack J. M., Brock M. N., Kouveliotou C., 1992, *Nature*, **355**, 143
- Meegan C. A., et al., 2008, *GCN*, **8100**, 1
- Meegan C., et al., 2009, *ApJ*, **702**, 791
- Mészáros P., Rees M. J., 1997, *The Astrophysical Journal Letters*, **482**, L29
- Metzger M. R., Djorgovski S. G., Kulkarni S. R., Steidel C. C., Adelberger K. L., Frail D. A., Costa E., Frontera F., 1997, *Nature*, **387**, 878
- Moradi R., Rueda J. A., Ruffini R., Wang Y., 2019, arXiv e-prints, p. arXiv:1911.07552
- Murdin P., ed. 2000, *Compton Gamma Ray Observatory (CGRO)*. p. 4537, doi:10.1888/0333750888/4537
- Nakamura K., Kuroda T., Takiwaki T., Kotake K., 2014, *ApJ*, **793**, 45
- Nappo F., et al., 2017, *A&A*, **598**, A23
- Narayan R., Piran T., Shemi A., 1991, *ApJ*, **379**, L17
- Narayan R., Paczynski B., Piran T., 1992, *ApJ*, **395**, L83
- Nava L., 2018, preprint, (arXiv:1804.01524)
- Nomoto K., Hashimoto M., 1988, *Phys. Rep.*, **163**, 13
- Nousek J. A., et al., 2006, *ApJ*, **642**, 389
- Oke J. B., et al., 1995, *PASP*, **107**, 375
- Paciesas W. S., et al., 1999, *ApJS*, **122**, 465
- Paczynski B., 1986, *ApJ*, **308**, L43
- Panaitescu A., 2017, *ApJ*, **837**, 13
- Papapetrou A., 1966, *Annales de L'Institut Henri Poincare Section (A) Physique Theorique*, **4**, 83
- Pian E., et al., 2000, *ApJ*, **536**, 778
- Pisani G. B., et al., 2016, *ApJ*, **833**, 159
- Pisani G. B., et al., 2018, in *European Physical Journal Web of Conferences*. p. 04002, doi:10.1051/epjconf/201816804002
- Postnov K. A., Yungelson L. R., 2014, *Living Reviews in Relativity*, **17**, 3
- R. Mirzoyan et al., 2019, GRB Coordinates Network
- Racusin J. L., et al., 2011, *ApJ*, **738**, L38
- Rees M. J., Meszaros P., 1992, *MNRAS*, **258**, 41P
- Reifenstein E. C., Brundage W. D., Staelin D. H., 1969, *Phys. Rev. Lett.*, **22**, 311
- Rhoades C. E., Ruffini R., 1974, *Phys. Rev. Lett.*, **32**, 324
- Roming P. W. A., et al., 2005, *Space Sci. Rev.*, **120**, 95
- Rueda J. A., Ruffini R., 2012, *ApJ*, **758**, L7
- Rueda J. A., Ruffini R., 2020, *European Physical Journal C*, **80**, 300
- Rueda J. A., Ruffini R., Karlica M., Moradi R., Wang Y., 2020, *ApJ*, **893**, 148
- Ruffini R., 1974, in *Astrophysics and Gravitation: Proceedings of the Sixteenth Solvay Conference on Physics*. Editions de l'Universite de Bruxelles, pp 349–424
- Ruffini R., 1998, in Sato H., Sugiyama N., eds, *Frontiers Science Series 23: Black Holes and High Energy Astrophysics*. p. 167
- Ruffini R., Wheeler J. A., 1971, *Physics Today*, **24**, 30
- Ruffini R., Bianco C. L., Frascchetti F., Xue S.-S., Chardonnet P., 2001, *ApJ*, **555**, L117
- Ruffini R., et al., 2015a, *Astronomy Reports*, **59**, 626
- Ruffini R., et al., 2015b, *ApJ*, **798**, 10
- Ruffini R., et al., 2016a, *ApJ*, **831**, 178
- Ruffini R., et al., 2016b, *ApJ*, **832**, 136
- Ruffini R., et al., 2018a, *ApJ*, **852**, 53
- Ruffini R., Karlica M., Sahakyan N., Rueda J. A., Wang Y., Mathews G. J., Bianco C. L., Muccino M., 2018b, *ApJ*, **869**, 101
- Ruffini R., et al., 2018c, *ApJ*, **869**, 151
- Ruffini R., et al., 2019a, arXiv e-prints,
- Ruffini R., Melon Fuksman J. D., Vereshchagin G. V., 2019b, *ApJ*, **883**, 191
- Ruffini R., et al., 2019c, *ApJ*, **886**, 82
- Ruffini R., Bianco C. L., Frascchetti F., Xue S.-S., Chardonnet P., 2001c, *ApJ*, **555**, L117
- Sari R., 1997, *ApJ*, **489**, L37
- Sari R., Piran T., 1995, *ApJ*, **455**, L143
- Sari R., Piran T., Narayan R., 1998, *ApJ*, **497**, L17
- Shirasaki Y., et al., 2008, *PASJ*, **60**, 919
- Shklovskij I. S., 1969, *Supernovae.. Interscience Publishers*
- Smith N., Li W., Silverman J. M., Ganeshalingam M., Filippenko A. V., 2011, *MNRAS*, **415**, 773
- Staelin D. H., Reifenstein Edward C. I., 1968, *Science*, **162**, 1481
- Strong I. B., 1975, *Cosmic gamma-ray bursts..* pp 47–58, doi:10.1007/978-94-010-1767-1_3
- Tam P.-H. T., He X.-B., Tang Q.-W., Wang X.-Y., 2017, *ApJ*, **844**, L7
- Tauris T. M., Langer N., Moriya T. J., Podsiadlowski P., Yoon S.-C., Blinnikov S. I., 2013, *ApJ*, **778**, L23
- Tauris T. M., Langer N., Podsiadlowski P., 2015, *MNRAS*, **451**, 2123
- Tavani M., et al., 2009, *A&A*, **502**, 995
- Vernet J., et al., 2011, *A&A*, **536**, A105
- Wald R. M., 1974, *Phys. Rev. D*, **10**, 1680
- Wang Y., Rueda J. A., Ruffini R., Becerra L., Bianco C., Becerra L., Li L., Karlica M., 2019, *ApJ*, **874**, 39
- Waxman E., Piran T., 1994, *ApJ*, **433**, L85
- Wijers R. A. M. J., Rees M. J., Meszaros P., 1997, *MNRAS*, **288**, L51
- Woosley S. E., 1993, *ApJ*, **405**, 273
- Woosley S. E., Bloom J. S., 2006, *ARA&A*, **44**, 507
- Xu D., et al., 2013, *ApJ*, **776**, 98
- Yoon S.-C., Woosley S. E., Langer N., 2010, *ApJ*, **725**, 940
- Zhang B., 2018, *The Physics of Gamma-Ray Bursts*, doi:10.1017/9781139226530.
- Zhang B., Fan Y. Z., Dyks J., Kobayashi S., Mészáros P., Burrows D. N., Nousek J. A., Gehrels N., 2006, *ApJ*, **642**, 354
- de Pasquale M., et al., 2006, *A&A*, **455**, 813
- in 't Zand J. J. M., et al., 1998, *ApJ*, **505**, L119
- in 't Zand J. J. M., et al., 2001, *ApJ*, **559**, 710
- van Paradijs J., et al., 1997, *Nature*, **386**, 686

APPENDIX A: UPDATED BDHNE I LIST: BDHNE I WITHIN 2017–2018

The list of BdHNe I consists of 345 sources² within 1997–2016 published in Ruffini et al. (2018a). Therein 152 bursts occurred before the launch of *Fermi* space mission. The first event detected by *Fermi*-GBM was the object GRB 080810 reported in GCN 8100 Meegan

² https://iopscience.iop.org/0004-637X/852/1/53/suppdata/apjaa9e8bt9_mrt.txt

et al. (2008). Consequently, the further 193 events of the list occurred within operational era of *Fermi* observatory.

BdHNe I are all the GRBs which satisfy the following criteria Pisani et al. (2018):

- measured redshift z ;
- GRB rest-frame duration larger than 2 s;
- isotropic energy $E_{\gamma,\text{iso}}$ larger than $\sim 10^{52}$ erg;
- presence of associated *Swift*-XRT data.

For fitting the X-ray afterglow in Pisani et al. (2016) only the ones having *Swift*-XRT data lasting at least up to $t_{\text{rf}} = 10^4$ s have been considered, which shows a distribution of power-law index follows a Gaussian behavior with a value of $\alpha_X = -1.48 \pm 0.32$.

In order to update the BdHNe I list with ones occurred within 2017–2018 we go through the all triggered bursts. To have a comprehensive list we use several sources of information^{3 4 5 6} and cross-correlate data on each GRB.

There are 197 (2017) and 164 (2018) events in total classified as GRBs and reported in GCN circulars. Among them 17 (2017) and 16 (2018) bursts have the measured redshift values. These 33 GRBs are represented by 31 long and 2 short duration bursts. In total of 31 long events the *Fermi*-GBM triggered in 16 cases while the rest objects were observed by different instruments—*Konus*-WIND and *Swift*-BAT, etc.

In Table A1 we present GRB list with measured redshift values within January 2017–December 2018. The values of redshift z and duration T_{90} are retrieved from GCN and literature. The values of isotropic-equivalent energy $E_{\gamma,\text{iso}}$ are calculated using the spectral parameters (α , β , $E_{p,i}$, etc.) of the model best-fitting the T_{90} interval defined within [50–300] keV band and reported in appropriate GCN, preferentially by *Fermi*-GBM team. Note that the preference for duration info and best-fit was given to *Fermi*-GBM (denoted with full name in parenthesis), then if absent—to *Konus*-WIND (denoted as *KW), then if absent—to *Swift*-BAT (denoted as *SW), and the motivation for such a gradation stays on different energy bands used to define T_{90} value. The subsequent data on spectral fit should be understood as attributed to the analysis on substitute instruments when indicated. The boresight angle θ with respect to *Fermi*-LAT instrument is an off-axis angle defined at the trigger moment.

In Table A2 we present the above list narrowed to the BdHNe I which fell within *Fermi*-LAT FoV at the trigger. Additional information includes whether the high-energy photons were detected, and if so, the calculated value of energy E_{LAT} is given together with test statistic (TS) value of the signal to be associated with GRB. The bursts observed by other instruments lack the information on *Fermi*-LAT boresight angle and consequently no observations in high-energy domain were carried out. Therefore, consideration of that events is not possible even their energy values are sufficient ($E_{\gamma,\text{iso}} \gtrsim 10^{52}$ erg) and GRBs are classified as BdHNe I.

We present here in Table A3 the complete list of the 378 BdHNe observed up through the end of 2018, which includes the 161 BdHNe already presented in Pisani et al. (2016) and 345 BdHNe already presented in Ruffini et al. (2018a).

³ https://gcn.gsfc.nasa.gov/gcn3_archive.html

⁴ <https://heasarc.gsfc.nasa.gov/W3Browse/fermi/fermigbrst.html>

⁵ <https://heasarc.gsfc.nasa.gov/W3Browse/fermi/fermilgrb.html>

⁶ <http://www.mpe.mpg.de/~jcg/grbgen.html>

#	GRB	z	T_{90} (s)	Best-fit (model)	α	β	$E_{p,i}$ (keV)	$E_{\gamma,iso}$ ($\times 10^{52}$ erg)	θ (deg)	References
1	170113A (420)	1.968	49.2	PL	-1.95 ± 0.08	—	—	19.91	145.0	20452, 20458
2	170202A *KW	3.645	30.0	CPL	$-1.16^{+0.59}_{-0.34}$	—	$247.0^{+166.0}_{-86.0}$	17.0	—	20584, 20588, 20590, 20604 *KW
3	170214A (649)	2.53	122.9	SBPL	-1.063 ± 0.008	-2.246 ± 0.038	253.4 ± 10.4	...	33.2	20675, 20686
4	170405A (777)	3.51	78.6	Band	-0.799 ± 0.020	-2.354 ± 0.089	267.0 ± 9.3	241.01	52.0	20990, 20986
5	170428A *KW	0.454	0.14	Band	$-0.47^{+0.28}_{-0.21}$	$-2.46^{+0.52}_{-7.54}$	$982.0^{+394.0}_{-355.0}$...	—	21059, 21045 *KW
6	170519A *SW	0.818	216.4	PL	-1.94 ± 0.26	—	—	...	—	21119, 21112 *SW
7	170531B *SW	2.366	164.1	PL	-1.95 ± 0.14	—	—	...	—	21177, 21209, 21186 *SW
8	170604A *KW	1.329	30.0	CPL	$-1.31^{+0.26}_{-0.20}$	—	$220.0^{+72.0}_{-48.0}$	4.7 ± 0.6	—	21197, 21247 *KW
9	170607A (971)	0.557	20.9	CPL	-1.401 ± 0.044	—	145.2 ± 11.9	1.13	100.0	21240, 21218
10	170705A (115)	2.01	22.8	Band	-0.991 ± 0.069	-2.303 ± 0.108	97.9 ± 7.6	14.95	118.0	21298, 21297
11	170714A *SW	0.793	537.3	PL	-1.76 ± 0.17	—	—	...	—	21359, 21347 *SW
12	170817A (529)	0.0093	2.0	PL	-1.428 ± 0.094	—	—	...	91.0	—
13	170903A (534)	0.886	25.6	CPL	-1.316 ± 0.108	—	95.6 ± 13.4	1.15	93.0	21799, 21812
14	171010A (792)	0.3285	107.3	Band	-1.089 ± 0.006	-2.191 ± 0.009	137.7 ± 1.4	14.49	114.7	22002, 22096, 21992
15	171020A *SW	1.87	41.9	PL	-1.04 ± 0.20	—	—	...	—	22039, 22038 *SW
16	171205A *KW	0.0368	145.0	PL	-2.0 ± 0.18	—	—	0.0024	—	22180, 22227 *KW
17	171222A (684)	2.409	80.4	PL	-2.068 ± 0.059	—	—	20.73	43.0	22272, 22277
18	180115A *SW	2.487	40.9	PL	-1.66 ± 0.22	—	—	...	—	22346, 22348 *SW
19	180205A (184)	1.409	15.4	PL	-1.887 ± 0.052	—	—	3.06	94.0	22384, 22386
20	180314A (030)	1.445	22.0	CPL	-0.445 ± 0.055	—	106.2 ± 2.9	6.58	99.0	22484, 22485
21	180325A *KW	2.248	10.0	Band	$-0.50^{+0.21}_{-0.19}$	$-2.65^{+0.31}_{-1.06}$	$306.0^{+50.0}_{-39.0}$	23.0	—	22535, 22555, 22546 *KW
22	180329B *SW	1.998	210.0	CPL	-0.97 ± 0.56	—	48.6 ± 9.1	...	—	22567, 22566 *SW
23	180404A *SW	1.000	35.2	PL	-1.95 ± 0.12	—	—	...	—	22591, 22599 *SW
24	180510B *SW	1.305	134.3	PL	-2.00 ± 0.17	—	—	...	—	22702, 22705 *SW
25	180620B (660)	1.1175	46.7	Band	-1.206 ± 0.116	-1.660 ± 0.035	175.6 ± 49.8	16.30	137.0	22823, 22813
26	180624A *SW	2.855	486.4	PL	-1.91 ± 0.10	—	—	...	—	22845, 22848 *SW
27	180703A (876)	0.6678	20.7	Band	-0.776 ± 0.041	-1.967 ± 0.103	350.8 ± 32.2	3.15	44.0	23889, 22896
28	180720B (598)	0.654	48.9	Band	-1.171 ± 0.005	-2.490 ± 0.071	636.0 ± 15.4	19.08	49.1	22996, 22981
29	180728A (728)	0.117	6.4	Band	-1.54 ± 0.01	-2.46 ± 0.02	79.2 ± 1.4	...	35.0	23055, 23067, 23053
30	180914B *KW	1.096	280.0	Band	$-0.81^{+0.04}_{-0.04}$	$-2.12^{+0.08}_{-0.7}$	$466.0^{+29.0}_{-27.0}$	360.0	94.0	23246, 23240 *KW
31	181010A (247)	1.39	9.7	CPL	-0.8 ± 0.2	—	280.0 ± 80.0	...	48.1	23315, 23320
32	181020A (792)	2.938	15.1	Band	-0.70 ± 0.02	-2.06 ± 0.07	367.0 ± 17.0	...	50.0	23356, 23352
33	181110A *KW	1.505	140.0	CPL	$-1.63^{+0.34}_{-0.26}$	—	$48.0^{+14.0}_{-27.0}$	11.0	—	23421, 23424 *KW

Table A1. List of 33 GRBs with measured redshift values within January 2017–December 2018. Four criteria were applied (columns from left to right) to the sample and highlighted elements are consistent with their requirements.

BdHN	z	T_{90} (s)	$E_{\gamma,iso}$ ($\times 10^{52}$ erg)	θ (deg)	GeV photons	E_{LAT} ($\times 10^{52}$ erg)	TS	References
170214A (649)	2.53	122.9	...	33.2	Yes	—	—	20675 (z), 20686 (GBM)
170405A (777)	3.51	78.6	241.01	52.0	Yes	—	—	20990 (z), 20986 (GBM)
171222A (684)	2.409	80.4	20.73	43.0	No	—	—	22272 (z), 22277 (GBM)
180703A (876)	0.6678	20.7	3.15	44.0	No	—	—	23889 (z), 22896 (GBM)
180720B (598)	0.654	48.9	19.08	49.1	Yes	—	—	22996 (z), 22981 (GBM)
180728A (728)	0.117	6.4	...	35.0	—	—	—	23055 (z), 23067 (z), 23053 (GBM)
181010A (247)	1.39	9.7	...	48.1	—	—	—	23315 (z), 23320 (GBM)
181020A (792)	2.938	15.1	...	50.0	—	—	—	23356 (z), 23352 (GBM)

Table A2. List of BdHNE I within January 2017–December 2018 with boresight angle $\theta \lesssim 75^\circ$ at the trigger.



Table A3: continued.

GRB	z	$E_{\text{iso}}^{(a)}$	LX ^(b)	Early flare ^(c)	UL ^(d)	$T_{90}^{(e)}$	Instrument ^(f)	Reference ^(g)
<p>Table A3: List of the 378 BdHNe during 14 years of Swift/XRT observation activity, updated in this work. We report: the redshift z, the isotropic energy E_{iso}, the instrument which detected the sources in the gamma-ray band, and the reference from which the gamma-ray spectral parameters are taken in order to evaluate the E_{iso}.</p> <p>(a): in units of 10^{52} erg.</p> <p>(b): “LX” indicates the sources with Swift/XRT data observed up to times larger than $t_{\text{rf}} \sim 10^4$ s after the trigger time.</p> <p>(c): “C” and “E” represent the sources with early flares in their Swift/XRT, and they stand for “confirmed” and “excluded” respectively; see Ruffini et al. (2018a).</p> <p>(d): “UL” indicates the sources with $T_{90} \gtrsim 1000$ s known as ultra-long GRBs.</p> <p>(e): observed T_{90} (s).</p> <p>(f): “B-SAX” stands for Beppo-SAX/GRBM; “BATSE” stands for Compton-GRO-BATSE; “Ulysses” stands for Ulysses-GRB; “KW” stands for Konus-WIND; “HETE” stands for HETE-2-FREGATE; “Swift” stands for Swift-BAT; “Fermi” stands for Fermi-GBM.</p> <p>(g): (1) Frontera et al. (1998); (2) Ruffini et al. (2015a); (3) in ’t Zand et al. (1998); (4) Amati et al. (2000); (5) Hurley et al. (2000); (6) in’t Zand et al. (2001); (7) Barraud et al. (2003); (8) Shirasaki et al. (2008); (9) Cenko et al. (2006).</p>								
970228	0.695	1.65 ± 0.16				80	B-SAX	(1)
970828	0.958	30.4 ± 3.6				90	BATSE	(2)
971214	3.42	22.1 ± 2.7				40	BATSE	IAUC 6789
980329	3.5	267 ± 53				54	B-SAX	(3)
980703	0.966	7.42 ± 0.74				400	BATSE	GCN 143
990123	1.6	241 ± 39				63.3	BATSE	GCN 224
990506	1.3	98.1 ± 9.9				131.33	BATSE	GCN 306
990510	1.619	18.1 ± 2.7				75	BATSE	GCN 322
990705	0.842	18.7 ± 2.7				42	B-SAX	(4)
991208	0.706	23.0 ± 2.3				68	Ulysses	(5)
991216	1.02	69.8 ± 7.2				15.17	BATSE	GCN 504
000131	4.5	184 ± 32				50	KW+Ulysses	GCN 529
000210	0.846	15.4 ± 1.7				12.3	BATSE	GCN 540
000301C	2.0335	4.96 ± 0.50				10	Ulysses	GCN 568
000418	1.12	9.5 ± 1.8				30	KW+Ulysses	GCN 642
000911	1.06	70 ± 14				500	KW+Ulysses	GCN 791
000926	2.07	28.6 ± 6.2				25	KW+Ulysses	GCN 801
010222	1.48	84.9 ± 9.0				170	B-SAX	(6)
010921	0.45	0.97 ± 0.10				12	HETE	GCN 1096
011121	0.36	8.0 ± 2.2				28	Ulysses	GCN 1148
011211	2.14	5.74 ± 0.64				270	B-SAX	GCN 1215
020124	3.2	28.5 ± 2.8				78.6	HETE	(7)
020127	1.9	3.73 ± 0.37				9.3	HETE	(7)
020405	0.69	10.6 ± 1.1				40	KW+Ulysses	GCN 1325
020813	1.25	68 ± 17				90	HETE	(7)
021004	2.3	3.47 ± 0.46				57.7	HETE	(7)
021211	1.01	1.16 ± 0.13				5.7	HETE	GCN 1734
030226	1.98	12.7 ± 1.4				100	HETE	GCN 1888
030323	3.37	2.94 ± 0.92				26	HETE	GCN 1956
030328	1.52	38.9 ± 3.9				100	HETE	GCN 1978
030329	0.169	1.62 ± 0.16				50	HETE	IAUC 8101
030429	2.65	2.29 ± 0.27				14	HETE	GCN 2211
030528	0.78	2.22 ± 0.27				21.6	HETE	GCN 2256
040912	1.563	1.36 ± 0.36				122	HETE	GCN 2723
040924	0.859	0.98 ± 0.10				2.4	KW	GCN 2754
041006	0.716	3.11 ± 0.89				27.3	HETE	(8)

Table A3: continued.

GRB	z	$E_{\text{iso}}^{(a)}$	LX ^(b)	Early flare ^(c)	UL ^(d)	$T_{90}^{(e)}$	Instrument ^(f)	Reference ^(g)
041219A	0.31	10.0 ± 1.0				520	Swift	GCN 2874
050126	1.29	2.47 ± 0.25				26	Swift	GCN 2987
050315	1.95	6.15 ± 0.30	LX			96	Swift	GCN 3099
050318	1.444	2.30 ± 0.23	LX			32	Swift	GCN 3134
050319	3.243	4.63 ± 0.56	LX			10	Swift	GCN 3119
050401	2.898	37.6 ± 7.3	LX			33	KW	GCN 3179
050408	1.2357	2.48 ± 0.25	LX			34	HETE	GCN 3188
050502B	5.2	2.66 ± 0.22				17.5	Swift	GCN 3339
050505	4.27	16.0 ± 1.1	LX			60	Swift	GCN 3364
050525A	0.606	2.30 ± 0.49	LX			5.2	KW	GCN 3479
050603	2.821	64.1 ± 6.4				6	KW	GCN 3518
050714B	2.4383	4.99 ± 0.85				46.7	Swift	GCN 3615
050730	3.969	11.8 ± 0.8	LX			155	Swift	GCN 3715
050802	1.71	5.66 ± 0.47	LX			13	Swift	GCN 3737
050803	4.3	1.16 ± 0.12	LX	E		85	Swift	GCN 3757
050814	5.3	9.9 ± 1.1	LX			65	Swift	GCN 3783
050819	2.5043	3.60 ± 0.55				36	Swift	GCN 3828
050820	2.615	103 ± 10	LX			549.2	KW	(9)
050822	1.434	10.8 ± 1.1	LX	E		102	Swift	GCN 3856
050904	6.295	133 ± 14				225	Swift	GCN 3938
050908	3.347	1.54 ± 0.16				20	Swift	GCN 3951
050915	2.5273	1.8 ± 1.3				53	Swift	GCN 3982
050922B	4.9	46.4 ± 4.6	LX	E		980	Swift	GCN 4019
050922C	2.199	5.6 ± 1.8	LX			8.4	KW	GCN 4030
051001	2.4296	2.3 ± 1.7				190	Swift	GCN 4052
051006	1.059	1.02 ± 0.56				26	Swift	GCN 4063
051008	2.77	115 ± 20				280	KW	GCN 4078
051022	0.8	56.0 ± 5.6				200	KW	GCN 4150
051109A	2.346	6.85 ± 0.73	LX			130	KW	GCN 4238
051111	1.55	15.4 ± 1.9				47	KW	GCN 4260
060108	2.03	1.51 ± 1.33	LX			14.4	Swift	GCN 4445
060111	2.32	1.62 ± 0.08	LX	E		13	Swift	GCN 4486
060115	3.533	5.9 ± 3.8	LX			142	Swift	GCN 4518
060124	2.296	43.8 ± 6.4	LX			300	KW	GCN 4599
060202	0.785	1.20 ± 0.09	LX			203.7	Swift	GCN 4635
060204B	2.3393	29.3 ± 6.0	LX	C		134	Swift	GCN 4671
060206	4.056	4.1 ± 1.9	LX			7	Swift	GCN 4697
060210	3.91	32.2 ± 3.2	LX			255	Swift	GCN 4748
060223	4.41	9.73 ± 0.72				11	Swift	GCN 4820
060306	3.5	7.6 ± 1.0				61	Swift	GCN 4851
060418	1.489	13.5 ± 2.7	LX			52	Swift	GCN 4975
060502A	1.51	10.57 ± 0.48	LX			33	Swift	GCN 5053
060510B	4.9	19.1 ± 0.8	LX			276	Swift	GCN 5107
060512	2.1	2.38 ± 2.70	LX			8.6	Swift	GCN 5124
060522	5.11	6.47 ± 0.63				69	Swift	GCN 5153
060526	3.22	2.75 ± 0.37	LX			298	Swift	GCN 5174
060602A	0.787	6.63 ± 0.41				60	Swift	GCN 5206
060605	3.773	4.23 ± 0.61	LX			15	Swift	GCN 5231
060607A	3.082	21.4 ± 11.9	LX	C		100	Swift	GCN 5242
060707	3.424	4.3 ± 1.1	LX			68	Swift	GCN 5289
060708	1.92	1.06 ± 0.08	LX			9.8	Swift	GCN 5295
060714	2.7108	7.67 ± 0.44	LX			115	Swift	GCN 5334
060719	1.532	1.4 ± 1.3				55	Swift	GCN 5349
060729	0.54	1.20 ± 0.53	LX	E		116	Swift	GCN 5370
060814	1.923	56.7 ± 5.7	LX			40	KW	GCN 5460
060906	3.6856	7.81 ± 0.51	LX			43.6	Swift	GCN 5538
060908	1.884	7.2 ± 1.9				19.3	Swift	GCN 5551
060923B	1.5094	2.71 ± 0.34				8.8	Swift	GCN 5595
060926	3.2086	2.29 ± 0.37				8	Swift	GCN 5621

Table A3: continued.

GRB	z	$E_{\text{iso}}^{(a)}$	LX ^(b)	Early flare ^(c)	UL ^(d)	$T_{90}^{(e)}$	Instrument ^(f)	Reference ^(g)
060927	5.46	12.0 ± 2.8				22.6	Swift	GCN 5639
061007	1.262	90.0 ± 9.0	LX			75	KW	GCN 5722
061110B	3.4344	17.9 ± 1.6				128	Swift	GCN 5810
061121	1.314	23.5 ± 2.7	LX			81	Swift	GCN 5831
061126	1.1588	31.4 ± 3.6	LX			191	Swift	GCN 5860
061202	2.2543	21.99 ± 0.63				91	Swift	GCN 5887
061222A	2.088	30.0 ± 6.4	LX			72	Swift	GCN 5964
061222B	3.355	8.1 ± 1.5				40	Swift	GCN 5974
070110	2.3521	4.98 ± 0.30	LX			85	Swift	GCN 6007
070125	1.547	84.1 ± 8.4				75	Swift	GCN 6049
070129	2.3384	16.8 ± 1.7	LX	E		460	Swift	GCN 6058
070223	1.6295	4.73 ± 0.28				89	Swift	GCN 6132
070224	1.9922	2.37 ± 0.28				34	Swift	GCN 6141
070306	1.4959	8.26 ± 0.41	LX			210	Swift	GCN 6173
070318	0.84	3.41 ± 2.14	LX	C		63	Swift	GCN 6212
070328	2.0627	56.7 ± 7.7				45	KW	GCN 6230
070411	2.954	8.31 ± 0.45				101	Swift	GCN 6274
070419B	1.959	12.1 ± 1.7				236.5	Swift	GCN 6327
070508	0.82	7.74 ± 0.29	LX			40	KW	GCN 6403
070521	1.35	10.8 ± 1.8				55	KW	GCN 6459
070529	2.4996	12.8 ± 1.1	LX			109	Swift	GCN 6468
070611	2.0394	0.92 ± 0.13				12	Swift	GCN 6502
070612A	0.617	1.96 ± 0.40				370	Swift	GCN 6522
070721B	3.6298	24.2 ± 1.4				340	Swift	GCN 6649
070802A	2.45	1.65 ± 2.78	LX			16.4	Swift	GCN 6699
070810A	2.17	91.5 ± 1.1				11	Swift	GCN 6748
071003	1.604	38.3 ± 4.5	LX			30	KW	GCN 6849
071010B	0.947	2.32 ± 0.40				16.6	KW	GCN 6879
071020	2.145	10.0 ± 4.6				8.45	KW	GCN 6960
071021	2.452	8.18 ± 0.82	LX	E		225	Swift	GCN 6966
071025	5.2	115 ± 4				109	Swift	GCN 6996
071031	2.6918	4.99 ± 0.97				180	Swift	GCN 7029
071112C	0.823	15.7 ± 2.1				15	Swift	GCN 7081
071117	1.331	5.86 ± 2.7				5	KW	GCN 7114
080129	4.349	7.7 ± 3.5				48	Swift	GCN 7235
080205	2.72	15.21 ± 0.72				106.5	Swift	GCN 7257
080207	2.0858	16.4 ± 1.8				340	Swift	GCN 7272
080210	2.6419	4.77 ± 0.29	LX			45	Swift	GCN 7289
080310	2.4274	20.9 ± 2.1	LX	E		365	Swift	GCN 7402
080319A	2.0265	27.0 ± 2.2				64	Swift	GCN 7447
080319B	0.937	118 ± 12	LX			50	KW	GCN 7482
080319C	1.95	14.9 ± 3.0	LX			15	KW	GCN 7487
080325	1.78	9.55 ± 0.84				128.4	Swift	GCN 7531
080411	1.03	16.2 ± 1.6				70	KW	GCN 7589
080413A	2.433	8.6 ± 2.1				46	Swift	GCN 7604
080413B	1.1	1.61 ± 0.27				8	Swift	GCN 7606
080514B	1.8	18.1 ± 3.6				7	KW	GCN 7751
080515	2.47	5.11 ± 0.77				21	Swift	GCN 7726
080602	1.8204	6.08 ± 0.38				74	Swift	GCN 7786
080603B	2.69	6.0 ± 3.1				70	KW	GCN 7812
080604	1.4171	1.05 ± 0.12				82	Swift	GCN 7817
080605	1.64	28 ± 14	LX			20	Swift	GCN 7854
080607	3.04	187 ± 11	LX	C		85	KW	GCN 7862
080710	0.8454	1.68 ± 0.22				120	Swift	GCN 7969
080721	2.591	134 ± 23	LX			30	KW	GCN 7995
080804	2.205	12.0 ± 1.2	LX			34	Swift	GCN 8067
080805	1.51	7.16 ± 1.90	LX	C		78	Swift	GCN 8068
080810	3.35	50.0 ± 4.4	LX	C		79.4	KW	GCN 8101
080825B	4.3	38.4 ± 3.8				110	KW	GCN 8142

Table A3: continued.

GRB	z	$E_{\text{iso}}^{(a)}$	LX ^(b)	Early flare ^(c)	UL ^(d)	$T_{90}^{(e)}$	Instrument ^(f)	Reference ^(g)
080905B	2.3739	4.55 ± 0.37	LX			128	Swift	GCN 8188
080906	2.1	21.2 ± 1.2				147	Swift	GCN 8196
080913	6.695	9.2 ± 2.7				8.8	KW	GCN 8280
080916A	0.689	0.98 ± 0.10				40	KW	GCN 8259
080916C	4.35	407 ± 86	LX			60	Fermi	GCN 8263
080928	1.692	3.99 ± 0.91	LX			66	Fermi	GCN 8278
081008	1.967	13.5 ± 6.6	LX	C		185.5	Swift	GCN 8351
081028	3.038	18.3 ± 1.8	LX			260	Swift	GCN 8428
081029	3.8479	12.1 ± 1.4				270	Swift	GCN 8447
081109	0.9787	1.81 ± 0.12	LX			45	Fermi	GCN 8505
081118	2.58	12.2 ± 1.2				20	Fermi	GCN 8550
081121	2.512	32.4 ± 3.7	LX			18	KW	GCN 8548
081203A	2.05	32 ± 12	LX			213	KW	GCN 8611
081210	2.0631	15.6 ± 5.4	LX	C		146	Swift	GCN 8649
081221	2.26	31.9 ± 3.2	LX			40	Fermi	GCN 8704
081222	2.77	27.4 ± 2.7	LX			30	Fermi	GCN 8715
081228	3.44	9.9 ± 2.0				3	Swift	GCN 8749
081230	2.0	3.21 ± 0.31				60.7	Swift	GCN 8759
090102A	1.547	22.6 ± 2.7	LX			30	KW	GCN 8776
090113A	1.7493	1.00 ± 0.17				9.1	Swift	GCN 8808
090201A	2.1	93.4 ± 8.1				110	KW	GCN 8878
090205A	4.6497	1.12 ± 0.16				8.8	Swift	GCN 8886
090313A	3.375	4.42 ± 0.79	LX			78	Swift	GCN 8986
090323A	3.57	438 ± 53				150	Fermi	GCN 9035
090328A	0.736	14.2 ± 1.4	LX			80	Fermi	GCN 9057
090404A	3	59.2 ± 6.1	LX	E		84	Swift	GCN 9089
090418A	1.608	17.2 ± 2.7	LX			64.8	KW+Swift	GCN 9196
090423A	8.26	8.8 ± 2.1	LX			12	Fermi	GCN 9229
090424A	0.544	4.07 ± 0.41	LX			52	Fermi	GCN 9230
090429B	9.3	6.7 ± 1.3				5.5	Swift	GCN 9290
090516A	4.109	99.6 ± 16.7	LX	C		350	Fermi	GCN 9415
090519A	3.85	24.7 ± 2.8				64	Swift	GCN 9406
090529A	2.625	2.56 ± 0.30				100	Swift	GCN 9434
090530A	1.266	1.73 ± 0.19				48	Swift	GCN 9443
090618A	0.54	28.6 ± 2.9	LX			113.2	Fermi	GCN 9535
090715B	3.	63.9 ± 3.7	LX	E		100	KW	GCN 9679
090726A	2.71	1.82 ± 0.40				67	Swift	GCN 9716
090809A	2.737	1.88 ± 0.26	LX			5.4	Swift	GCN 9756
090812A	2.452	44.0 ± 6.5	LX	C		64.8	KW+Swift	GCN 9821
090902B	1.822	292 ± 29.2	LX			21	Fermi	GCN 9866
090926A	2.106	228 ± 23	LX			20	Fermi	GCN 9933
090926B	1.24	4.14 ± 0.45				81	Fermi	GCN 9957
091003A	0.897	10.7 ± 1.8	LX			21.1	Fermi	GCN 9983
091020A	1.71	8.4 ± 1.1	LX			37	Fermi	GCN 10095
091024A	1.092	18.4 ± 2.0			UL	1250	KW	GCN 10083
091029A	2.752	7.97 ± 0.82	LX			39.2	Swift	GCN 10103
091109A	3.076	10.6 ± 1.4				48	Swift	GCN 10141
091127A	0.49	1.64 ± 0.18	LX			9	Fermi	GCN 10204
091208B	1.063	2.06 ± 0.21	LX			15	Fermi	GCN 10266
100219A	4.6667	3.93 ± 0.61				18.8	Swift	GCN 10434
100302A	4.813	1.33 ± 0.17	LX			17.9	Swift	GCN 10462
100414A	1.368	55.0 ± 5.5				26.4	Fermi	GCN 10595
100424A	2.465	3.05 ± 0.53				104	Swift	GCN 10670
100425A	1.755	2.76 ± 3.45	LX			37	Swift	GCN 10685
100513A	4.8	6.75 ± 0.53	LX			84	Swift	GCN 10753
100615A	1.398	5.81 ± 0.11				37.7	Fermi	GCN 10851
100621A	0.542	2.82 ± 0.35	LX			80	KW	GCN 10882
100728A	1.567	86.8 ± 8.7				162.9	Fermi	GCN 11006
100728B	2.106	3.55 ± 0.36				11.8	Fermi	GCN 11015

Table A3: continued.

GRB	z	$E_{\text{iso}}^{(a)}$	LX ^(b)	Early flare ^(c)	UL ^(d)	$T_{90}^{(e)}$	Instrument ^(f)	Reference ^(g)
100814A	1.44	15.3 ± 1.8	LX			149	Fermi	GCN 11099
100816A	0.8049	0.75 ± 0.10	LX			2	Fermi	GCN 11124
100901A	1.408	4.22 ± 0.50	LX			439	Swift	GCN 11169
100906A	1.727	29.9 ± 2.9	LX			105	Fermi	GCN 11248
101213A	0.414	2.72 ± 0.53				45	Fermi	GCN 11454
110128A	2.339	1.58 ± 0.21	LX			12	Fermi	GCN 11628
110205A	2.22	48.3 ± 6.4	LX			330	KW	GCN 11659
110213A	1.46	5.78 ± 0.81	LX			33	Fermi	GCN 11727
110213B	1.083	8.3 ± 1.3				50	KW	GCN 11722
110422A	1.77	79.8 ± 8.2	LX			40	KW	GCN 11971
110503A	1.613	20.8 ± 2.1	LX			12	KW	GCN 12008
110715A	0.82	4.36 ± 0.45	LX			20	KW	GCN 12166
110731A	2.83	49.5 ± 4.9	LX			7.3	Fermi	GCN 12221
110801A	1.858	10.9 ± 2.7				415.1	KW+Swift	GCN 12276
110808A	1.348	6.09 ± 4.83	LX			48	KW	GCN 12270
110818A	3.36	26.6 ± 2.8				75	Fermi	GCN 12287
110918A	0.982	185 ± 5	LX			22	KW	GCN 12362
111008A	4.9898	24.7 ± 1.2	LX			40	KW	GCN 12433
111107A	2.893	3.76 ± 0.55				12	Fermi	GCN 12545
111123A	3.1516	24 ± 14	LX			290	Swift	GCN 12598
111209A	0.677	5.14 ± 0.62	LX		UL	11900	KW	GCN 12663
111215A	2.06	22.1 ± 2.5				796	Swift	GCN 12689
111228A	0.716	2.75 ± 0.28	LX			101.2	Fermi	GCN 12744
120118B	2.943	6.24 ± 0.55				23.26	Swift	GCN 12873
120119A	1.728	27.2 ± 3.6	LX			55	Fermi	GCN 12874
120211A	2.4	7.1 ± 1.0				61.7	Swift	GCN 12924
120326A	1.798	3.27 ± 0.33	LX			12	Fermi	GCN 13145
120327A	2.813	14.42 ± 0.46	LX			62.9	Swift	GCN 13137
120404A	2.876	4.18 ± 0.34				38.7	Swift	GCN 13220
120521C	6.01	11.9 ± 1.9				26.7	Swift	GCN 13333
120624B	2.197	319 ± 32				271	Fermi	GCN 13377
120711A	1.405	180 ± 18	LX			44	Fermi	GCN 13437
120712A	4.175	21.2 ± 2.1	LX			23	Fermi	GCN 13469
120716A	2.486	30.2 ± 3.0				234	Fermi	GCN 13498
120802A	3.796	12.9 ± 2.8				50	Swift	GCN 13559
120805A	3.1	19.0 ± 3.2				48	Swift	GCN 13594
120811C	2.671	6.41 ± 0.64				26.8	Swift	GCN 13634
120815A	2.358	1.65 ± 0.27				9.7	Swift	GCN 13652
120909A	3.93	87 ± 10	LX			112	Fermi	GCN 13737
120922A	3.1	22.4 ± 1.4	LX			180	Fermi	GCN 13789
121024A	2.298	4.61 ± 0.55	LX			69	Swift	GCN 13899
121027A	1.773	1.50 ± 0.17	LX	E	UL	6000	Swift	GCN 13910
121128A	2.2	8.66 ± 0.87	LX			17	Fermi	GCN 14012
121201A	3.385	2.52 ± 0.34				85	Swift	GCN 14028
121209A	2.1	24.31 ± 0.84				42.7	Swift	GCN 14052
121217A	3.1	25.9 ± 19.7	LX			780	Fermi	GCN 14094
121229A	2.707	3.7 ± 1.1				100	Swift	GCN 14123
130408A	3.758	35.0 ± 6.4				15	KW	GCN 14368
130131B	2.539	7.15 ± 0.84				4.3	Swift	GCN 14164
130215A	0.597	4.45 ± 0.11				140	Fermi	GCN 14219
130408A	3.757	35.4 ± 5.9				15	KW	GCN 14368
130418A	1.218	9.9 ± 1.6	LX			120	KW	GCN 14417
130420A	1.297	7.74 ± 0.77	LX			102	Fermi	GCN 14429
130427A	0.334	92 ± 13	LX			162.8	Fermi	GCN 14473
130427B	2.78	13.3 ± 0.5	LX	E		27	Swift	GCN 14469
130505A	2.27	347 ± 35	LX			21	KW	GCN 14575
130514A	3.6	49.5 ± 9.2	LX	E		204	Swift	GCN 14636
130518A	2.488	193 ± 19				48	Fermi	GCN 14674
130528A	1.25	18.0 ± 2.3	LX	E		55	Fermi	GCN 14729

Table A3: continued.

GRB	z	$E_{\text{iso}}^{(a)}$	LX ^(b)	Early flare ^(c)	UL ^(d)	$T_{90}^{(e)}$	Instrument ^(f)	Reference ^(g)
130606A	5.91	28.3 ± 5.1	LX	E		165	KW	GCN 14808
130610A	2.092	6.99 ± 0.46	LX			28	Fermi	GCN 14858
130701A	1.155	2.60 ± 0.09	LX			5.5	KW	GCN 14958
130907A	1.238	304 ± 19	LX			214	KW	GCN 15203
130925A	0.347	3.23 ± 0.37	LX	E	UL	4500	Fermi	GCN 15261
131011A	1.874	86.67 ± 0.39				77	Fermi	GCN 15331
131030A	1.293	30.0 ± 2.0	LX	C		28	KW	GCN 15413
131105A	1.686	34.7 ± 1.2	LX			112	Fermi	GCN 15455
131108A	2.4	70.87 ± 0.97	LX			19	Fermi	GCN 15477
131117A	4.042	1.02 ± 0.16	LX			11	Swift	GCN 15499
131227A	5.3	24.2 ± 1.7				18	Swift	GCN 15620
140114A	3.0	27.6 ± 0.8	LX	E		139.7	Swift	GCN 15738
140206A	2.73	35.8 ± 7.9	LX	C		27	Fermi	GCN 15796
140213A	1.2076	9.93 ± 0.15	LX			18.6	Fermi	GCN 15833
140226A	1.98	5.8 ± 1.1	LX			15	KW	GCN 15889
140301A	1.416	0.95 ± 0.18	LX	C		31	Swift	GCN 15906
140304A	5.283	15.3 ± 1.1	LX	E		32	Fermi	GCN 15923
140311A	4.954	11.6 ± 1.5	LX			71.4	Swift	GCN 15962
140419A	3.956	185 ± 77	LX	C		80	KW	GCN 16134
140423A	3.26	65.3 ± 3.3	LX			95	Fermi	GCN 16152
140428A	4.7	1.88 ± 0.31				17.42	Swift	GCN 16186
140430A	1.6	1.54 ± 0.23				173.6	Swift	GCN 16200
140506A	0.889	7.75 ± 0.80	LX	E		64	Fermi	GCN 16220
140508A	1.027	23.24 ± 0.26	LX			44.3	Fermi	GCN 16224
140509A	2.4	3.77 ± 0.44	LX			23.2	Swift	GCN 16240
140512A	0.725	7.76 ± 0.18	LX			148	Fermi	GCN 16262
140515A	6.32	5.41 ± 0.55				23.4	Swift	GCN 16284
140518A	4.707	5.89 ± 0.59				60.5	Swift	GCN 16306
140614A	4.233	7.3 ± 2.1	LX			720	Swift	GCN 16402
140620A	2.04	6.28 ± 0.24	LX			46	Fermi	GCN 16426
140623A	1.92	7.69 ± 0.68				110	Fermi	GCN 16450
140629A	2.275	6.15 ± 0.90	LX			26	KW	GCN 16495
140703A	3.14	1.72 ± 0.09	LX			84	Fermi	GCN 16512
140801A	1.32	5.69 ± 0.05				7	Fermi	GCN 16658
140808A	3.29	11.93 ± 0.75				4.7	Fermi	GCN 16669
140907A	1.21	2.29 ± 0.08	LX			35	Fermi	GCN 16798
141026A	3.35	7.17 ± 0.90	LX			146	Swift	GCN 16960
141028A	2.33	68.9 ± 0.02				31.5	Fermi	GCN 16971
141109A	2.993	33.1 ± 6.9	LX			94	KW	GCN 17055
141121A	1.47	14.2 ± 1.1	LX		UL	1200	KW	GCN 17108
141220A	1.3195	2.44 ± 0.07				7.6	Fermi	GCN 17205
141221A	1.47	6.99 ± 1.98	LX	C		23.8	Fermi	GCN 17216
141225A	0.915	2.29 ± 0.11				56	Fermi	GCN 17241
150120B	3.5	7.37 ± 1.09	LX			24.3	Swift	GCN 17330
150206A	2.087	55.6 ± 20.1	LX			60	KW	GCN 17427
150301B	1.5169	2.87 ± 0.42	LX			13	Fermi	GCN 17525
150314A	1.758	95.2 ± 3.1	LX			10.7	Fermi	GCN 17579
150323A	0.593	1.30 ± 0.30				38	KW	GCN 17640
150403A	2.06	98.1 ± 6.3	LX			22.3	Fermi	GCN 17674
150413A	3.139	49.80 ± 7.01				263.6	KW+Swift	GCN 17731
150821A	0.755	14.7 ± 1.1	LX			103	Fermi	GCN 18190
150910A	1.359	21.6 ± 1.8	LX			112.2	Swift	GCN 18268
151021A	2.33	112.2 ± 35	LX			100	KW	GCN 18433
151027A	0.81	3.94 ± 1.33	LX	C		124	Fermi	GCN 18492
151027B	4.063	18.6 ± 3.7	LX			80	Swift	GCN 18514
151111A	3.5	3.43 ± 1.19	LX	E		40	Fermi	GCN 18582
151112A	4.1	12.1 ± 1.5	LX			19.32	Swift	GCN 18593
151215A	2.59	1.89 ± 0.43	LX			17.8	Swift	GCN 18699
160121A	1.96	2.54 ± 0.21	LX			12	Swift	GCN 18919

Table A3: continued.

GRB	z	$E_{\text{iso}}^{(a)}$	LX ^(b)	Early flare ^(c)	UL ^(d)	$T_{90}^{(e)}$	Instrument ^(f)	Reference ^(g)
160131A	0.972	58.7 ± 32.7	LX			200	KW	GCN 18974
160203A	3.52	12.0 ± 1.0	LX			20.2	Swift	GCN 18998
160227A	2.38	5.52 ± 2.38	LX			316.5	Swift	GCN 19106
160228A	1.64	15.98 ± 0.80				98.36	Swift	GCN 19113
160509A	1.17	84.5 ± 2.3	LX			371	Fermi	GCN 19411
160623A	0.367	22.4 ± 1.5	LX			38.9	KW	GCN 19554
160625B	1.406	419.0 ± 4.8	LX			460	Fermi	GCN 19587
160629A	3.332	48.8 ± 9.9				66.6	Fermi	GCN 19628
160804A	0.736	2.46 ± 0.51	LX			130	Fermi	GCN 19769
161014A	2.823	10.1 ± 1.7				37	Fermi	GCN 20051
161017A	2.013	7.56 ± 1.55	LX			32	Fermi	GCN 20068
161023A	2.708	73.9 ± 27.5	LX			50	KW	GCN 20111
161108A	1.159	1.66 ± 0.15	LX			105.1	Swift	GCN 20151
161117A	1.549	31.2 ± 5.5	LX			122	Fermi	GCN 20192
170113A	1.968	19.91	LX	C		49.2	Swift	GCN20452, GCN20458
170202A	3.645	17.0	LX			30.0	Swift	GCN20584, GCN20604
170214A	2.53	392 ± 3				122.9	Fermi	GCN20675, GCN20686
170405A	3.51	241 ± 52	LX	C		78.6	Swift	GCN20986, GCN20990
170519A	0.818		LX	C		216.4	Swift	GCN21112, GCN21119
170531B	2.366		LX	C		164.1	Swift	GCN21177, GCN21209
170604A	1.329	4.7 ± 0.5	LX	C		30	Swift	GCN21197, GCN21247
170607A	0.557	1.113	LX	C		29.9	Swift	GCN21218, GCN21240
170705A	2.01	14.95	LX	C		22.8	Swift	GCN21297, GCN21298
170903A	0.886		LX			25.6	Swift	GCN21799, GCN21812
171010A	0.3285	14.49	LX			107.3	Fermi	GCN22002, GCN22096
171222A	2.409	20.73	LX	C		80.4	Swift	GCN22272, GCN22277
180115A	2.487		LX			40.9	Swift	GCN22346, GCN22348
180205A	1.409		LX			15.4	Swift	GCN22384, GCN22386
180314A	1.445	6.58	LX			22.0	Swift	GCN22484, GCN22485
180325A	2.248	23.0	LX			10.0	Swift	GCN22535, GCN22555
180329B	1.998		LX	C		210.0	Swift	GCN22566, GCN22567
180404A	1.000		LX			35.2	Swift	GCN22591, GCN22599
180510B	1.305		LX			134.3	Swift	GCN22702, GCN22705
180620B	1.1175	16.3	LX	C		46.7	Swift	GCN22813, GCN22823
180624A	2.855		LX	C		486.4	Swift	GCN22845, GCN22848
180703A	0.6678	3.15				20.7	Fermi	GCN22889, GCN22896
180720B	0.654	68.2 ± 2.2	LX	C		48.9	Swift	GCN22981, GCN22996
180728A	0.117	3.15 ± 0.7	LX			6.4	Swift	GCN23055, GCN23067
180914B	1.096	360				280.0	AGILE	GCN23246, GCN23240
181010A	1.39		LX			9.7	Swift	GCN23315, GCN23320
181020A	2.938		LX	C		15.1	Swift	GCN23452, GCN23456
181110A	1.505	11.0	LX	C		140.0	Swift	GCN23421, GCN23424